INVESTIGATION OF NANOPARTICLE-PROTEIN INTERACTIONS WITH NOVEL METHODS

THÈSE N° 8534 (2018)

PRÉSENTÉE LE 27 MARS 2018

À LA FACULTÉ DES SCIENCES ET TECHNIQUES DE L'INGÉNIEUR

LABORATOIRE DES NANOMATÉNAUX SUPRAMOLÉCULAIRES ET INTERFACES - CHAIRE CONSTELLIUM

PROGRAMME DOCTORAL EN SCIENCE ET GÉNIE DES MATÉRIAUX

ÉCOLE POLYTECHNIQUE FÉDÉRALE DE LAUSANNE

POUR L'OBTENTION DU GRADE DE DOCTEUR ÈS SCIENCES

PAR

Ahmet BEKDEMIR

acceptée sur proposition du jury:

Prof. P. Muralt, président du jury
Prof. F. Stellacci, directeur de thèse
Prof. K. Dawson, rapporteur
Prof. H. Cölfen, rapporteur
Prof. R. Riek, rapporteur

ÉCOLE POLYTECHNIQUE
FÉDÉRALE DE LAUSANNE

Suisse
2018

Gözleri aşkla gülen biricik sevdiğim Elif'ime…

ACKNOWLEDGMENTS

My journey throughout this 4.5 years has finally come to an end. During these years, I got to meet a lot of people who touched my life one way or another. I probably cannot count the names of all of you here but I would like you to know that it was a pleasure to meet and talk to you.

First of all, I have always been grateful to my supervisor, Francesco, for accepting me to his group and giving me a chance to find my way in science. I appreciated all of our discussions. Thank you also for supporting me to pursue next steps in my career and all your valuable advices.

Aside from this, first, I would like to thank my parents for supporting me not only during these PhD years but also throughout my entire career. On top of having trusted me on every choice I made in my life, you have become true guardian angels for me. I also thank my sister for being just who she is. You have always been kind and encouraging to me. I honestly do not want to know how my life would be if you were not around me. Thank you Meltem'im.

I would like to express my gratitude to all of my colleagues in SUNMIL for all of the fruitful discussions and feedbacks not only scientifically but also non-scientifically. I learned a lot from you. In particular, I enjoyed all politics, history and science discussions with my office mate, Paulo. Also, I thank Matej, Özgün, Pelin, Nikos, Sergio, Ula, Maria, Anna, Marie, Rosie, Simone and Evi for nice coffee breaks. They were really valuable times for me.

ABSTRACT

Advancements in novel nanomaterials present promising avenue for therapeutics and diagnosis in nanomedicine. Importantly, in these applications, nanoparticles (NPs) are almost instantly coated with a complex layer of proteins in biological environment, termed as 'protein corona'. Understanding the interactions between the proteins and NPs has therefore been one of the key challenges in nanomedicine. The techniques established particularly for thermodynamic investigation of protein-NP interactions, however, suffer from spurious signals produced by aggregates in solution or require additional fluorescent labelling either of NPs or the proteins. In addition, there is a lack of careful systematic studies of the relationship between binding mechanism and the NP parameters such as size, surface chemistry and hydrophobicity.

Presented within this thesis, a novel centrifugation-based methodology to investigate thermodynamic interaction parameters of NPs with proteins utilizing their hydrodynamic properties. With this technique, it is possible to monitor anisotropic shape evolution of NP-protein complex during the course of protein titration, especially for very small NPs. By exploiting Heteronuclear Single Quantum Coherence NMR spectroscopy, protein binding sites to NPs were carefully investigated with the help of diminishing cross peak signals of amino acids in the model protein, ubiquitin. Having developed high quality, monodisperse NPs with varying characteristics of size, hydrophobicity and surface chemistry, a systematic comparison study was carried out on the effects of such parameters on protein binding. The lack of correlation between the thermodynamic data and the mechanism of protein-NP interactions highlighted the importance of using multiple

methods to fully describe these interactions. Finally, sub-10 nm gold NPs coated with amphiphilic ligand shell were proposed as efficient cargo delivery platforms for hydrophobic drug molecules with remarkable colloidal stability. The potential of these platforms was further corroborated *in vitro* and *in vivo* with a variety of therapeutics.

Overall, we believe the characterization techniques presented herein elucidate crucial aspects of NP-protein interactions and their relationship to structural parameters of the NPs. The implications of this work are anticipated to pave the way for better design of nanomedicine tools.

RÉSUMÉ

Les progrès réalisés dans le domaine des nanomatériaux novateurs constituent une approche prometteuse pour les thérapies et les diagnostiques de la nanomédecine. En particulier dans ces applications, les nanoparticules (NPs) en environnement biologique sont presque instantanément recouvertes d'une couche complexe de protéines, appelé « couronne protéique ». Comprendre les interactions entre les protéines et les NPs a donc été l'un des principaux défis de la nanomédecine. Cependant, les techniques établies spécifiquement pour l'étude thermodynamique des interactions NP-protéine souffrent de signaux parasites produits par des agrégats en solution ou nécessitent un marquage fluorescent supplémentaire des NPs soit des protéines. En outre, il y a un manque d'études systématiques minutieuses de la relation entre le mécanisme de liaison et les paramètres des NPs tels que la taille, la chimie de surface et l'hydrophobicité.

Dans le cadre de cette thèse, une nouvelle méthodologie basée sur la centrifugation est présentée pour étudier les paramètres d'interaction thermodynamique des NPs avec des protéines en utilisant leurs propriétés hydrodynamiques. Avec cette technique, il est possible de suivre l'évolution de la forme anisotrope du complexe NP-protéine au cours du titrage des protéines, en particulier pour les très petites NPs. En exploitant la spectroscopie de RMN à Cohérence Quantique Hétéronucléaire Unique, les sites de liaison des protéines aux NPs ont été soigneusement étudiés à l'aide de la diminution des signaux de crête croisés des acides aminés dans la protéine modèle, l'ubiquitine. Ayant développé des NPs monodispersées de haute qualité avec des caractéristiques variables de taille, d'hydrophobicité et de chimie de surface, une étude de comparaison systématique a été réalisée sur les effets de tels

paramètres sur la liaison aux protéines. Le manque de corrélation entre les données thermodynamiques et le mécanisme des interactions NP-protéine a mis en évidence l'importance d'utiliser plusieurs méthodes pour décrire complètement ces interactions. Finalement, des NPs d'or de moins de 10 nm revêtus d'une enveloppe de ligands amphiphiles ont été proposés comme plates-formes efficaces de livraison pour des molécules de médicaments hydrophobes, avec une stabilité colloïdale remarquable. Le potentiel de ces plateformes a été corroboré *in vitro* et *in vivo* avec une variété de produits thérapeutiques.

Dans l'ensemble, nous croyons que les techniques de caractérisation présentées ici éclaircissent les aspects cruciaux des interactions NP-protéine et leur relation avec les paramètres structuraux des NPs. Les implications de ce travail devraient ouvrir la voie à une meilleure conception des outils de la nanomédecine.

Mots-clés : nanomédecine, couronne protéique, interactions nanoparticule-protéine, délivrance de médicaments, ligands mixtes, nanoparticules d'or amphiphiles

List of Abbreviations

2D	two-dimensional
3D	three-dimensional
allMUS	homoligand MUS coated gold nanoparticles
AUC	analytical ultracentrifugation
AuNPs	gold nanoparticles
BSA	bovine serum albumin
Cryo-EM	cryogenic electron microscopy
CyC	cytochrome C
DGU	density gradient ultracentrifugation
DMSO	dimethylsulfoxide
HSA	human serum albumin
HSQC	Heteronuclear Single Quantum Coherence Spectroscopy
MD	molecular dynamics
MUA	11-mercaptoundecanoic acid
MUS	11-mercaptoundecane sulfonate, sodium salt
MUSOT	mixed-ligand MUS:OT coated gold nanoparticles
NMR	nuclear magnetic resonance
NP	nanoparticles
NR	nanorod
OT	1-octanethiol
PC	protein corona
PCA	principal component analysis
QCM	quartz crystal microbalance
R848	resiquimod

SE   sedimentation equilibrium

SPR   surface plasmon resonance

SV   sedimentation velocity

TGA   thermogravimetric analysis

<p style="text-align: center;">Table of Contents</p>

CHAPTER 1

1. NANOMEDICINE: A BRIEF INTRODUCTION

Designing efficient nanomaterials for medicinal applications has been a long-standing, promising endeavor that founded the basis of a scientific discipline termed as nanomedicine. In the beginning of this chapter, some of the promising approaches are outlined in order to give the reader a glimpse of the meaning of nanomedicine. Aiming to prepare the reader for detailed discussions of experimental results in the subsequent chapters, more detailed description of nanoparticle types and their physicochemical properties that influence their performance in such applications will be provided.

1.1. Nanomedicine: is it worth to sweat for?

Nanomedicine is a multidisciplinary research area that aims to utilize the tool-box of nanotechnology, biology and chemistry to remedy both long-standing and recently emerged diseases. Over the past two decades, the advancements in molecular biology, (supramolecular) chemistry and engineering enabled nanotechnology to advance in early detection and treatment of diseases at cellular and molecular level. To fulfill such promises, the foundation of any research in nanomedicine ought to be established on at least three crucial pillars: (i) a thorough knowledge of biology and pathophysiology of diseases in order to create efficient diagnosis and therapeutics, (ii) powerful methodologies to produce nanoscale matter and detailed
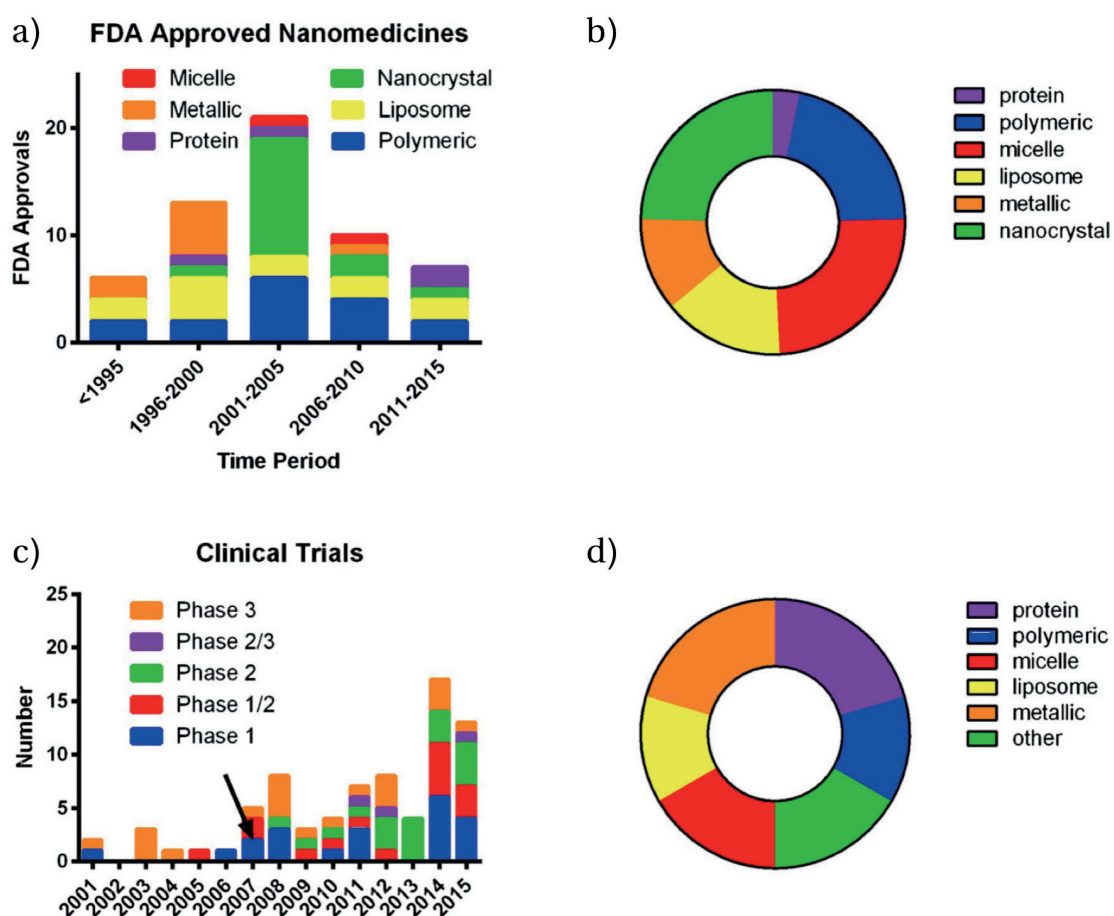
Figure 1.1: Clinical trials trends in nanomedicine development through years. a) FDA approved nanomedicines categorized by the material divided each 5-year span; b) overall FDA approval categorized by the material; c) clinical trials information obtained from clinicaltrials.gov between 2001-2015, arrow indicates the start date of US law (FDAAA 801) which requires reporting to the database; d) nanomedicines under clinical trials categorized by material. Adapted from reference [1] with the permission of Springer Nature.

characterization of their physicochemical properties and (iii) advanced chemistry tool-box to stabilize nanomaterials for biocompatibility and to functionalize them for efficient targeting of therapeutics.

The pioneering work in nanomedicine undertook a mission to improve disease therapy with unprecedented precision and efficiency, hence, plethora of work was put in to develop novel NP formulations. Only recently, however, the exponential growth on the number of clinical trials was reported [2]. In 1990s, the majority of clinical trials of nanomedicines was composed of liposomal and polymeric NPs whereas starting from 2000s, micellar, metallic, protein-based particles as well as nanocrystals have been more favorable (Figure 1.1). Particularly metallic NPs that have efficient optoelectronic properties were studied and many trials are pending in this topic. For example, various types of iron oxide NPs have undergone clinical trials [1]. Apart from being efficient contrast agents which is advantageous for imaging purposes, iron oxide NPs were shown to be effective in iron replacement therapy (Venofer®, Ferrlecit®, Dexferrum® and Feraheme®) as well as a tumor therapy with hyperthermia (Nanotherm™) [1,3]. Gold has been another highly studied core metal in NPs due to its unique combination of optical and thermal properties as well as their ease of synthesis and functionalization. The clinical trials, however, approach gold-based nanomedicines with extreme caution, particularly when they are not well coated with 'antifouling' materials such as PEG or silica [4,5]. Rare examples include Naomi Halas' gold-silica nanoshells that were recently approved by FDA under the production of Nanospectra Biosciences. These nanoshells were designed to generate heat upon irradiation with near IR laser and cause the burst of the surrounding cancer cells [6]. In many other approaches, however, gold NPs were used as templates to develop novel designs and then transfer the technology to more bio-friendly

platforms. For instance, Chad Mirkin demonstrated that nucleic acid coated gold NPs were able to enter cells by initiating particular pathways, proposing potentially efficient drug delivery systems [7]. Developed with a similar approach, spherical nucleic acid NPs were recently approved by FDA as an early-stage clinical trial drug for therapy of glioblastoma multiforme [8]. Many other gold-based novel NPs are still in development phase with highly encouraging medicinal properties [9].

In spite of encouraging number of trials, nanomedicine is still thought to be far from what it has originally promised [10]. As per the completion of these promises, increasing number of *in vivo* studies and clinical trials is nowadays postulated as the 'next wave' for the nanomedicine platforms [11]. In order to establish such goals, however, it is crucial not to divert our attention from developing novel nanomaterials and discovering more efficient approaches to be successful in clinical nanomedicine. Overall, it is definitely worth to pursue this endeavor as long as there is a close collaboration of clinical studies with innovation of novel nanomaterials with unique properties. To this end, various nanoparticle types and their physicochemical properties pertaining to medicinal applications will be discussed in the subsequent sections.

1.2. Nanoparticles in Disease Therapy

Smart delivery of drug molecules and genetic materials into cells have been a center of interest in medicine in order to increase the efficiency of therapy while avoiding side-effects. The ability to tune NPs' size and surface chemistry opens up multiple avenues for developing NPs based drug delivery platforms. The potential advantages of employing NPs in therapeutics as delivery agents can be listed as follows:

4

- Due to small size, drug molecules are undergoing fast renal clearance, hence decreasing the effective concentration. Drug loaded NPs can avoid renal clearance and increase the half-life of the drug circulating in the blood.

- Drug – NP conjugates can be dissociated only at the target tissue/cellular environment. The necessary initial dose of drug can be decreased which alleviates side-effects and high cost problems.

- Some hydrophobic drugs are injected with toxic solvents and present precipitation problem. Also, body's immunogenic response to drug molecules can be avoided by 'hiding' the drug within NPs from the macrophages.

- Active form of drugs can be directly used to load to NPs unlike pro-drug molecules that need to undergo chemical transformation on site in order to become pharmaceutically active.

- Drug molecules in NP carriers can be activated only at disease site when designed with stimuli responsive processes.

Cargo molecules can be loaded in NPs carriers in number of ways either by covalent attachment or weak forces such as electrostatic or hydrophobic interactions. Chemical conjugation of drug molecules entails additional chemistry both on NPs and drug molecules. Also, the conjugation should be specifically cleaved at the target site to release the drug molecules. These extra steps require fine-tuned orthogonal bioconjugation methodologies on NP–drug systems. On the other hand, encapsulation of drugs in NPs through non-covalent interaction or simply by physical entrapment do not modify drug molecules and therefore retain their active form. However, in this case, drug molecules' premature release should also be controlled with additional factors either by chemical modification on NPs or

dissociating NPs completely at the target site upon change in the environment such as pH or concentration of mildly reducing amino acids.

1.2.1. Organic Nanoparticles for Drug Delivery

In aqueous environments, amphiphilic lipid molecules are typically self-assembled in certain concentration rendering spherical NPs such as liposomes or micelles, inside of which are completely hydrophobic. During the formation of self-assembly, if hydrophobic drug molecules are introduced in solution, they thermodynamically avoid unfavorable interactions with water molecules and prefer to reside inside of the NPs. Using liposomes or micelles are therefore an easy and efficient way of solubilizing drug molecules by encapsulation. In fact, a chemotherapeutic drug, doxorubicin loaded liposomes (Doxil®) were presented as the first FDA-approved nano-drug that showed enhanced *in vivo* stability and half-life compared to doxorubicin alone [12]. Targeting in these systems could also be conferred by incorporating specific ligand molecules to receptors on the cell membrane [13]. Drug release could be achieved by the decomposition of NPs upon an encounter with the structurally commensurate cell membrane {Wang:2016hm}. This mechanism, however, also brings upon a limitation for such NP carrier system because of the possibility of non-specific or early release. More stability is obtained with additional stabilizers and surfactants which form the basis of generic solid lipid NPs [14]. Although these NPs have shown better stability, they were captured primarily by reticuloendothelial system (RES) because of their hydrophobic core which limits the potency of these systems [15].

Degradable or non-degradable polymers were suggested as more robust organic NPs for drug delivery. Most common degradable polymeric NPs are made of PEG, poly(vinylpirrolidone) and poly (N-isopropylacrylamide) [16]. Precipitation of linear polymers into colloidal NP form enables to encapsulate drug molecules as well as large genetic materials and proteins. Different pH at the target site changes their solubility and structural deformation upon regained solubility results in releasing the cargo [17]. Such mechanism can generally be conferred on polymers with additional chemical conjugation of pH responsive functional groups to polymer backbone which may complicate the synthesis. On the other hand, using biodegradable polymers such as poly(lactic-glycolic acid), poly(methyl methacrylate) and poly(L-glutamic acid) allow metabolic hydrolysis in biological systems without additional modification [18]. These polymers can also provide slow release of drug molecules which is generally beneficial in pharmacokinetics. Carbon based NPs such as fullerenes and carbon nanotubes (CNTs) were another choice of study on drug delivery because of their efficient drug loading capacity [19]. Their transport across cells are similar to liposomes because of their hydrophobic nature which allows membrane penetration without causing disruption. However, these carriers have been reportedly apoptotic, increasing the mitochondrial production of reactive oxygen species in cells [20].

1.2.2. Inorganic Nanoparticles for Drug Delivery

Inorganic NPs are extensively utilized in nanotherapeutics because of their ease of preparation and functionalization. For instance, silica NPs are one of the most commonly used inorganic NPs with stimuli responsive drug release mechanisms [21-23]. Drugs are loaded either into channels of mesoporous silica structure or simply
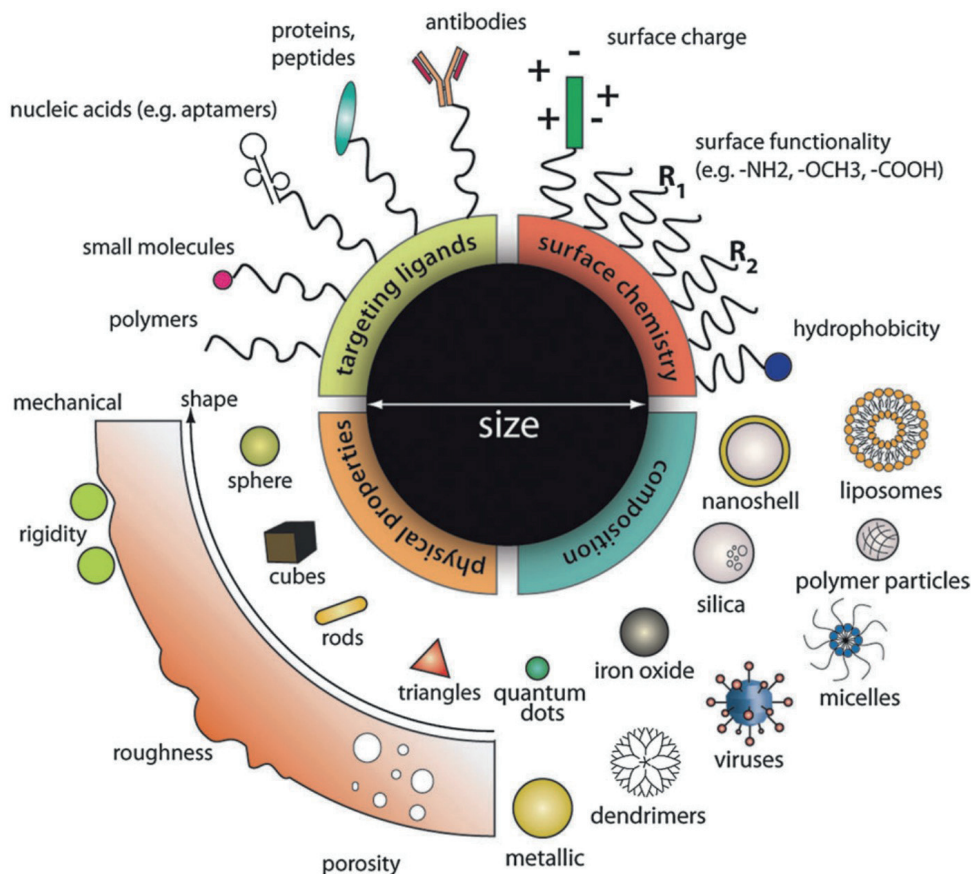
Figure 1.2: Summary of physicochemical properties of nanoparticles that influence medicinal applications. The vastness of these properties allows researchers to fine tune nanoparticles for specific purposes. Adapted from reference [24], permission from the Royal Society of Chemistry.

inside the core-shell silica NPs. The collaborative work of Frasier Stoddart and Jeffery Zink pioneered on mesoporous silica NPs that use molecular switches as gating devices for cargo loading and release as delivery vehicles [25]. Multiple biological stimuli such as a pH change or enzymatic cleavage were utilized as inputs for these

systems [25,26]. Although as elegant design as they seem to have, there is still work to be done to simplify the chemistry for the practical purposes in clinical applications.

Metal NPs such as gold, titanium, silver, copper and iron constitute another subclass of inorganic NPs that are studied to be used for drug delivery applications [27]. Among these, gold NPs are one of the most studied NPs due to their facile synthesis and functionalization as well as the absence of apparent cytotoxicity. Densely packed ligand shell on the surface of gold NPs can be easily functionalized with various therapeutics and cleaved with easy chemistry (e.g. by oxidation of thiol). Anisotropic gold NPs such as nanorods and nanostars are able to create hyperthermia effect owing to their electron dense tips which also contribute to killing tumor cells and are used in therapeutics [28]. However, there is a concern about long term accumulation health effects because gold is not biodegradable. Apart from being inherently antibacterial, silver NPs were also developed as potential drug delivery agents.

Although historically reported as toxic, the surface modifications of silver NPs were recently revisited with improved stability in biological environment, rendering them safe at moderate doses [29]. Additional optical properties such as superior light absorption also contributed the use of silver NPs for multipurpose therapeutic delivery platforms.

1.3. Physicochemical Properties of NPs that Influence Medicinal Applications

Physicochemical properties of NPs may have dramatic influence on their medicinal use (Figure 1.2.). Parameters such as size, shape and surface ligands of NPs can affect the outcome for cytotoxicity, colloidal stability in biological environment, cellular

transport mechanism and targeting efficiency. Among them, the following sections focus particularly on size, shape, ligand chemistry and charge of NPs.

1.3.1. Size and Shape

In cancer therapy, one of the most immediate outcome of size parameter in NPs is the passive accumulation to the tumor tissue due to enhanced permeation and retention (EPR) effect [24]. When coupled with poor lymphatic drainage, abnormally fast-growing tumor cells result in leaky vasculature which leads to transport of smaller than 100 nm NPs into tumor tissue. The circulation time in blood and cellular transport mechanism are also size dependent properties [30]. For example, 500 nm NPs enter cells *via* caveolae-mediated internalization, while smaller NPs are internalized by phagocytosis or clathrin-mediated endocytosis [31]. Penetration of NPs into cellular nucleus was also shown to be size selective, with 50 nm gold NPs cannot pass through while smaller gold NPs were shown to be inside nucleus [32]. The size of NPs can also result in accumulation in different organs and affect the overall biodistribution. Recent studies showed that liver is the most affected organ when size of NPs is varied. ^{198}Au-radio-labelled negatively charged NPs were shown to accumulate primarily in liver with 50% for 1.4 nm and 99% for 200 nm [33]. At cellular level, it has been showed that cytotoxicity is greatly affected by size of NPs [34]. The smaller NPs has a higher tendency to aggregate and interact with biological components thereby increasing the toxicity. However, this statement should be taken with a grain of salt, as size is not the only parameter that determines the colloidal stability of NPs. Covering small NPs with highly charged surface ligands can easily outperform bigger NPs with uncharged ligands in solubility in aqueous media.

As far as the shape is concerned, NPs' geometry may influence the hydrodynamic behavior in blood, having an indirect effect on biodistribution and cellular uptake. Mechanistically speaking, prior to the cellular internalization, transport of NPs in blood is dictated by their margination (i.e. radial drift) towards the blood vessel walls. The degree of margination influences NPs' interaction with tumor vascular bed to have subsequent interactions. Margination is usually not attained due to convective transport of NPs in tumor tissue. Oblate-shaped NPs show more efficient tumbling and rotation than spherical NPs and therefore have increased lateral drift which favors the margination [35,36]. That is, anisotropic NPs can have increased probability of interacting with the tumor vasculature than their spherical counterparts [37]. Also, phagocytotic uptake by macrophages is less efficient for oblate shape NPs, and therefore these NPs can stay circulating in blood without being cleared by RES. In this context, 100 nm-long nanochains with aspect ratio of 4 was accumulated in liver significantly less than 100 nm nanosphere of the same material [38,39]. Besides macrophages, NPs shape governs the endocytotic uptake mechanism by cancer cells. Rod-like NPs showed the highest uptake in HeLa cells followed by spheres, cylinders and cubes [40]. Also, compared to spherical NPs, oblong shaped NPs exhibited higher avidity to receptor surface rendering them better cargo carriers with higher targeting ability [41].

1.3.2. Ligand Type and Surface Charge

NPs' surface is highly critical as it constitutes one of the primary features that directly encounter the environment. The degree of colloidal stability as well as interaction with other biomolecules intra- and extra-cellularly depends largely on what NPs' surface is comprised of. For example, PEG coating to NPs has shown to confer

biocompatibility and reduce macrophage uptake to increase circulation time in blood. In addition, NPs' surface could be enriched with peptide-based targeting molecules to increase the specificity of cargo delivery. For example, TAT peptides, neurotensin-targeting peptides, transferrin have been incorporated to NPs for delivery to brain [42]. Arginine functionalized NPs have shown to promote cellular uptake without increasing cytotoxicity whereas incorporation of histidine residues stimulates proton sponge effect to increase the cargo release in cytoplasm. In order to increase the targeting efficiency, various NPs such as liposomes, polymeric NPs and inorganic NPs were coated with monoclonal antibodies for specific attachment to tumor antigens. Although, antibody – NP conjugates have shown to be highly efficient systems in targeting *in vitro*, their high cost and low stability limits their applications *in vivo*. Also, the potential immunogenicity and retention in RES suggests more detailed design of such systems is necessary.

Designing synthetic ligands on NPs surface for distinct cell membrane interaction is also possible. Our group, for instance, discovered that sulfonate coated negatively charged sub-10 nm gold NPs can diffuse through cell membrane without endocytotic pathway only if the ligand layer consists of a mixture of hydrophilic – hydrophobic ligands [43-45]. The ability to immerse into the membrane is attributed to amphiphilic lipid-like structure of ligand monolayer of NPs that can match with a cell membrane and the interaction becomes favorable. Detailed physicochemical and computational studies revealed such behavior is also strictly size dependent [46,47]. Another interesting example is recently emerged spherical nucleic acid NPs developed by Mirkin's group. Oligonucleotides arrange themselves to selectively bind to class A scavenger receptors on cell membrane which facilitates rapid internalization through lipid-raft dependent caveolae-mediated pathway [48,49].

The tendency of NPs to interact with the environment is highly dependent on their surface charge. In solution, the surface charge density of NPs or their electric potential is an indirect way of measuring their colloidal stability. Although higher density of charges on the surface of NPs may increase the colloidal stability due to repulsive forces in biological environment, this may result in their increased attachment to various biomolecules as they are heterogeneous in surface charge and can initiate attractive electrostatic forces. Positively charged NPs were reported to have higher uptake than negative or neutral NPs. However, they do have favorable toxicity because of depolarization of the membrane potential in a dose dependent manner, eventually resulting in membrane disruption [7]. On the other hand, negatively charged NPs can promote anticoagulant activity and stimulate cytokine release [33]. In some cases, their cytotoxicity is based on initiation of apoptosis in phagocytic cells. Recent reports on gold NPs that are covered with zwitterionic ligands were shown to be resistant to attach biomolecules and have increased half-life in blood circulation compared to positively and negatively charged gold NPs [50]. Similar low attachment behavior was observed for zwitterionic iron oxide NPs in terms of decreased cellular internalization *in vitro* which demonstrates the minimal effect of core material for the occurrences of such properties [51].

1.4. Conclusion

In summary, nanotechnology provides numbers of different ways to improve medicinal imaging, diagnostics and therapy. Various types of materials in nano form can be employed to create contrast to visualize, transport therapeutics cargo protecting from early release *en route*, and release/activate drugs selectively at the disease site. Modifications of structural parameters of NPs such as size, shape, ligand

type and surface charge were found to be extremely crucial and beneficial to confer these superior properties in nanomedicine.

2. INTRODUCTION TO PROTEIN CORONA

Nanomedicine, as discussed in the previous chapter, promises to increase efficiency of imaging and therapeutic approaches by exquisite properties of nanoparticles. Advanced chemical and biological tools are employed to create better nanoparticle systems that can address inadequate efficiency of drugs and substantial side-effects in clinical medicine. When nanoparticles are introduced into blood, most often they encounter with biomolecules which form nanoparticle-protein complexes; termed protein corona. Protein corona might jeopardize or at least alter the properties of nanoparticles originally designed. Therefore, there has been huge interest in understanding the phenomenon in more detail to achieve better nanomedicine systems. This chapter gives an introduction on how protein corona affects NPs' behavior *in vitro* and *in vivo*. Later, the summary of methodologies reported in literature for characterization of NP – protein interactions are given in larger detail.

2.1. Ramifications of Protein Corona *In Vitro* and *In Vivo*

The term protein corona/biomolecular corona (PC) reflects the complex self-assembly of NPs and biomolecules that forms upon administration of NPs to blood. For the last decade, the effect of corona on NPs' blood circulation and cellular internalization was demonstrated to be significant (Figure 2.1). In some instances, a crucial portion of corona includes opsonins that facilitate the uptake by RES while decreasing the circulation span in body. The opsonin proteins create molecular
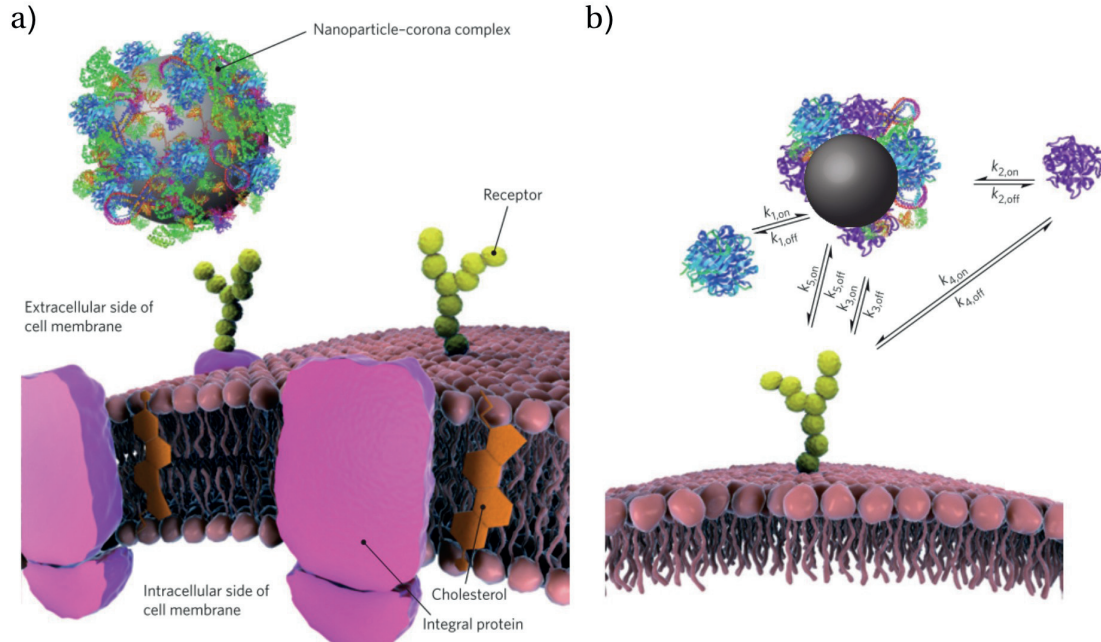
Figure 2.1: Protein corona, or in broader term biomolecular corona, affects targeting applications of nanoparticles. For example, a) cell membrane receptor binding can be hindered with the presence of corona around nanoparticles; b) in fact, the complex interactions between proteins and nanoparticles as well as between nanoparticles and cell membrane receptors define the final attachment. Adapted from reference [52], permission from the Nature Publishing Group.

signature on NPs that is recognized by immune cells and therefore hinder the outreach of NPs to disease site. For example, antibody functionalized NPs have been shown to target efficiently in serum free *in vitro* studies, whereas *in vivo* targeting was diminished quite dramatically. Mahmoudi *et al.* demonstrated that such disparity in fact occurs due to covering of NPs with serum proteins which limit the accessibility of the targeting moieties *in vivo* [53,54]. Up to 99% targeting efficiency loss was

observed when a silicon substrate is used to simulate cell membrane targeting by using cycloalkyne click chemistry [55]. Warren Chen and coworkers evidenced a premature release of cargo molecules from polymeric micelles because protein corona conferred instability to micelles before reaching the cells [56,57]. They later showed $\alpha-$ and $\beta-$ globulins were mainly responsible for the quick release of Förster resonance energy transfer (FRET) molecules from polymeric micelles [58]. Nonetheless, the presence of a PC is not always associated with hindrance of targeting, but occasionally also results in selective uptake by specific cell types. Recent results on hyaluronic acid-based nanocapsules point to enhanced targeting specificity to CD44+ because the presence of PC hampers the binding of nanocapsules to CD44- cells more than CD44+ cells [59].

Other applications of nanoparticles in medicine have exploited PC formation to overcome any issues pertaining to nanomaterial toxicity. For example, physical damage to lipid membranes triggered by graphene oxide nanosheets during cellular uptake can be mitigated by pre-coating the particles with proteins prior to administration [60]. Apart from PC's direct implications on nanotherapeutics or nanotoxicology, the identity of proteins localized in the PC can carry rich information related to the microenvironment surrounding NPs. For example, protein profiles of various types and sizes of NPs gathered from proteomic studies indicate enrichment of certain complement proteins (C1q and C3) in the fluid lining the respiratory tract after incubating with a simulant lung lining fluid [61]. Another study concluded that post-translational modifications of proteins can impact NP – cell interactions based on the comparative cell binding experiments with NPs coated with glycosylated PC vs. deglycosylated PC [62].

2.2. Physicochemical Properties of Nanoparticles that Affect Protein Corona

The majority of studies concentrated on the surface charge of the NPs as it is one of the most apparent characteristics of NPs. Neutral NPs have shown to have distinctively less protein adsorption than charged NPs, indicating a strong correlation between the surface charge and PC [63]. In parallel, as the surface charge density increased for polymeric NPs, increased amount of plasma protein adsorption was observed without the change in the composition [64]. Distinct proteins, on the other hand, may have different preferences on NPs charges. For instance, albumin with isoelectric point (pI) less than 5.5 predominantly binds to positively charged PS NPs whereas negatively charged PS NPs carry IgG (isoelectric point is higher than 5.5) to a higher extent [65]. Recently, Moyano et. al. carried out a comprehensive protein adsorption study with gold NPs coated with zwitterionic ligands and demonstrated their resistance to PC formation[66]. Targeting efficiency of zwitterionic ligand coated NPs were not diminished when in contact with serum rendering them highly versatile NP system with 'stealth' properties [67].

Surface chemistry of NPs also affects PC composition [68]. For example, dextran coated porous Si NPs exhibited lesser degree of opsonization which directly affects macrophage uptake and characterized by decreased percentage of immune proteins in corona composition [69,70]. Hydrophobic NPs are more susceptible for protein adsorption due to higher propensity of stabilizing their energetically active hydrophobic surface in aqueous environment [71]. NIPAM based polymeric NPs were shown to have dramatically enriched PC compared to their copolymer counterparts with 15% hydrophobicity induced with BAM polymer [72]. As far as size of NPs concerned, studies have shown that while larger NPs cause change in the
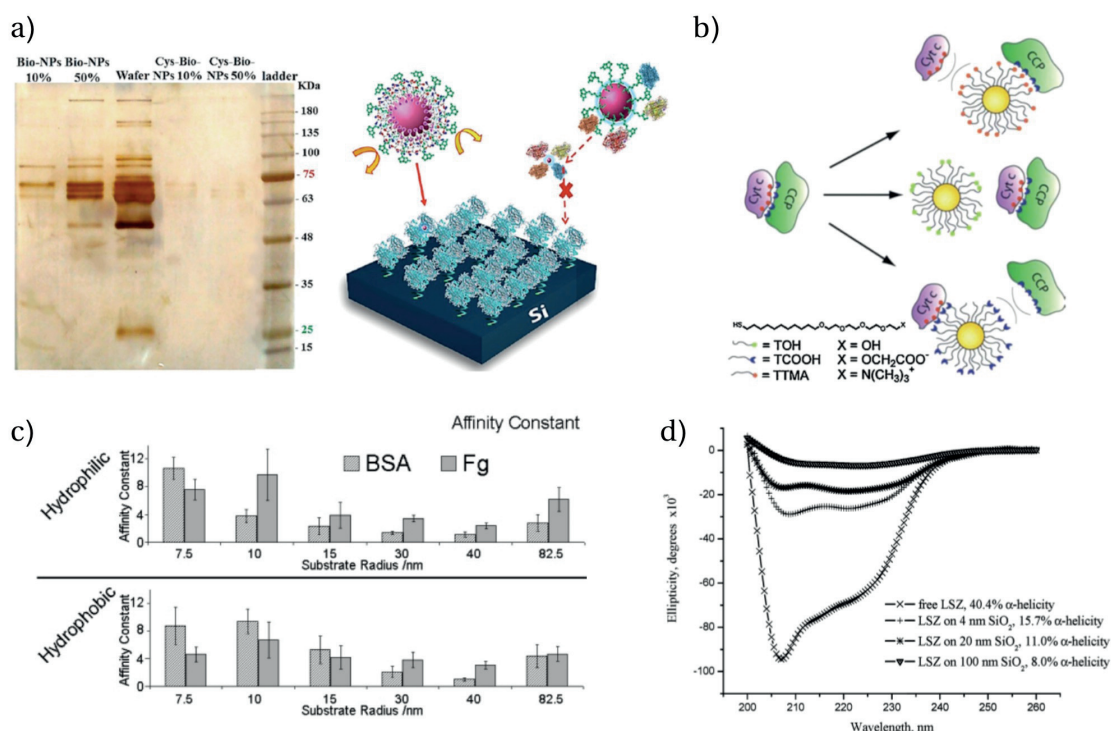
Figure 2.2: Various nanoparticle parameters were investigated in terms of protein adhesion. For example, a) ligand charge, zwitterionic cysteine functionalized NPs escaped from being coated with proteins and thus attached to the targeted surface more efficiently, ref. [73] with the permission of The American Chemical Society; b) depending on the surface charge of nanoparticles, different proteins can be attracted which can influence the protein function as well, ref. [74] with the permission of The Royal Society of Chemistry; c) hydrophobicity of nanoparticles may govern the binding affinities of certain proteins in corona, ref. [75,76] and d) certain nanoparticle size can alter protein conformation after attachment. For instance, lysozyme undergone deformation with increasing size of silica nanoparticles between 4nm, 20nm and 100 nm, ref. [75,76] with the permission from the American Chemical Society.

protein conformation due to highly energetic surfaces; this was not observed in smaller NPs possibly due to lack of large enough surface area for a protein to re-adapt

their conformation [75,76]. Additionally, a comparative study between hydrophobic and hydrophilic Si NPs against BSA and fibrinogen binding revealed the structural changes occurred in case of hydrophobic NPs [77].

2.3. Characterization Methods for Protein Corona

The characterization of protein corona can be divided into various sub-categories according to the answers they provide such as protein conformation, kinetics, protein affinity, stoichiometry and corona composition (Table 2.1).

2.3.1. Protein Conformation

Conformational change of protein upon adsorption to NP surface have been investigated with multiple spectroscopic methods among which circular dichroism (CD) has been arguably the most common. The response to polarized light is distinctively separate for α-helices and β-sheets in a protein with a relative population that can be calculated from the intensity of absorption of light. Upon contact with the NPs, any change in the secondary structure is reflected into the circular dichroism absorption spectrum as a variation in the relative ratio of alpha helices and beta sheets because any denaturing of protein should remove ordered structures of amino acid backbones [76,78]. Although easy operation and wide range of use, method requires large amount of proteins and the presence of NPs sometimes dramatically decrease the signal-to-noise ratio particularly at far UV-region [79]. Fourier-transform infrared and Raman spectroscopy are highly sensitive methods that can detect the structural changes in more detail. Vibrational energies of amino acids alter with conformational change in the protein due to differing electronic

environment. This in turn affect the energy absorbed by that particular mode, characterized by the peak corresponds to amide vibrational modes (1700 – 1600 cm^{-1})[80]. Nuclear magnetic resonance (NMR) spectroscopy has been another powerful characterization method particularly for small and medium size biomolecules. Protein characterization with both solid-state and liquid-state NMR spectroscopy provides highly detailed information on the protein structure as well as the protein-NP binding event at molecular level detail. However, sophisticated data analysis as well as the necessity of high sample concentration restricted the wide use of this method [81].

2.3.2. Protein Corona Evolution and Total Protein Concentration

Protein binding on NPs' surface effectively monitored in the change of hydrodynamic properties as more bound protein molecules simply increase the hydrodynamic diameter of NPs. This increase could be captured for example with dynamic light scattering (DLS). In fact, several studies utilized DLS to demonstrate the extent of corona formation as a function of diameter [82,83]. As long as monodisperse NPs are used and the size of NPs are distinctively different than most of the proteins in solution, DLS can provide corona evolution information. Although easy operation is the biggest advantage of DLS, the method is highly susceptible to overestimating larger sized contaminations and aggregations because light scattering intensity is dependent on the sixth power of radius. Recently, differential centrifugal sedimentation (DCS) has been applied to protein – NP interaction analysis based on size and density differentiation of NPs after protein coverage. This allows separation of pristine NPs and free proteins from NP- protein complexes and thus overcomes drawbacks of DLS based methods. Dawson *et. al.* has utilized this method extensively

Table 2.1: Summary of techniques available to investigate different aspects of protein corona.

NP - Protein Parameter	Techniques
Structure/Thickness	Dynamic Light Scattering (DLS)
	Differential Centrifugal Sedimentation (DCS)
	Transmission Electron Microscopy (TEM)
Protein Quantification	Bichinchoninic acid (BCA) assay
	Bradford assay
	Thermogravimetric analysis (TGA)
Binding Affinity and Stoichiometry	Fluorescence quenching titration
	Fluorescence Correlation Spectroscopy (FCS)
	Size Exclusion Chromatography (SEC)
	Isothermal Titration Calorimetry (ITC)
	Surface Plasmon Resonance (SPR)
	Quartz Crystal Microbalance (QCM)
Protein Conformation	Circular Dichroism (CD)
	Fourier-Transform Infrared (FTIR) Spectroscopy
	Raman Spectroscopy
	Nuclear Magnetic Resonance (NMR)
Protein Corona Composition	Sodium Dodecyl Sulfate - Polyacrylamide Gel Electrophoresis (SDS-PAGE)
	Mass Spectrometry (MS)

in their studies to semi-quantitatively show the degree of corona formation for various NPs [84,85].

In addition, generic protein quantification assays such as bichinchoninic acid (BCA) assay or Bradford assay were applied to corona investigation after forced desorption of bound proteins. Experimental protocol simply includes incubation of NPs in protein solution followed by centrifugation to wash off free proteins. Then desorption of proteins was facilitated by destroying the NPs or simply saturating with more affinity ligands [86]. The amount of protein was then quantified by BCA assay where reduction of Cu^{2+} to Cu^{1+} in alkaline solution results in colorimetric reaction of BCA with Cu^{1+}. Although the method is highly compatible with several reagents and

buffers, it fails to be cost and time effective compared to other colorimetric assays such as Bradford assay [66,87]. Yet, as these methods includes separation of protein-NP complex from its original milieu, experimental errors such as pipetting and disturbing the precipitates are inevitable.

2.3.3. Protein Composition

For clinical applications of NPs, corona composition is perhaps one of the most important aspects of protein corona. When NPs are incubated in serum, hundreds of different biomolecules tend to attach the NP surface, therefore characterizing such complicated structure is challenging. To this end, several studies were carried out to profile proteins on NPs surfaces with various methods such as surfactant-based gel electrophoresis (SDS-PAGE) and mass spectrometry (MS). In SDS-PAGE, the corona proteins are loaded in polyacrylamide gel and subjected to electrical field resulting migration from one end to another. The rate of the transport through the gel depends on the molecular weight of protein. After separation, proteins can be stained with Coomassie blue for visualization followed by densitometry analysis for quantification of each proteins' abundance. In MS based methods, except for some studies with polymeric NPs [93], generally proteins are detached from NPs first and then digested with the help of trypsin. The resulting small peptide fragments are ionized in the spectrometer and the data is reconstructed to obtain each protein identity. Although conventional MS can be used to identify proteins, quantitative MS was developed either by labeling the peptide fragments with isotopes or counting the chromatographic peaks in a label-free manner [84]. This method can also be combined with SDS-PAGE in order to determine the protein profile more reliably [86].

2.3.4. Protein Binding Kinetics and Thermodynamics

Protein binding to NPs' surface is generally governed by the combination of various physical forces, such as electrostatic interactions, Van der Waals interactions, London forces and hydrogen bonding [15]. Electrostatic interactions are believed to be the primary forces that bring NPs and proteins together followed by the secondary interactions occur largely due to Van der Waals forces and hydrophobic interactions. If the hydrophobicity of NPs surface is large enough, hydrophobic interactions can cause opening up the secondary structure of protein and thus result in losing the protein conformation. The degree of the involvement of these interactions may depend on the size and surface functionality of NPs [94]. From a thermodynamic point of view, proteins are attaching the NPs surface spontaneously with a certain binding energy (ΔG). High values of ΔG represents strong binding with comparatively slower rate of desorption (k_{off}). The protein layer comprised of strong binding was termed as 'hard corona' with up to 8 hours of residing according to some studies with NIPAM/BAM copolymer NPs [88]. In contrast, soft corona is mostly characterized as secondary layer of proteins on NP surface where protein – protein interactions are more pronounced and direct NP surface attachment is rare. It is widely accepted that while hard corona can stay intact during cellular internalization process, soft corona is quickly replaced with the intracellular proteins after endocytosis, therefore considered relatively less relevant in functional responses of NPs [96].

The characterization of this dynamic interaction between NP and proteins provides fundamental understanding of binding in terms of thermodynamics and kinetics. Also, determination of binding affinities and stoichiometry established the grounds of bottom-up approaches to design nanomaterials with tunable protein corona. For
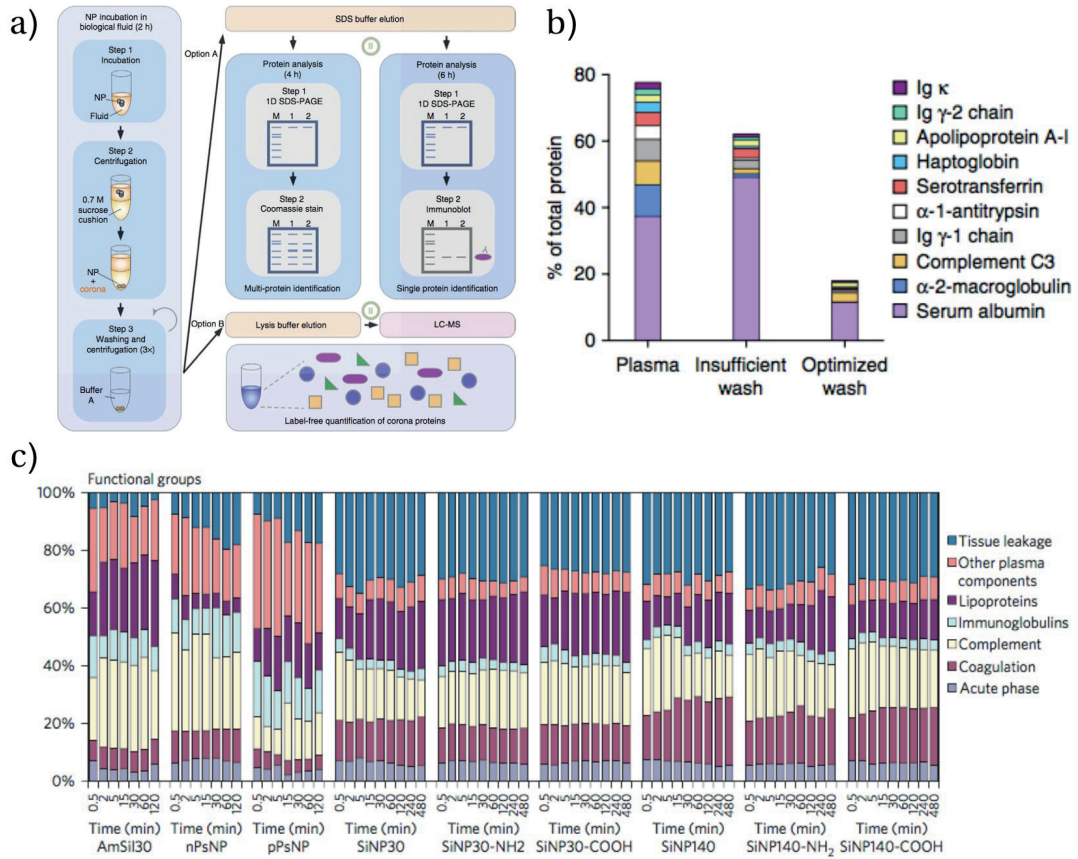
Figure 2.3: a) Workflow of preparing protein corona for further analysis. Followed by incubation with proteins, nanoparticles are centrifuged down and washed to clean from free proteins. Adsorbed proteins, then either applied to SDS-PAGE for separation or inserted into lysis buffer solution for subsequent LC-MS analysis, an exemplary result of which was shown in b) (Ref. [86] with the permission from The Nature Publishing Group). c) protein profiling with LC-MS analysis can reveal a vast amount of information about protein corona and its formation kinetics. Here a rapid formation of protein corona was demonstrated with LC-MS analysis. Ref. [89] with the permission from The Nature Publishing Group.

this motivation, several methodologies have been suggested to characterize thermodynamic and kinetics parameters of particular protein – NP pairs.

In terms of interaction kinetics, earlier, Dawson *et. al.* pioneered on applying size exclusion chromatography (SEC) separation method in determination of adsorption/desorption rates for protein attachment to NPs [98]. The elution profile of NP-protein mixture is typically dependent on flow rate, NPs' mass as well as dissociation rate of proteins. In case of slow dissociation, proteins stay at NPs surface during the elution and form bands similar position with NPs alone. In contrast, fast dissociated proteins rather fall behind and keep their position similar to protein injected alone. Intermediate rate constants result in divided or smeared bands in the column. Comparison of the positions of proteins after elution with simulated chromatograms allow to calculate rate constants for each protein that are identified in SEC. Surface plasmon resonance (SPR) is another early method to detect kinetics of protein attachment to NPs surface. Traditionally SPR has been utilized for protein-protein kinetics where one protein is fixed on a gold substrate layered on a glass support *via* covalent bond, while the other protein solution is introduced. Subsequent refractive index change on the surface as the molecules bind can be modeled with respect to time ($R(t)$). Again, Dawson's lab modified traditional SPR such that NPs are fixed on glass substrate through thiol – gold chemistry and protein of interest was added which was used to calculate association rate. After saturation, simple washing with buffer revealed the dissociation kinetics with pretty much same way.

As per the thermodynamics of protein binding, several methods have been applied calculate binding affinity constants and binding stoichiometry. Isothermal titration
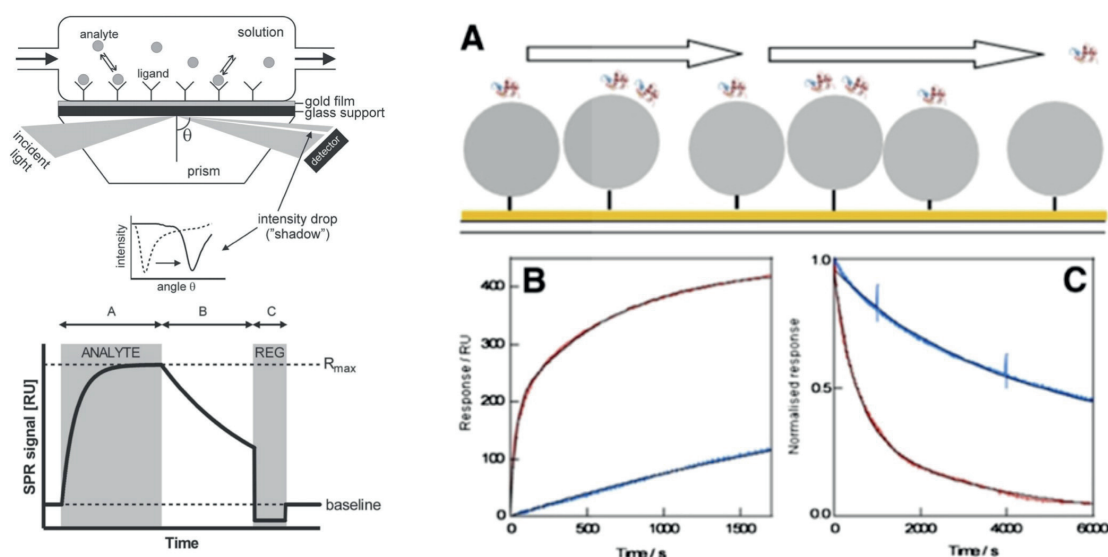
Figure 2.4: a) Kinetics of protein-nanoparticle interactions can be measured with surface based methods, such as surface plasmon resonance. a) By flowing a protein solution, the refractive index change can be measured upon binding of protein to surface fixated nanoparticles. An example of such study was given in b) where NIPAM:BAM polymeric nanoparticles and BSA interactions were measured. Note that the kinetics of binding is highly dependent on the hydrophobicity of the nanoparticles as shown with NIPAM:BAM ratio of 85:15 (blue curve) and 50:50 (red curve). Ref. [99] with the permission of Elsevier.

calorimetry (ITC) has been adapted from protein-protein interactions to measure the affinity through enthalpy of binding. In this technique, protein solution is typically added to NP solution and the heat exchange is measured as two parties interact with each other. Although the method is quite sensitive and versatile for protein-protein or protein-small molecule interactions, it poses practical hurdles in case of NPs due to tendency of aggregation and inaccurate concentration estimation. Plus, the stoichiometry is more ambiguous term for NP-protein complex than a well-defined

protein-ligand complexes (as it can go up to hundreds per NP) which is not modeled quite efficiently in ITC softwares. Quartz crystal microbalance is a fixed surface based method where the change in the overall mass of the substrate can be measured by highly sensitive piezoelectric microbalance. For example, MUA coated NPs are fixated on the substrate and BSA protein solution flow administered. Surface coverage over time creates Langmuir adsorption isotherm which can be modeled in terms of stoichiometry of protein per NPs [100].

2.4. Conclusion

Protein corona is a crucial phenomenon for NPs that are employed in nanomedicine. The implications of protein attachment to NPs surface can be dramatic and manifest as hindrance of targeting abilities as well as altering the biodistribution of NPs. Various characterization methodologies were suggested to shed light on NP-protein interactions from different perspectives such as thermodynamics, kinetics or protein composition. Dynamic nature of these interactions and inherent heterogeneity in NPs structure, on the other hand, make conventional ligand-protein binding methods impractical or at least subject to adaptation for NPs. Yet, there is an urgent need for more robust techniques with better defined interaction scheme particularly for thermodynamics, kinetics and mechanism. The rest of the thesis will try to fulfill some of these needs with novel methodologies such as analytical ultracentrifugation.

CHAPTER 3

3. ANALYTICAL ULTRACENTRIFUGATION AS A NANOMATERIAL
CHARACTERIZATION TOOL

Rapid development of novel nanomaterials for nanomedicine applications have necessitated thorough characterization methodologies to build proper structure-property relationships. Currently there is not a one-method-for-all approach but rather different techniques are combined to fully describe NPs' size, density, shape, ligand shell and surface charge. However, techniques that provide multimodal information from minimum amounts of experiments are highly sought after to attain high reliability with less time. This chapter discusses an example of such technique called analytical ultracentrifugation (AUC) which forms the basis of the works in this thesis. The working principle of AUC will be mentioned in the beginning followed by detailed literature examples of its application for NP characterization in different aspects.

3.1. Historical Perspective of Analytical Ultracentrifugation

More than a century ago, Theodore Svedberg, in his PhD dissertation, provided convincing evidence for the validity of Einstein and Schumolowski's mathematical description of particles' motion in liquid environment (Brownian motion) [53,54]. Later, he and his co-workers devised a centrifugation-based approach to monitor the effects of Brownian motion of colloids as opposed to directed centrifugal force. This

'ultracentrifugation' approach enabled them to analyze very small colloids (in the order of 10 nanometers) that were extremely difficult to sediment at that time. Additional optical apparatus was implanted in the centrifuge to track the solution under high centrifugal field which founded the basis for AUC. From the start, AUC simply paved the way for characterization of any small solutes from synthetic macromolecules to NPs, however, it gained huge popularity in academic research only after it was shown to be versatile tool for protein characterization. For the first time, Svedberg showed that a protein solution is homogeneous and have well-defined molecular weight which was contrarian to the common conception. He was awarded Nobel Prize 1926 in recognition of his pioneering centrifugal studies of proteins and other colloids.

Then, AUC has been a powerful tool for biophysicists to characterize hydrodynamic properties of biomolecules and polymeric systems particularly as a result of rapid developments in biotechnology field. Together with the recent advancements on nanotechnology, AUC became once more an important nanomaterial characterization method in colloidal form. Density and molecular weight-based separation in AUC allowed a wide range of applicability for NPs from 5000 nm to lower than 1 nm sized species. The possibility of using diverse set of solvents (from organic to aqueous) has rendered large applicability to AUC based characterization experiments.

3.2. AUC Working Principle

In AUC cell, sample solution is subjected to high gravitational fields imparted by centrifugation. After typically less than 10^{-6} s, equilibration is reached between

centrifugal forces, buoyancy and viscous drag, solute particles start moving toward the bottom of the cell with a certain rate which is called sedimentation velocity (Figure 3.1). Svedberg formulated this motion by relating the sedimentation velocity of solute particles with their molecular weight and density while coupling with Stokes-Einstein relation for spherical particles resulted a hydrodynamic size information as a function of sedimentation coefficient (s):

$$\frac{M\,(1-\overline{v}\rho)}{Nf} = \frac{u}{\omega^2 r} = s \qquad (3.1)$$

Evolution of solution's concentration distribution over time during centrifugation was historically monitored with Schlieren optics but more recently Beckman Coulter commercialized XLA/XLI instrument which enables absorbance and Rayleigh scattering optical detection system. Additional detection systems such as fluorescence and multiwavelength absorbance will be discussed later in more detail. The availability of 8-hole Beckman rotors allow to run up to 7 samples simultaneously (1 position is reserved for radial calibration cell). The highest centrifugal acceleration achievable with the current Beckman rotors is around 300,000 g. The instrument can practically operate any temperature between 0 °C and 40 °C, however, one will need to convert the resulting hydrodynamic parameters to the standard values corresponding to 20 °C.

There are two main types of experiments in AUC: (i) sedimentation velocity and (ii) sedimentation equilibrium. Sedimentation velocity (SV) experiments are typically comprised of an initially homogeneous (in terms of concentration) solution that start moving towards the bottom of the sample compartment under centrifugation. This
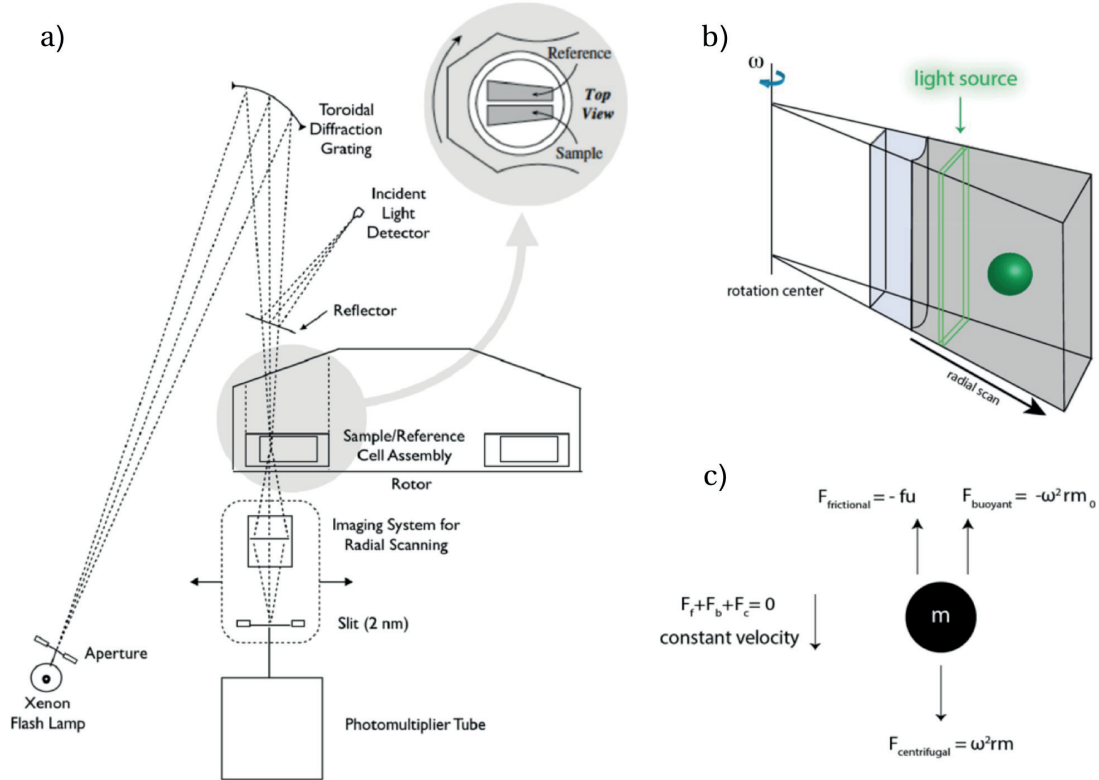
Figure 3.1: a) Schematic view of Beckman Coulter® analytical ultracentrifugation (AUC) composed of three main components: (i) a light source connected to diffraction grating monochromator, (ii) rotor compartment with 8-hole cell holders and (iii) slit assembly for radial scanning. b) in a typical AUC experiment, sample move towards the bottom of a sample container which is sector-shaped in order to avoid convection. c) right after the beginning of sedimentation velocity experiment, three forces come into equilibrium and hence constant velocity of sample.

results a depletion of sample from the liquid – air interphase and create a sharp, sigmoidal shape sedimentation boundary which represents a radial concentration profile $c(r,t)$ in the cell. The rate of the movement of sedimentation boundary is used to calculate the sedimentation coefficient which is directly related to molecular

weight (size factor, *M*) and frictional coefficient (shape factor, *f*). The spread of sedimentation boundary, on the other hand, is attributed to the diffusion of solute particles or high polydispersity of particle size in the sample. Diffusional broadening can then be extracted from the raw data through data analysis protocols. SV experiments are typically conducted at relatively higher centrifugal speeds to completely sediment the whole sample solution during the experiment. However, if the sample goes down too quickly to the bottom, enough scans (in the order of 30-40 scans) might not be collected for reliable data analysis, therefore, it is best to optimize the speed conditions based on the sedimentation characteristics of the sample. In sedimentation equilibrium (SE) experiments, on the other hand, sample is centrifuged with lower speeds but longer times until equilibrium is reached between sedimentation and back-diffusion in solution. Leveraging mass-balance equations, SE type of experiments are mostly used to obtain molar masses, stoichiometry and equilibrium constants of protein-protein interactions [56,57]. Theoretically, SE method is more robust than SV experiments for calculation of molar mass because it does not rely on *a priori* density or frictional coefficient information. Very long experimental times (in the order of days), however, render SE experiments impractical for most NP analysis. Yet, the studies that demand high degree of accuracy are optimal for SE method particularly for studying interactions of monodisperse NPs with other macromolecules.

3.3. Data Analysis Methods

In SV experiments where NPs move towards bottom of the cell relatively quickly, the concentration profile of NPs is mainly affected by two parameters: sedimentation as a result of centrifugation and diffusion due to Brownian motion. The latter term can

impede the accurate estimation of *s*-values particularly for small NPs (less than 30 nm or Mw of 100 000 g/mol) because high diffusion coefficient results in broadening of the sedimentation boundaries. Among multiple data analysis methodologies, there are two common ways of separating the diffusional spreading from sedimentation: (i) Lamm equation modeling (ii) van-Holde Weischet method.

3.3.1. Lamm Equation Modelling

In 1929, Lamm formulated a partial differential equation which describes the evolution of sedimentation boundaries in a sector-shaped centrifugal cell [58]:

$$\frac{\partial c}{\partial t} = D \left(\frac{\partial^2 c}{\partial r^2} + \frac{1}{r}\frac{\partial c}{\partial r} \right) - \omega^2 s \left(r\frac{\partial c}{\partial r} + 2c \right) \qquad (3.2)$$

where *c, D* and *s* are concentration, diffusion coefficient and sedimentation coefficient, respectively. The concentration distribution is represented as a function of time, *t*, angular velocity, ω and radius from the center of rotation, *r*. Lamm equation does not have any exact analytical solutions and historically only approximate solutions were achieved. In such calculations, the effect of back-diffusion and the retardation of radial migration by a rectangular cell walls were usually ignored [59]. Recently, the availability of powerful computers rendered establishing new protocols to solve Lamm equation *via* numerical analysis. Schuck *et. al.* pioneered on implementing software packages such as SEDFIT and SEDPHAT that calculate the sedimentation coefficient distribution function by fitting to the data [90-92]. With the assumption of constant shape factor, i.e. frictional ratio (f/f_0) for all species, the program estimates the Gaussian population for each species'

corresponding *s*-values and provides "*c(s)* distribution". The *c(s)* distribution effectively removes diffusional broadening due to high diffusion coefficients through an empirical scaling relation between *s* and *D* [90]. The peaks on the distribution represents each individual species which are smoothed by regularization protocol. The major advantages of *c(s)* model are excellent resolution and sensitivity, therefore, quantitative characterization of sample heterogeneity and contaminants are highly reliable with this method. On the other hand, the systems that undergo rapid self- or hetero- association/dissociation should be handled with care as it can result incorrect interpretations. One of the important remarks of the presence of dynamically interacting species in sample solution is a systematic noise in the resulting fit, usually identified as diagonal pattern in residual bitmap [90]. Nevertheless, there are available models to analyze such interacting species in the SEDFIT software with more relevant mathematical descriptions [93].

3.3.2. Van Holde - Weischet (vHW)

In order to deconvolute diffusion dependent broadening from sedimentation boundaries, van Holde and Weischet developed a graphical extrapolation method with fast and easily applicable protocol [94]. In theory, as time approaches infinity, all species with different *s*-values would be separated. Therefore, extrapolation of the sedimentation boundaries to infinite time minimizes the diffusion contribution because sedimentation is proportional to time, t, whereas diffusion is to the square root of t [95]. The modern version of the method that is implemented in ULTRASCAN software reliably differentiates heterogeneity in samples and identifies concentration dependent nonideality [96]. Recent advancements made on the software also allows 2-dimensional analysis of sedimentation coefficient and
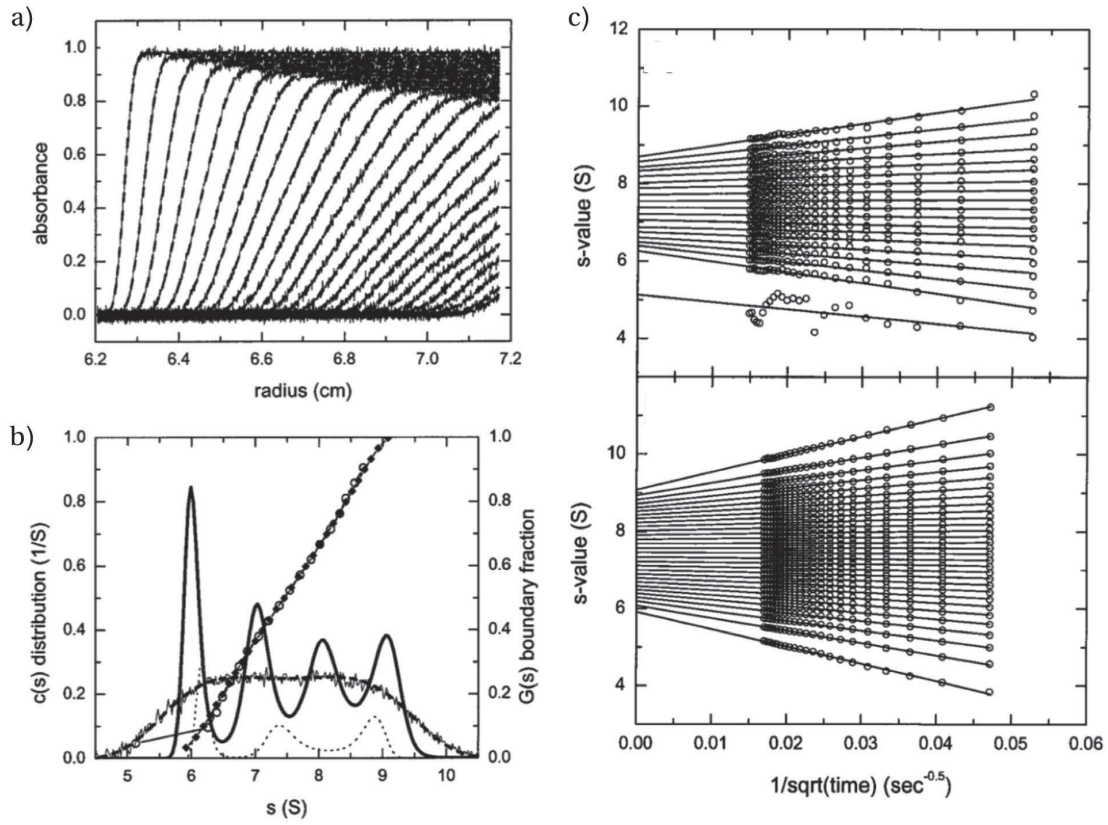
Figure 3.2: a) an example of Lamm-equation analysis of sedimentation velocity experiment. Experimental data points are overlaid with fit line. b) van Holde-Weischet analysis of the same nanoparticles. c) the result of both Lamm-equation and van Holde-Weischet analysis overlaid, ref. [97], permission from Wiley.

diffusion coefficient with the help of generic algorithm and Monte-Carlo analysis (2DSA). It also provides access to computer clusters around the world to speed up the CPU heavy computations as well as data management.

As a reference study, the performance comparison has been recently carried out between data analysis methodologies including time derivative, Lamm equation fitting and vHW/2DSA for SV experiments of colloids by Vittal et. al. [95] (Figure 3.3). ZrO_2 and SiO_2 NPs with different size and shapes were investigated as model objects to show the consistency among various data analysis methods. Small sized, relatively monodisperse ZrO_2 NPs resulted in the same size distribution whereas large and polydisperse SiO_2 NPs indicated noisier values with around 10% shift in the overall size distribution to higher values when 2DSA method is used. It is important to note that, 2DSA method, however, has the advantage of being a model free protocol with no requirements of *a priori* f/f_0 and partial specific volume of the NPs and thus preferable in some cases [98].

3.4. Detection Systems

Most common way of data acquisition is perhaps refractive detection of species in AUC cell *via* interferometer that is commercially available in Beckman Coulter XLA/XLI instruments. Interference data, in fact, are known to be more robust with better signal to noise ratio than absorbance optics. In Rayleigh interference, the concentration dependent signal behaves more linearly at high concentrations compared to light absorption. Although, refractometric methods are advantageous for samples with little optical absorbance, they usually suffer from the lack of selectivity among scanned species in solution. Absorbance based detection systems, on the other hand, employ monochromatic light with any wavelength between 190 nm and 800 nm at high resolution (±1 nm). Such detection methods can effectively monitor different species in solution separately if their light absorption occurs in different part of the spectrum (e.g. gold NPs at 520 nm vs. proteins at 280 nm). More
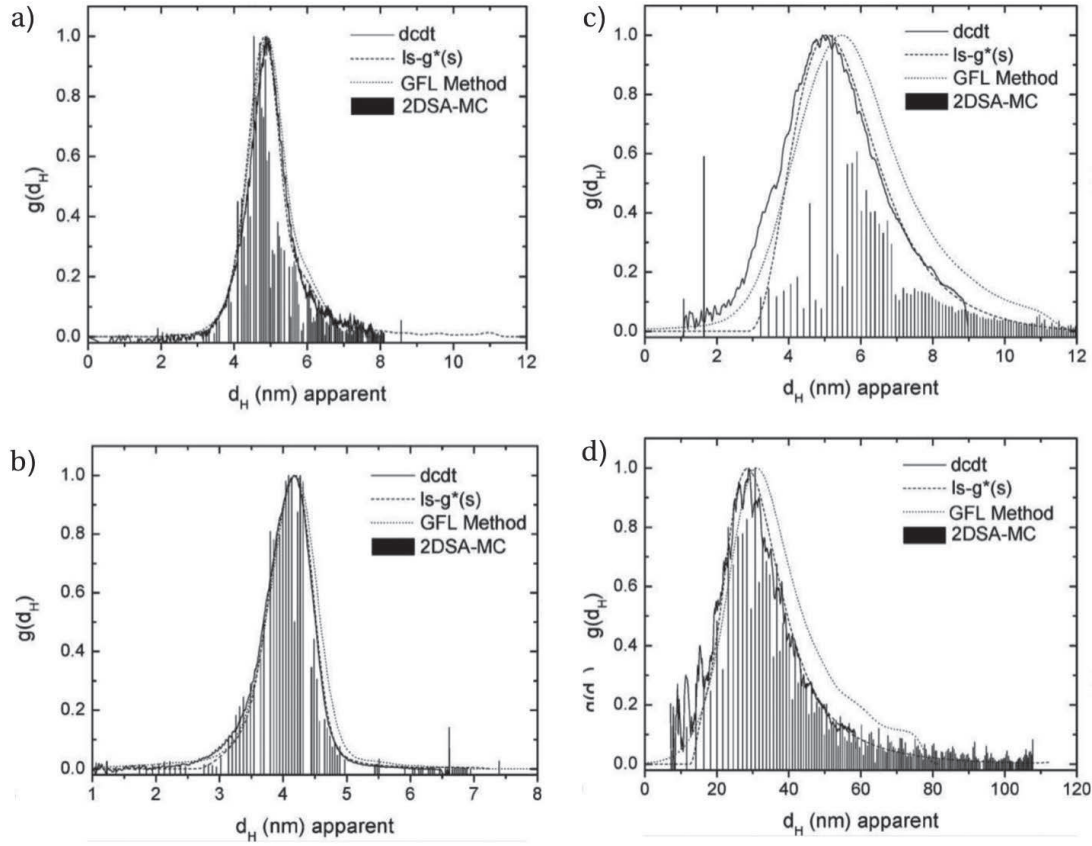
Figure 3.3: A comparison of analysis methods in analysis of hydrodynamic diameter analysis of ZrO_2 nanoparticles of a) spherical and b) non-spherical shape as well as SiO_2 of c) 5nm and d) 30nm size. Note the correlation of analysis methods for small ZrO_2 regardless of their shape being spherical or not. However, for SiO_2 nanoparticles, there is a discrepancy in ls-g(s) method. Ref. [95] with the permission of Wiley.

recently developed fluorescence detection system also offers unique advantages particularly for trace amount of materials due to its high sensitivity [99]. For example, fluorescence detection can analyze concentrations as low as 300 pM for fluorescein-like labels [99]. Yet, care must be taken for the inner filter effect which can complicate

data analysis for high concentrations. The radial resolution of fluorescence detector is similar to absorbance optics and SV/SE experiments can be reliably carried out with high accuracy.

In addition to conventional detection methods, as far as NP characterization is concerned, development of multiwavelength absorbance detection system (MWL-AUC) is arguably one of the most important contributions in AUC field [111]. In contrast to up to maximum 3 different wavelengths choice in conventional absorbance optics, MWL-AUC allows to collect the complete UV-Vis spectrum of each species in solution with CCD camera instalment. This enables to create multi-dimensional data with concentration distribution as well as absorption spectrum and therefore isolate sedimenting species at higher accuracy [100] (Figure 3.4). More importantly, MWL detection allows hydrodynamic analysis of anisotropic NPs that has disparate light absorption along different edges such as gold NRs or chirality dependent absorption for a nanomaterial, for instance, carbon nanotubes [101]. In combination with speed ramp experiments, MWL analysis for even highly polydisperse samples can be carried out without complication [102]. All of these advantages substantially increase the potential applicability of AUC in NP characterization studies with the contribution of both Ultrascan and SEDFIT software in which new MWL-AUC data analysis treatment protocol were implemented for end-users [103].

3.5. Sample Heterogeneity and Size Analysis of Nanoparticles with AUC

Particle size distribution analysis is perhaps one of the most crucial part of the jigsaw puzzle for NP characterization. In most of the NPs synthesis, heterogeneity in size,
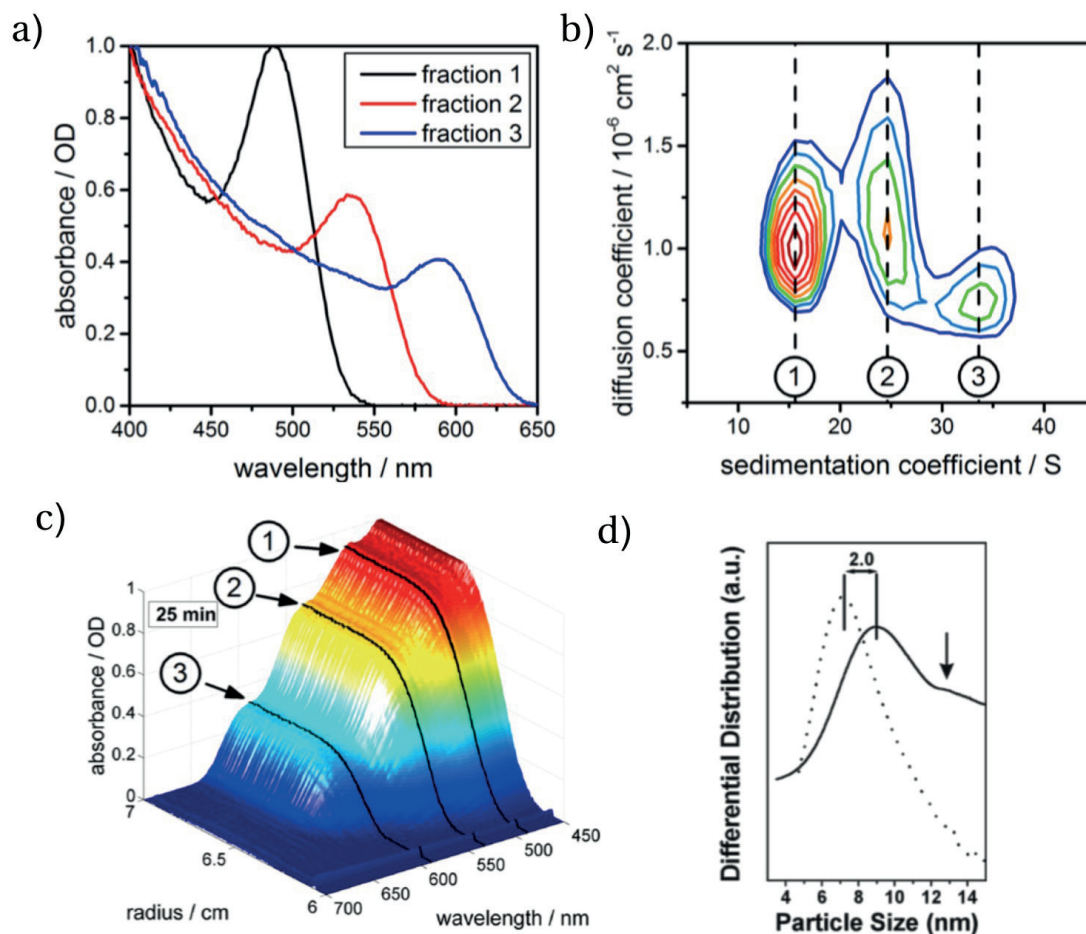
Figure 3.4: a) Size dependent light absorbance of CdTe nanoparticles and b) their 2-dimensional sedimentation velocity analysis at 488 nm using $c(s,f/f_0)$ method. c) Multiwavelength spectra of CdTe nanoparticles mixture. The three species with their individual absorbance spectra and sedimentation rates are clearly distinguishable. Ref. [101] with the permission of The American Chemical Society. d) An exemplary experiment where nanoparticle ligand coverage is monitored with a 2nm shift in hydrodynamic diameter as shown in AUC analysis. Ref. [104] with the permission of Wiley.

density or shape is almost inevitable. While detecting the sample heterogeneity through microscopic analysis suffers from low throughput and less representative statistics, light scattering methods such as dynamic/static light scattering (DLS/SLS) and nanoparticle tracking analysis (NTA) have become popular choices for bulk characterization of NPs due to easy and fast operation. Low resolution as well as overestimation of larger sized contaminations/aggregates (due to relation between light intensity and sixth power of radius), however, have limited the applicability of scattering methods as well. AUC, on the other hand, offers unique ability to study NPs' heterogeneity as well as size distribution with excellent resolution through sedimentation analysis. For example, a common synthetic protocol that was known to produce highly monodisperse iron oxide NPs, in fact, was found to exhibit at least bimodal distribution according to the SV-AUC analysis [105]. Such behavior was attributed to a premature decomposition of iron pentacarbonyl during the heat treatment which was almost impossible to capture with conventional characterization methods. Carbon nanotubes (CNTs) produced with high purity synthetic protocol was also shown to have trace amounts of bundles within a large population of individual monodisperse CNTs [106]. In addition to the detection, it is possible to calculate the relative concentrations of different species in s-value distributions provided that light absorption is size independent [107].

Stokes-Einstein equation suggests an apparent correlation between sedimentation coefficient (s) and hydrodynamic size (d_H) and density (ρ) of colloids:

$$d_H = \sqrt{\frac{18\eta_s s}{\rho_P - \rho_s}} \qquad (3.3)$$

With given solvent viscosity (η_s) and solvent density (ρ_s), NPs that do not have broad density distribution can be assumed to have constant density value, thereby size distribution can be estimated. For example, most organic NPs have relatively similar density which do not depend on the size. Therefore, SV experiments have been applied to various types of polymeric NPs and carbon nanodots to obtain high-resolution size information with constant particle density [108-113].

The fact that AUC can track slight changes in size allows to confirm even chemical modifications made on the NPs surface. For instance, a ligand exchange reaction protocol with glutathione to atomically precise *p*-mercaptobenzoic acid (MBA) coated Au144 nanoclusters can be tracked with a slight shift in size distribution due to the variation among ligand lengths [114]. Hydrodynamic diameter of AuMBA NPs obtained by SV-AUC (3.6 ± 0.2 nm) was found to be only 0.4 nm less than their glutathione coated counterparts which confirms the ligand exchange reaction [114]. Besides, Mayya et. al. showed the effect of layer-by-layer deposition of oppositely charged polyelectrolytes onto 7 nm diameter gold nanoparticles creating gold core – polyelectrolyte shell NPs [104]. AUC analysis showed a 2 nm increase in hydrodynamic diameter of gold NPs upon coating with two different polymers whereas 4 nm increase was observed when the layer is doubled. The average polyelectrolyte thickness was calculated to be around 0.5 nm.

3.6. Density Analysis of NPs with AUC

Stemming from Stokes-Einstein equation, the previous discussion indicated briefly the presence of strong correlation between size of NPs and their densities for one dimensional *s*-values analysis. That is, a prior knowledge of NP size can render

estimation of density with the help of *s*-values distribution. This type of information becomes highly useful for most of the functional NPs that are composite of multiple materials with core-shell structures. For example, core-shell Si nanocrystals with cyclohexane and allylamine coatings were characterized in terms of size with DLS. SV experiments revealed average *s*-value which was converted into overall effective density of NPs using the size information from DLS [115]. Fielding et al showed the presence of density distribution of core-shell polystyrene-silica nanocomposites (polystyrene core silica shell) and coupled with disk centrifuge photosedimentometry and SAXS to calculate the density quantitatively [116]. However, in case of no prior size information, analysis of *s*-values in solutions with different densities by mixing two different solvents or simply increasing heavy water content would still allow to estimate colloids' densities independent from their sizes. [115,117].

The overall density of most core-shell NPs is defined by a volume average of core density and ligand shell density. Therefore, in case of inorganic/metal core and organic shell NPs, any change in ligand shell identity, structure or grafting density should directly be projected in *s*-values distribution due to the overall NP density change [118,119]. For instance, Falabella et. al. reported the characterization of gold NPs coated with thiol-terminated single stranded DNA using AUC [120]. A monotonic decrease in *s*-value distribution of gold NPs was observed with increasing number of thymidine residues in ssDNA ligand which was related to the length of the whole ssDNA attached to the NPs. Additionally, the ligand packing density effect on the stability of NPs was detected as slight decrease in *s*-value of the NPs with increasing packing density of ssDNA ligands [120]. Similarly, grafting density of PEG on gold NPs could be quantitatively estimated assuming a hard-sphere NP model [121]. A pH
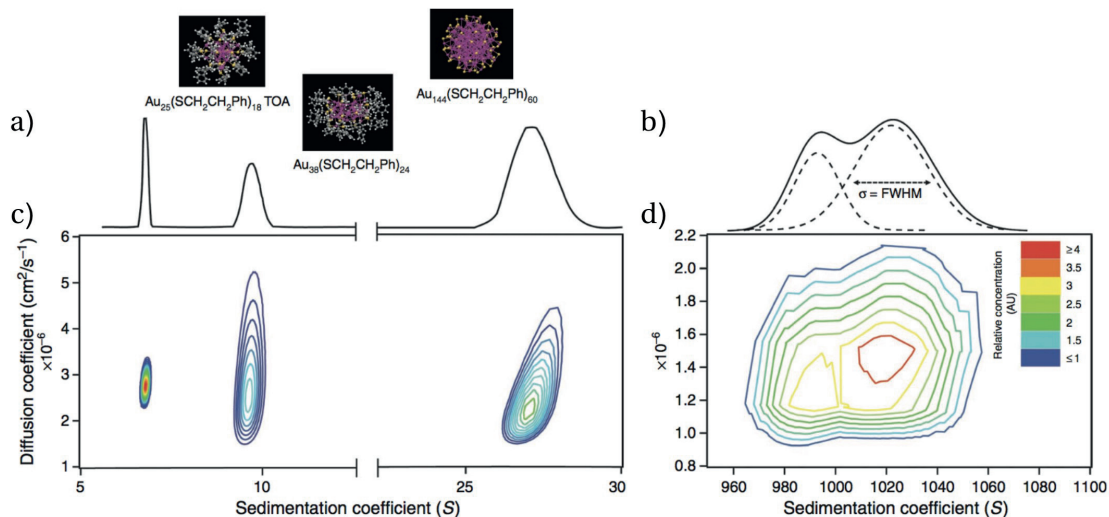
Figure 3.5: a) Separate gold nanoclusters were characterized with *c(s,f/f0)* method. b) Owing to high resolution of AUC, even moderately monodisperse nanoparticles can be further resolved in different distributions. Ref. [122].

dependent swelling/contracting abilities of such composite NPs was also monitored with *s*-values evolution [123]. Surface passivation of CNTs require adsorption of surfactant molecules, therefore, the degree of adsorption or the packing density of surfactants is a crucial parameter for colloidal stability of CNTs. With similar methodology, SV experiments allowed to determine ligand packing density of CNTs and various surfactants were compared in terms of their coverage and colloidal stability[124,125]. Additionally, salt effect on bile salt surfactant adsorption to CNTs were comparatively studied in the same manner[126].

Recent advancements on data analysis methods and instrumentation decreased the limitations on the priori knowledge and allowed to vary multiple parameters at a

time. Carney et. al. applied two-dimensional *s*- and *f/f₀*- analysis in SEDFIT to create *s*- and *D*-distribution of gold nanoclusters [122] (Figure 3.5). The average *s*- and *D*-values were then converted to hydrodynamic density, molecular weight as well as hydrodynamic diameter for NPs out of only one AUC experiment [122]. More strikingly, the methodology is not only limited to extremely monodisperse NPs (in this case, atomically precise gold nanoclusters were used to demonstrate the validity of the method), but also can be applied to polydisperse samples where separate *s*- and *D*-values for individual distributions can be calculated and converted into hydrodynamic parameters. In various nanocluster studies afterwards, the *c(s,D)* approach to calculate molecular weight of magic size nanoclusters was preferred over mass spectroscopy analysis due to higher sample throughput, information rich outcome and the possibility to see extremely small variations from aggregates [127-130]. Walter et. al. has also reported parametrically constrained spectrum analysis (PCSA) in Ultrascan to be highly useful for NPs to vary any two of five parameters (density, *s*, *D*, *f/f₀*, molecular mass). This method creates grids depending on the parameter varied in a mathematically constrained manner so that artefacts and false positives can be avoided [131].

3.7. Conclusion

Although historically AUC has been utilized for protein characterization, recent attempts show it can be highly valuable tool for investigating colloidal properties of NPs as well. Different data analysis methods are available for users with large amount of resources for learning. A quick AUC analysis can give information pertaining to sample heterogeneity and aggregation behavior whereas more detailed investigation can also be done to calculate hydrodynamic size and density of NPs. AUC offering

robust, high resolution and powerful characterization method for colloids, can also be used for investigation of NP-protein interaction analysis. The description of such methodology will be discussed in the next chapter.

4. MATERIALS & METHODS

In this chapter, experimental details on synthesis, size separation and characterization of NPs will be presented. In addition, some remarks on the efficiency of size separation of gold NPs with respect to mixed-ligand monolayer nature will be pointed out.

All chemicals and solvents were purchased from Sigma Aldrich and used without further purification unless otherwise stated. Optical spectra were acquired with an Ocean Optics USB2000+UV-VIS spectrophotometer.

4.1. Synthesis of Materials

4.1.1. Synthesis of 11-mercaptoundecane sulfonate, sodium salt (MUS)

The synthesis of MUS ligand was adapted from Dr. Paulo Jacob Silva who extensively worked on the optimization of the synthesis for highest purity. Although I synthesized some of the MUS ligand, his MUS ligands also contributed a lot to one-phase synthesis of NPs used in this thesis. More detail on MUS synthesis therefore can be found in the PhD dissertation of Dr. Paulo Jacob Silva, EPFL, 2016.

Sodium undec-10-enesulfonate: 11-bromo-1-undecene (56 mmol) was dissolved in a mixture of 300 mL of methanol:water mixture in approximately 1:2 volume ratio.

Benzyltriethyl ammonium bromide (10 mg) and sodium sulfite Na_2SO_3 (114 mmol, 14.4 g) were added. The mixture was refluxed at 105°C for 48h. Workup was done with plenty of diethyl ether extraction followed by drying. The powder was dissolved in approximately 200 mL methanol and filtered to wash away insoluble salt residues. Remaining solution was dried in rotary evaporator. This step was repeated twice to make sure the resulting powder is free from salts. ^{1}H-NMR (D_2O): 5.76 (m, 1H), 4.78 (m, 2H), 2.69 (t, 2H), 1.53 (m, 2H), 1.11 (br s, 12H).

Sodium 11-acetylthio-undecanesulfonate: Sodium undec-10-enesulfonate (10 g, 46 mmol) was mixed with thioacetic acid (9 mL, 128 mmol) in 150 mL methanol under UV lamp for 16h at room temperature. The solvent was evaporated followed by multiple washing/filtering steps with diethyl ether until yellowish-white colored powder is obtained. The solid was dissolved in methanol and about 3 g of carbon black was added to the solution, and the mixture was filtered through celite in a fluted filter paper. This step is repeated until clear solution is obtained. Finally, all the solvents were removed with resulting white powder. ^{1}H-NMR (D2O): 2.69 (t, 4H), 2.17 (s, 3H), 1.53 (m, 2H), 1.39 (m, 2H), 1.11 (br s, 14H).

11-mercapto-1-undecanesulfonate: Sodium 11-acetylthio-undecanesulfonate was refluxed at 105°C in 150 mL of aqueous 1M HCl solution for 16 h. 200 mL of 1M aqueous NaOH was then added to the final solution for neutralization. The clear solution was put in 4°C fridge and crystallized over a week. The white solid was centrifuged down in 50 mL falcon tubes, and dried under high vacuum. ^{1}H-NMR (D2O): 2.69 (t, 4H), 2.34 (t, 3H), 1.53 (m, 2H), 1.39 (m, 2H), 1.11 (br s, 14H). Calculated mass 290.42 g/mol.

4.1.2. Nanoparticle Synthesis

4.1.2.1. One-phase Method

In a typical one-phase synthesis, 0.3 mmol of gold chloride trihydrate (HAuCl$_4$ 3H$_2$O) in 75 mL ethanol and 0.3 mmol of desired thiolated ligand mixture in 20 mL methanol was mixed at room temperature for about 15 min. 600 mg of sodium borohydride (NaBH$_4$) in 50 mL ethanol was added dropwise with immediate formation of NPs characterized by black color. The solution was mixed for an additional 2 h at room temperature for completion of reaction. Gold NPs were removed from solution and washed with methanol 4-5 times via centrifugation at 5000 g for about 5 min. NPs were then dried under high vacuum obtaining around 120 mg of black powder. In order to wash NPs from inorganic salts, NPs were dissolved in 15 mL of DI water and washed with Amicon® centrifugal dialysis filters (10kDa MWCO). 4 mL of acetone was added to the resulting concentrated aqueous solution of NPs and were centrifuged down with preparative ultracentrifugation at 55krpm (SW Ti 55 rotor, Beckman Coulter). The pellet was dried under high vacuum and stored as powder for further use.

4.1.2.2. Stucky Method

Water soluble gold NPs: 124 mg chloro(triphenylphosphine) gold(I) was dissolved in 90 mL 9:1 DMF:H2O mixture. In a separate vial, 0.32 mmol of a desired mixture of ligands was dissolved in 20 mL 1:1 DMF:H2O mixture and added to the gold solution at room temperature. This mixture was put into a heating bath at 125 °C and after ~5 min, 140 mg of borane tertbutylamine complex (BtBA) in 10 mL 1:1 DMF:H2O

mixture was added at one portion. Following an almost immediate color change, the reaction was completed after 2 h. The solution was cooled down to room temperature and 200 mL of acetone was added. The flask was placed into a 4 °C fridge overnight for precipitation. NPs were cleaned with methanol 3 times and then dissolved with deionized water for further was with Amicon® Ultra-15 centrifugal filters (30kDa cutoff). 4 mL of acetone was added to the resulting concentrated aqueous solution of NPs and were centrifuged down with preparative ultracentrifugation at 55krpm (SW Ti 55 rotor, Beckman Coulter). The pellet was dried under high vacuum and stored as powder for further use.

Synthesis of OT coated hydrophobic gold NPs: 104 mg chloro(triphenylphosphine) gold(I) and 80 uL OT were dissolved in 16 mL chloroform:toluene mixture. In a separate vial, BtBA (200 mg) was dissolved in 16 mL chloroform:toluene mixture and added to the previous solution at room temperature. Immediately after, the reaction flask was put into a heating bath. The reaction was allowed stirring for 1 h for completion. The solution was slowly cooled down to room temperature and approximately 30 mL methanol was added and kept at 4 °C fridge overnight for precipitation. The particles were collected and washed with methanol 4-5 times with centrifugation. The resulting NPs were dried under high vacuum at least overnight prior to use. Varying the volumetric ratio of chloroform and toluene in the synthesis as well as the temperature were found to produce different sizes of NPs in high degree of monodispersity. These experimental parameters and their resulting sizes were summarized in Table 4.1.

Table 4.1: OT coated nanoparticles synthetic conditions that are used to obtain different sizes.

Size Obtained (nm)	Chloroform (%)	Toluene (%)	Temperature (˚C)
4 ± 0.5	100	0	55
5 ± 0.6	50	50	55
6 ± 0.8	50	50	85
6.5 ± 0.8	25	75	85
7 ± 1	25	75	115

4.1.2.3. Ligand Exchange Reactions

Typical ligand exchange reactions to obtain water soluble NPs were as follows: 10 mg of OT coated NPs were dissolved in 10 mL chloroform in a glass vial. While stirring vigorously, around 15 mmol of hydrophilic ligand (for example MUS) dissolved in 10 mL DI water was added to the previous solution. The two-phase mixture was vigorously stirred overnight until a complete phase transition of NPs from organic phase to aqueous phase was observed. NPs were carefully removed with a glass pipette and washed thoroughly with DI water using Amicon® centrifugal dialysis devices (10 kDa MWCO). The hydrophilic ligand content on NPs surface could be adjusted with varying amount of ligand concentration added to OT coated NPs in the synthesis. In case of 11-mercapto undecanoic acid coated NPs, the pH of the aqueous ligand solution was adjusted to 10 with NaOH prior to initiating ligand exchange to ensure the solubility of resulting NPs.

4.2. Characterization of Nanoparticles

4.2.1. Core Size and Hydrodynamic Size

Transmission Electron Microscopy (TEM) has been used for determination of core size of NPs and size distribution analysis. NP sample solutions were simply put on carbon coated TEM grids via drop casting method and air dried without blotting. Nanoparticle core sizes were analyzed by Transmission Electron Microscopy (TEM) on a Philips/FEI CM12, with an LaB6 source at 120 kV accelerating voltage. Image analysis is made with ImageJ analysis software with a custom-made macro by Dr. Marie Müller to combine all individual image analysis of the same sample.

In order to test heterogeneity in sample with higher resolution, AUC experiments were carried out for each NPs batch. NPs are dissolved in water or 10 mM phosphate buffer at a concentration where surface plasmon absorption corresponds to between 0.5–1.5 OD range. For sedimentation velocity experiments, minimum 300 uL were used to obtain higher data resolution in sedimentation analysis. The rotor speed was varied within 3 krpm up to 40 krpm depends on the NPs size and colloidal stability so that at least 30-40 scans could be acquired before complete sedimentation of the sample. For example, citrate NPs (14 nm) were analyzed at 3 krpm while ultrasmall gold nanoclusters of 1.5 nm core diameter entailed higher than 30 krpm for proper sedimentation. AUC was performed using a Beckman Optima XL-A (Beckman, Spinco Division, Palo Alto, CA), An-50 Ti or 60 Ti rotor, scanning absorbance optics, with 12 mm path length double sector centerpieces with sapphire windows. Absorbance wavelength has been chosen according to the sample's LSPR characteristics to get the highest light absorption possible. For example, gold NPs of
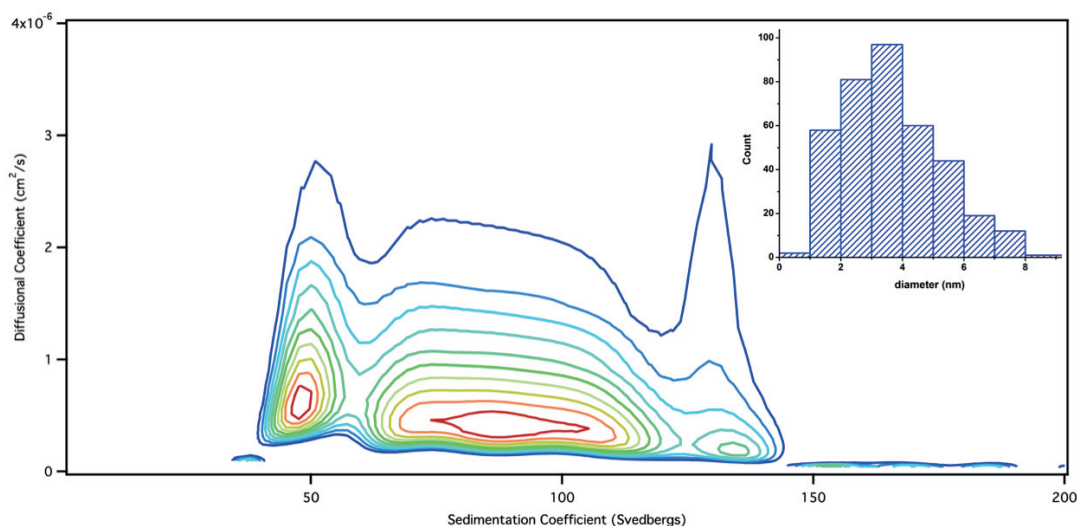
Figure 4.1: A *c(s,D)* analysis of MUSOT nanoparticles produced with one-phase method. Note at least 4 distinct distribution which is practically invisible in TEM analysis (shown in the inset).

larger than 2 nm, 520 nm was chosen while gold nanoclusters were monitored at 400 nm as they are lack of LSPR peak at around 520 nm. All experiments were carried out at 20 C with 0.006 cm radial step size. Before doing size analysis, samples were run at various concentrations to investigate the presence of concentration dependent sedimentation which may complicate the size analysis. In such case, ionic strength of solution is adjusted to find ideal sedimentation range for NPs. For data analysis, SEDFIT from Peter Schuck was exclusively used with *c(s,ff$_0$)* analysis followed by subsequent calculation of average sedimentation and diffusion coefficient values with custom made Matlab script written by Dr. Randy P. Carney. In some cases, however, ULTRASCAN by Borries Demeler was the choice of software as it allows to vary more parameters in two-dimensional space such as sedimentation coefficient vs density of NPs. 2DSA with ULTRASCAN was found to be more sensitive to

heterogeneities and higher resolution compared to SEDFIT which becomes advantageous in most cases.

4.2.2. Ligand Packing Density

Investigation of the packing density of self-assembled monolayers of gold NPs by thiolated ligands is crucial as it can affect the surface characteristics dependent biophysical behavior of NPs. For this, TGA was exclusively used to determine mass-based ratio of organic ligand shell on gold NPs (Figure 4.2). In a typical TGA experiment, small amount of NP sample in powder form (around 5-10 mg) is put in Teflon® crucibles under nitrogen gas flow. The temperature of the crucible is ramped up at a slow rate (in my experiments, 5 °C per minute) while the mass of the sample is measured with high sensitivity. The organic shell of NPs is burnt between 200 – 500 C, while pure gold element stays in the sample container. In most cases, temperature increased up to 900 C where no organic molecules are remained on NPs surface as characterized by a plateau in mass change curve. For MUSOT NPs, two distinct weight decreases were observed at 240 °C and 450 °C corresponding to OT and MUS ligands respectively as confirmed by the TGA experiments with only organic ligands. The molar ratio of MUS and OT can be semi-quantitatively calculated based on the height of each drop by converting the mass to molarity by using molar masses of each ligands. However, comparison with NMR analysis revealed that this methodology may have inherent errors mainly emanating from instrumentational errors and broadened decomposition curves which complicates the determination of accurate beginning and ending decomposition points for each ligand. On the other hand, organic coverage can be more reliably calculated by simply calculating mass loss with respect to weight of the gold core. This type of analysis demonstrated 10-12% in

54
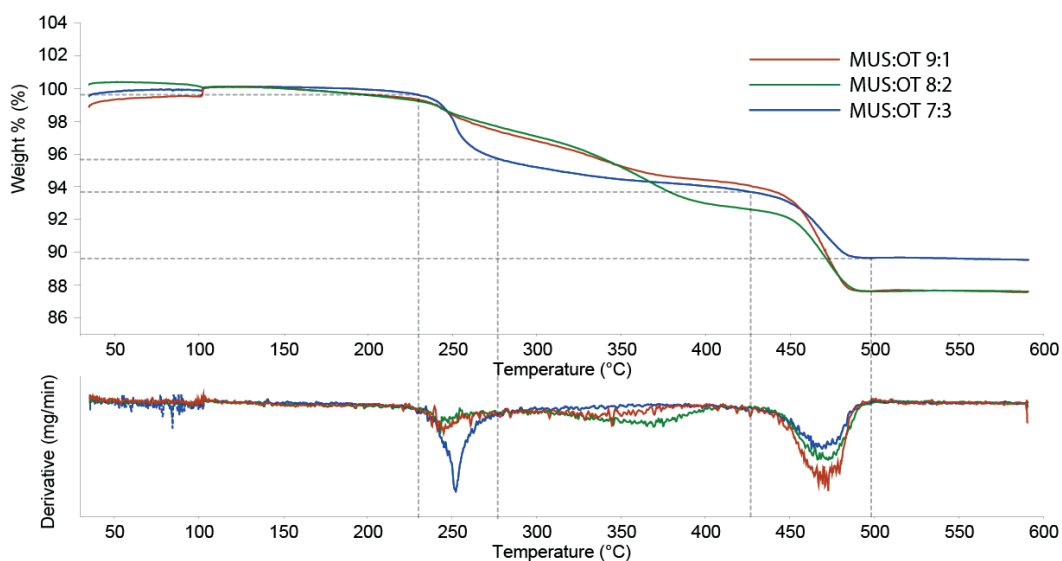
Figure 4.2: Thermogravimetric analysis (TGA) of three different MUSOT batches with varying MUS:OT ratio. Although it is difficult to separate MUS and OT completely from these curves, depending on the ratio, weight loss curve might show difference overall.

weight loss in most MUSOT and allMUS NPs which was converted to average ligand packing density of 3.2 – 3.8 ligands per square nanometer on NP surface. Notably, organic coverage seems not following a monotonous trend with the ligand ratio of MUS:OT. However, it has to be kept in mind that this calculation was done with the raw batch of particles that has a broad size distribution, i.e. based on average diameter (3.7 nm). More detailed analysis with more homogeneous samples is necessary to reach the dependency on NPs' ligand ratio and their ligand packing density.

4.2.3. Surface Ligand Composition

1H NMR spectrometry offers highly valuable information on NPs purity and molar ratios of ligands on NPs surface. All ^{1}H NMR experiments were carried out with Bruker AV-400 Mhz and data analysis were done with Topspin v3.0 or MestreNova Lab. All spectra were subjected to baseline subtraction with these data analysis softwares before integration of peaks. Before investigation of ligand composition on NPs surface, ^{1}H NMR spectroscopy was used to investigate the cleanliness of NPs sample. Simply put, when ligands are conjugated to NP surface, their tumbling rate considerably slows down and thus peak broadening occurs in the NMR spectrum. That is, if ^{1}H NMR analysis of NP solution in deuterated H_2O (or in an organic solvent for hydrophobic NPs) exhibit sharp peaks corresponds to ligands' NMR shifts, the NP solution was considered contaminated with free ligands and further washing steps were carried out.

Second step in ^{1}H NMR analysis is informative predominantly for mixed-ligand NPs, serving as a quantitative method to investigate the molar ratio of corresponding ligands on NPs surface (Figure 4.3). Prior to ^{1}H NMR analysis, all NP powders were put in iodine solution (approximately 10 mg/mL in deuterated methanol or DMSO) and sonicated for at least 30 min. Iodine reacts selectively with Au atoms in the NPs, forming insoluble AuI salt, which in turn releases the ligands on the surface. AuI was then separated from the solution with centrifugation (5000 g, 5 min) and supernatant was used for subsequent ^{1}H NMR analysis. The ligand ratio of MUS and OT on NPs surface was calculated as follows: the peak at around 0.7 ppm is attributed to 3 protons in -CH_3 head in OT. The other peak at around 1.4 ppm is a combination of -CH_2 protons that are second nearest neighbors of –SH terminal (in both MUS and OT)

and –CH$_2$ protons second nearest neighbor to SO$_3^-$ head in MUS. The reason why thiol-end side and sulfonate-end side protons have exactly the same shift was attributed to the solvent DMSO. It is slightly oxidizing agent and during the chemical etching process, half-hour long ultrasonication might have facilitated the oxidation of thiols to sulfonates or sulfates[71]. Decomposition with a different chemical etchant, namely, potassium cyanide results in separate peaks, however, the data quality was much lower due to the occurrence of side products under these conditions. Eventually, by simply integrating these corresponding peaks could quantitatively reveal the relative MUS and OT ratio that are liberated from NPs surface after iodine etching protocol. Importantly, as evidenced by these calculations, the feed ratio of ligands in the initial synthesis and the actual ratio on the NP surface may deviate but follow monotonic correlation. Stabilizing the synthetic conditions (such as ligand to gold ratio, stirring rate, temperature, rate of addition of reducing agent and cleanliness of glassware) contributes to achieving more reproducible synthetic results in terms of ligand ratio. More detailed discussion on ligand feed ratio and actual ratio can be found in Dr. Randy P. Carney (EPFL, 2013) and Dr. Paulo J. Silva (EPFL, 2016) Ph.D. dissertations.

4.3. Size Separation of Nanoparticles

Synthetic protocols of NPs can have different outcome in terms of the overall heterogeneity. For example, one-phase method described above employs ethanol and methanol as main reaction solvent which do not dissolve water soluble MUSOT and allMUS NPs. This results an immediate precipitation of produced NPs and captures in different states of nucleation and growth. Also, sodium borohydride serves as strong reducing agent that reacts vigorously and do not allow time to
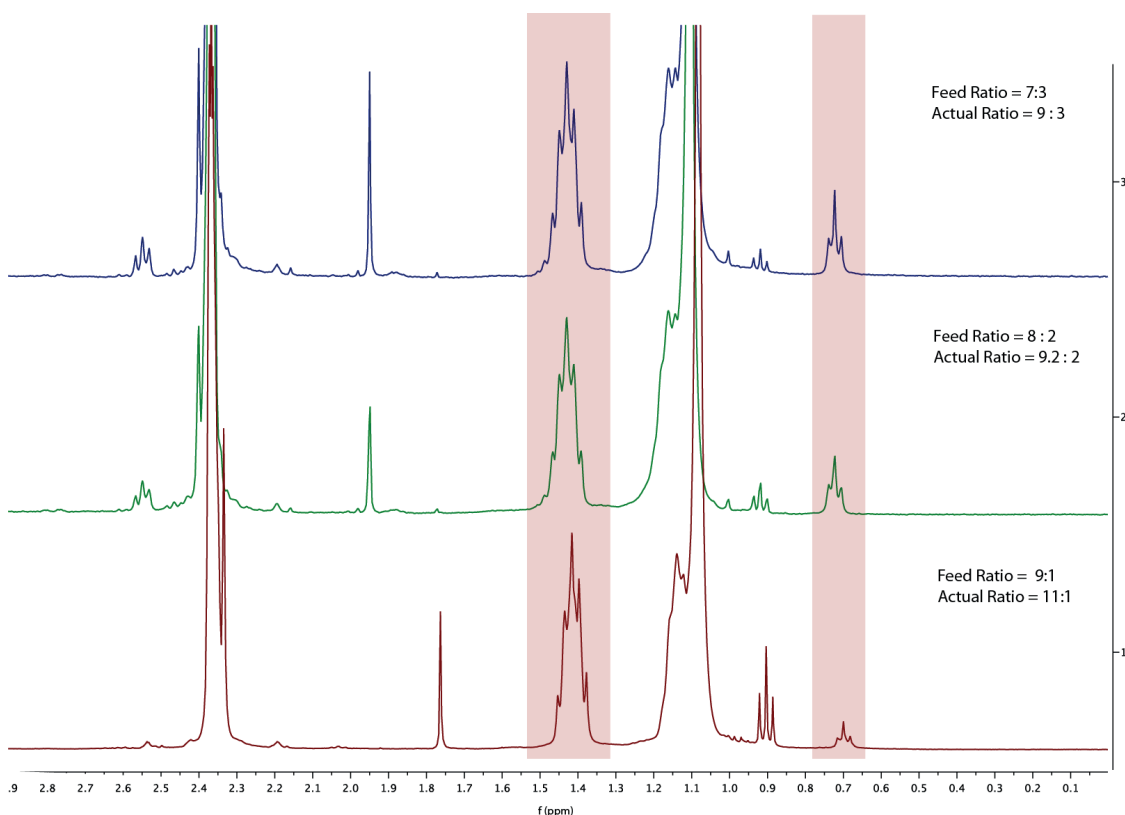
Figure 4.3: Nuclear magnetic resonance (NMR) analysis of etched gold nanoparticles allowed us to reliably calculate the ligand ratio (MUS and OT here). A triplet peak at around 0.7 ppm corresponds to protons in –CH$_3$ terminal of OT while multiplet at 1.4 ppm comes from both MUS and OT.

nucleation and growth for equilibration. These parameters result increased heterogeneity in NPs batch and entails further separation protocol to perfect NPs prior to application. To this motivation, multiple separation methodologies were suggested to obtain homogeneity in NPs samples. Some of these methods exploit specific properties of NPs for size separation, for instance, magnetic susceptibility. Simply manipulating magnetic field around a column allow to separate magnetic NPs

in terms of their sizes and composition because their response to magnetic force is size dependent[132,133]. Other methods such as density gradient fractionation may simply rely on the colloidal behavior differences with respect to size and density as predicted by Stokes-Einstein equation. As size and/or density vary on NPs, their Brownian motion in colloids also change due to their diffusional coefficient changes. Leveraging this relation may enable to separate NPs with respect to size or density depending on the methodology used. In this thesis, density gradient ultracentrifugation (DGU) protocol was used to separate particularly one-phase synthesis NPs which form the most polydisperse batch among the other synthetic protocols.

4.3.1. Fractionation Basics

The basic principle of DGU relies on the correlation between the sedimentation behavior of NPs and their size and density as suggested by Stokes' Law:

$$d = \left(\frac{18\eta_w s_{20,w}}{\rho_p - \rho_w} \right)^{1/2} \qquad (4.1)$$

In this approach, viscous drag is equilibrated by friction and buoyancy of NPs in a colloidal medium while subjected to high centrifugal field. The rate of sedimentation thus depends on the size and density (as well as molar mass) of NPs presents opportunity to be fractionated. Using highly viscous solutions such as iodixanol, PVP, glycerol and sucrose, it is possible to slow down this mobility of NPs as well as separate them because high viscosity prevents different fractions to be mixed again.

Various types of nanomaterials from metal core NPs to single wall carbon nanotubes have been efficiently fractionated with DGU protocol by other laboratories14.

4.3.2. Fractionation Protocol for NPs

Within the framework of this thesis, DGU was extensively used to separate AuNPs, size of which is ranging between 2 nm and 7 nm in diameter. Depending on density and sizes of the materials to be separated, various density gradient media can be employed. Here, sucrose gradients were the primary choice because highly viscous solutions can be prepared to ensure limited diffusional spreading of AuNPs (considering density of gold core is 19.3 g/cm^3). Moreover, sucrose is non-toxic (crucial if NPs are to be used for biological applications) and can be easily washed out through dialysis or centrifugal membranes. In general, 20% (w/v) aqueous sucrose solution was placed on top of 50% (w/v) sucrose solution with a 1:1 volume ratio in a 38.5 mL capacity thin-wall transparent UltraClear® Beckman Coulter centrifugation tubes. The two-phase solution was then mixed with certain angles and speeds to obtain a continuous density gradient with commercial gradient mixer (Biocomp® Gradient Master). Aqueous NPs solution (500 uL, 10 mg/mL) was carefully layered on top of the tube and placed in SW32 Ti Beckman Coulter rotor. The samples were then centrifuged at 32 krpm for 2 h at 20 C with maximum acceleration and deceleration settings. After centrifugation, colored NPs solution was observed smeared along the tube creating continuous bands within. Multiple fractions with 4-5 mm distances were separated by using Biocomp® Gradient Master Fractionator. Sucrose contaminated NPs solutions were finally rigorously washed with DI water using Amicon® centrifugal dialysis devices (10kDa MWCO). The efficiency of washing from

sucrose was judged by subsequent 1H NMR analysis where the absence of sucrose peaks in NMR spectrum was sought after.

4.3.3. Remarks on Fractionation

When NPs do only vary in size, that is, they are coated with only one type of thiolated molecules (homoligand), DGU provides efficient separation. This is due to the fact that as long as the ligand packing density is the similar among different sized NPs, the density only depends on the size and therefore separation by density directly reflects to size separation. I consistently observed this behavior for homoligand NPs such that even after the first fractionation step I obtained high degree of monodispersity (Figure 4.4). However, when mixed ligands are used on NPs, the separation was not as efficient and often times second or even third separation was necessary to obtain a clear separation. This was attributed to the multiple heterogeneity sources such as size and ligands ratio on NPs surface that can affect the density. Furthermore, because I was focused on separation of MUS:OT NPs, the ratio of MUS and OT can dramatically affect the colloidal stability in a way that as OT ratio increases, solubility in water diminished. This may result an increased sedimentation rate in the gradient, resulting small particles travels with larger size particles. In this context, I have observed small NPs (in the range of 2 nm) are 'contaminating' most of the larger size fractions and thus results in less monodisperse distribution. This contaminating effect was alleviated by decreasing the loading quantity of NPs in the gradient with the caveat of obtaining less NPs at the end of separation. When started with higher quantity/concentration, in order to get the same degree of separation, I needed to go through multiple separation steps (running DGU to already separated fractions) which is time consuming as well as decreasing the overall yield again. My conclusion
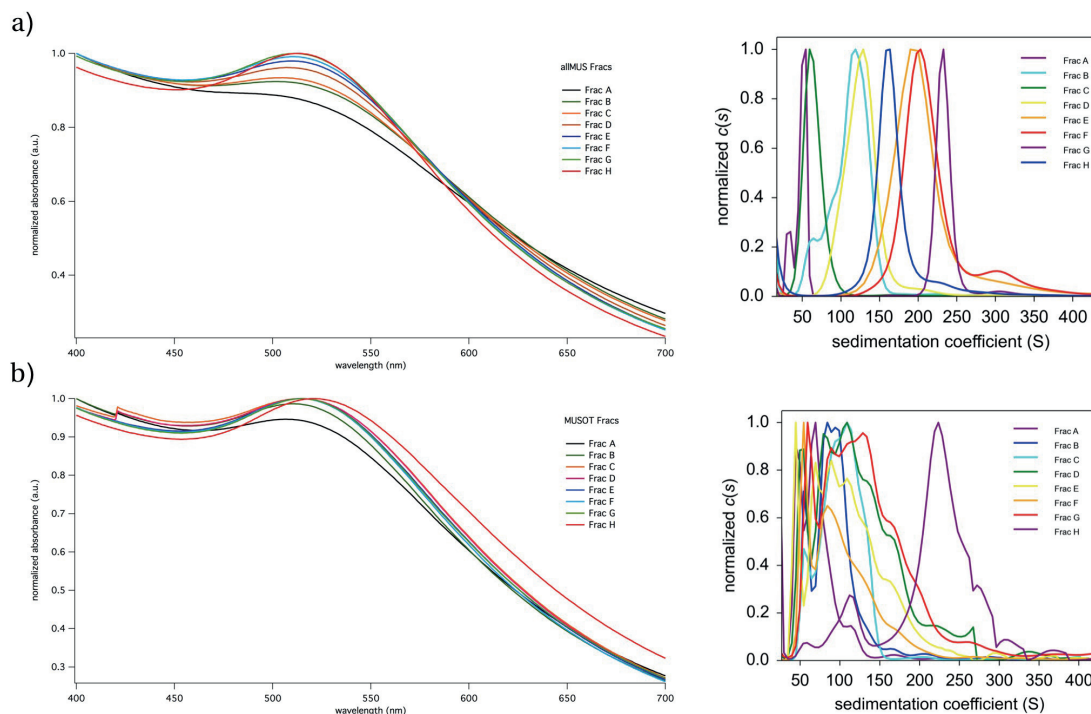
Figure 4.4: A comparison of fractionation results between a) allMUS and b) MUSOT one-phase nanoparticles (NPs). UV-Vis spectra of allMUS fractions show gradual appearance of plasmon peak which is typically dependent on size, whereas MUSOT fractions do exhibit rather mixed behavior. Sedimentation coefficient distributions also demonstrate the monodisperse separation of allMUS NPs in contrast to MUSOT NPs which includes small sized NPs for almost all fractions.

is that separating mixed ligand NPs, particularly the ones having hydrophilic and hydrophobic ligands together on the surface, may not be achieved to a satisfying degree if one needs to have large amounts at the end. Apart from this situation, I find DGU method quite successful and efficient separation methods for gold NPs within the size range of 2 nm to 7 nm.

^{1}H NMR analysis for ligand ratio determination on fractions of one-phase MUSOT NPs demonstrated considerable variation among the fractions in terms of MUS and OT ratio (Figure 4.5). For this particular example, the first two fractions were found to have around 25% OT while third and fourth fractions bore slightly more OT groups. The increase in the OT ratio was more pronounced for larger fractions with around 33% of OT ligands on NPs surface. The change in the OT ligand ratio among fractions evidenced by NMR studies also support the hypothesis of not-so-efficient size separation of mixed-ligand NPs due to their heterogeneity in hydrophilic/ hydrophobic ligand ratio.
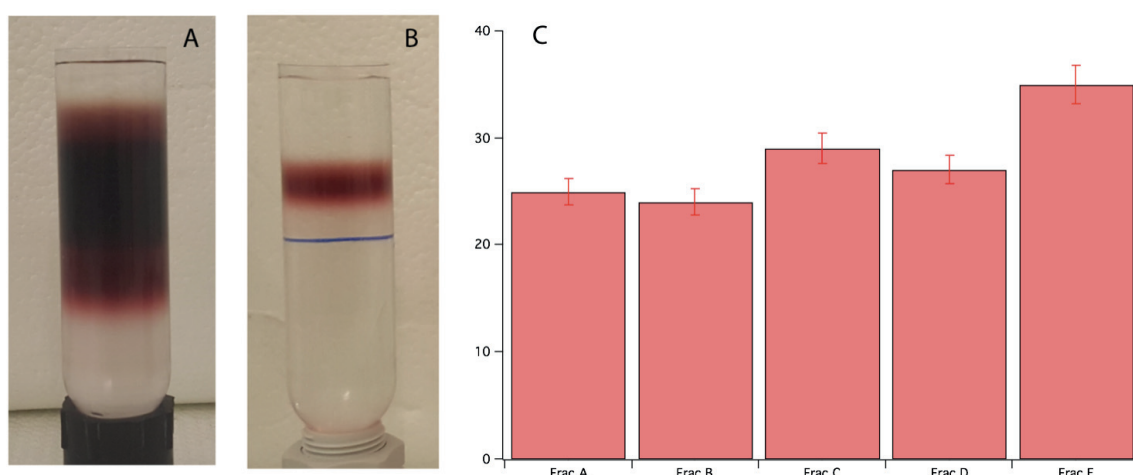
Figure 4.5: Sucrose gradient fractionation photographs after a) first and b) fourth step of the same MUSOT NPs batch. Note that the size separation of NPs was successful but the amount of material also decreases as characterized by the intensity of the color, c) OT ligand percentages calculated with NMR analysis as described below. The OT ligands are apparently

not the same for all fractions which complicate the separation as it affects the colloidal stability as well as density.

CHAPTER 5

5. AUC: A NEW TOOL FOR MEASURING NANOPARTICLE-PROTEIN
INTERACTIONS

Instrumental and methodological shortcomings of scattering and fluorescence-based techniques limit the resolution and reliability of thermodynamic analysis of protein-NP interactions. As discussed previously, AUC prevails over other colloidal characterization techniques in many aspects, thus can be regarded as valuable alternative for characterization of such interactions. In this chapter, AUC based, a novel characterization methodology will be put forward. Detailed description of the incorporation of Hill formulation for generic ligand-receptor interactions to sedimentation analysis in AUC will be presented. Additional information such as anisotropic shape evolution of NP-protein complexes will be discussed. The results presented in this chapter were published in *Bekdemir, A. and Stellacci, F. Nature Communications., 2016, p 13121.*

5.1. State-of-the-art

Recent work by Parak and coworkers applied fluorescence correlation spectroscopy to determine binding affinity and stoichiometry based on change in the correlation function of fluorescent NPs which was adapted to Hill formulation [134]. The method basically uses the correlation function to calculate average hydrodynamic diameter increase upon protein attachment. Then, they elegantly combined Hill formulation
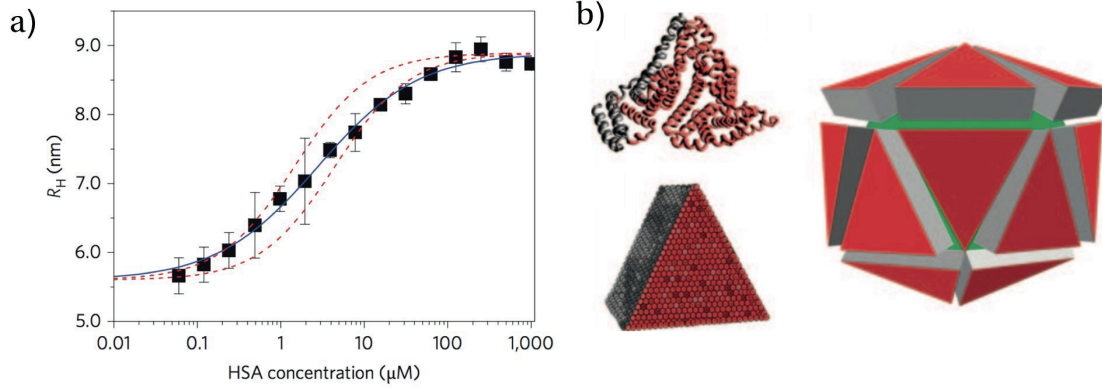
Figure 5.1: a) Hydrodynamic size evolution of FePt nanoparticles as human serum albumin (HSA) is added to the solution due to protein coverage. Black boxes are experimental data points calculated with fluorescence correlation spectroscopy. The blue solid line represents a fit of an anti-cooperative binding model (Eq. 5.1) to the data, and the red dashed lines are Langmuir binding isotherms fitted to the first and last 20% of the transition. b) HSA is a triangular pyramid like protein which was approximately 8 nm in edges and 3nm in depth. Using these parameters, fully packed HSA can cover up to 24 proteins on the surface of around 10 nm nanoparticles. Ref. [134] with the permission of The Nature Publishing Group.

with hydrodynamic size information for a series of NP-protein complexes. This description was subsequently converted into kinetics and thermodynamics interaction parameters for CdSe/ZnS quantum dots and FePt NPs. Simply, any additional protein attached to a NP surface would result in a gradual increase in the overall hydrodynamic size of NP-protein complexes. The size (r_H) can be expressed as a function of the number of protein bound to the surface (N) with a given initial size of NPs ($r_H(0)$) and the scaling factor (c):

$$r_H(N) = r_H(0)\sqrt[3]{(1 + cN)} \qquad (5.1)$$

This approach allowed to collectively represent the effect of increase in size with respect to number of proteins attached to NPs' surface. This representation inspired the basis of my work where I take another hydrodynamic parameter (sedimentation coefficient, *s*) and formulated its evolution as more proteins attach to NPs' surface by exploiting a more robust instrumental approach (AUC).

5.2. Exploiting AUC for Characterization NP – Protein Interactions

5.2.1. Theoretical Foundations of the New AUC Model

In a conventional SV experiment in AUC, a particle in a solution is subjected to three different forces that come into equilibrium and reach terminal velocity in a very short period of time. Centrifugal force is directed towards the bottom of the cell and depends on the rotor acceleration ($\omega^2 r$) while buoyant force and frictional force act in opposite direction. These forces are summed up in Svedberg equation and combined with Stokes-Einstein relation, eventually providing the Stokes-equivalent spherical diameters [135]:

$$r_H = \frac{1}{2}\sqrt{\frac{18\eta_s s}{(\rho_p - \rho_s)}} \qquad (5.2)$$

where r_H is hydrodynamic radius of an analyte, η_s is solvent viscosity, *s* is sedimentation coefficient, ρ_p and ρ_s are densities of the analyte and solvent respectively. The density of a NP-protein complex varies depending of the fraction of each component. Assuming the formation of homogeneous complexes at equilibrium, which depends only on the proteins concentration, we can express the

density of the NP-protein complex as shown in equation 5.3. The density and volume information of both the isolated NPs and proteins are derived from individual SV experiments.

$$\rho_{cx} = \frac{\rho_{Np}V_{Np} + N_{avg}\rho_P V_P}{V_{Np} + N_{avg}V_P} \qquad (5.3)$$

where N_{avg} is the average number of protein per NP, V_{Np} and V_P are volumes of NP and protein, respectively and $\rho_{cx}, \rho_{Np}, \rho_P$ are densities of NP-protein complex, NP and protein alone, respectively. When equations are combined, the average sedimentation coefficient of NP-protein complex can be expressed in terms of N:

$$s_{cx}(N_{avg}) = \frac{2}{9\eta}\sqrt[3]{\frac{9}{16\pi}}\frac{(\rho_{Np} - \rho_s)V_{Np} + N_{avg}(\rho_P - \rho_s)V_P}{(V_{Np} + N_{avg}V_P)^{1/3}} \qquad (5.4)$$

N_{avg} can be expressed as a function of protein concentration according to the following equation:

$$N_{avg} = N_{max}\frac{1}{1 + \left(K_D/_{[P]}\right)^n} \qquad (5.5)$$

where N_{max} is maximum number of protein per particle, K_D is dissociation constant of interaction and n is the Hill coefficient. Therefore, using equation (5.5) into (5.4) provides the whole model that is to be used for fitting the experimental data obtained from SV-AUC experiments for AuNPs together with BSA as a model protein:

$$s_{cx}([BSA]) = \frac{2}{9\eta} \sqrt[3]{\frac{9}{16\pi}} \frac{(\rho_{Np} - \rho_S)V_{Np} + N_{max}\frac{1}{1+\left(K_D/[BSA]\right)^n}(\rho_P - \rho_S)V_P}{\left(V_{Np} + N_{max}\frac{1}{1+\left(K_D/[BSA]\right)^n}V_P\right)^{1/3}} \quad (5.6)$$

Equation 5.6 is floating the parameters K_D, N_{max} and n while all the other parameters ρ_{NP}, V_{NP}, ρ_P and V_P are obtained from separate SV-AUC experiments and kept constant during the fitting. This function has two important characteristics: (1) the initial steep region where the affinity and cooperativity of the binding are related, and (2) the plateau portion from which a protein monolayer is quantified. The resulting adsorption isotherm apparently employs Hill equation and therefore, necessitates the reversibility of the binding for correct interpretation of the interaction parameters. Within the given equilibration time for the initial nanoparticle – protein mixture, any modifications on the reaction (e.g. temperature, pH, concentrations of the reagents) should entail new equilibrium state. As to whether this could be observed in our experiments will be discussed later in this chapter.

Three types of gold NPs are used as model NPs in this work: (i) citrate coated (citrate-AuNPs), (ii) 11-mercaptoundecanoic acid coated (MUA-AuNPs) and (iii) 11-mercaptoundecane sulfonate coated (MUS-AuNPs). For details of synthetic protocols, refer to chapter 4.

Table 5.1: Summary of NP properties used in this work. Core diameters (d_{core}) are calculated from TEM analysis and hydrodynamic diameters (d_H) are calculated using sedimentation coefficients obtained from AUC experiments. PDI refers to polydispersity index, simply standard deviation of d_{core} values divided by the averaged d_{core} values. Ligand lengths are approximately calculated with ACDLabs 3D chemical drawing software with fully extended conformation of the ligands. PDI is estimated via the standard deviation of the Stokes radius distribution from c(s) distribution in SEDFIT software.

	d_{core} (nm)	d_H (nm)	PDI (%)	Ligand type	Ligand length (nm)
Citrate-AuNPs	12.6	13.6	12	Citrate	0.5
MUA-AuNPs	6.1	9.4	10	-COOH	1.7
MUS(m)-AuNPs	4.4	7.0	11	$-SO_2OH$	1.8
MUS(s)-AuNPs	2.2	5.6	16	$-SO_2OH$	1.8

5.2.2. Determination of Interaction Parameters

First, we started with MUA-AuNPs as these particles are neither large nor small and suitable candidates for comparison with previously reported values. NPs solutions (at a constant concentration) were incubated with several concentrations of BSA and SV experiment were conducted for each mixture. All mixtures' *c(s,D)* distributions were calculated in SEDFIT and plotted together to construct the absorption isotherm as shown in Figure 5.2. The experimental data was fitted to the equation and the interaction parameters for MUA–AuNPs with BSA were estimated (Figure 5.3). The
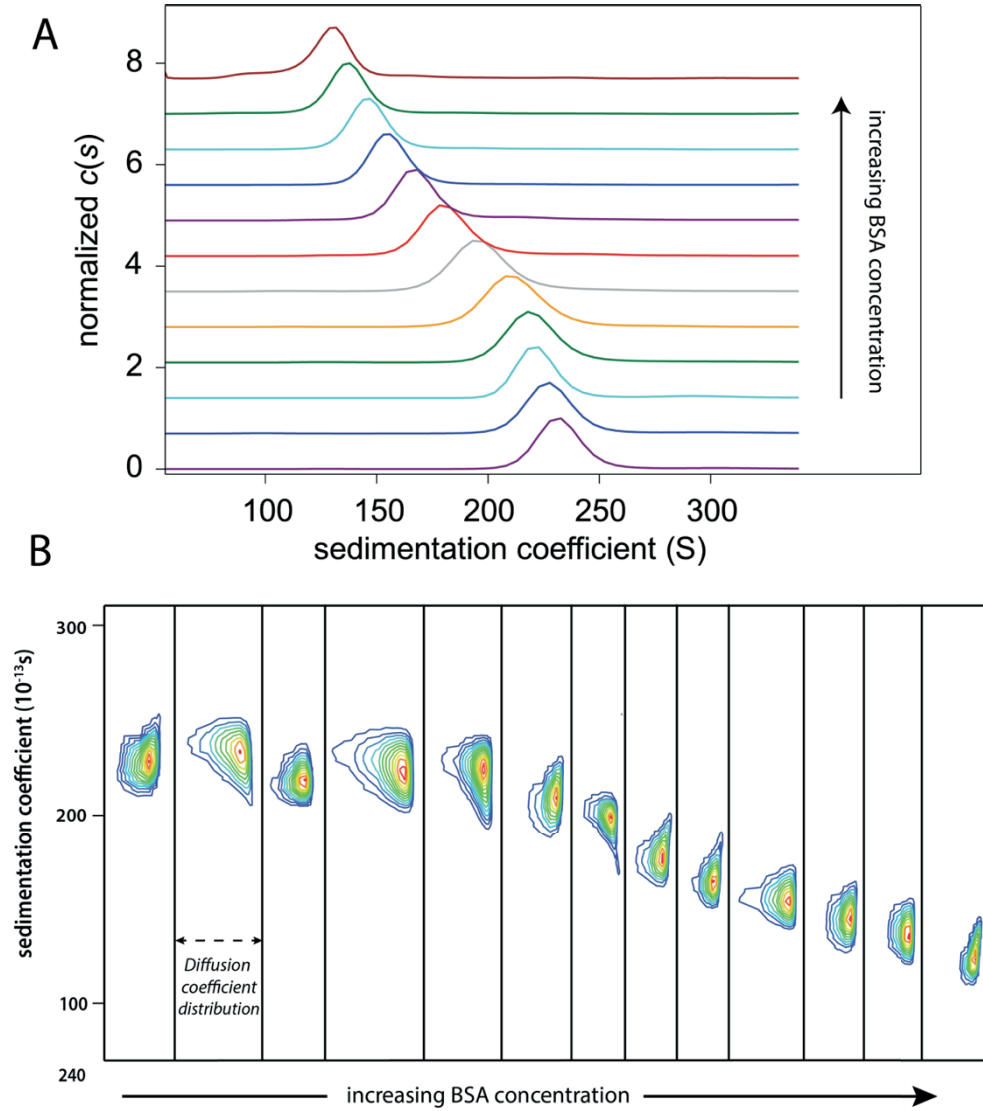
Figure 5.2: a) overlaid sedimentation coefficient distributions of MUA nanoparticles with respect to bovine serum albumin (BSA) addition. Note that the average s-values are decreasing consistently. b) sedimentation – diffusion coefficients distribution of the same experiment demonstrates the appearance of Langmuir type of isotherm as more BSA is added to the solution.

71

B	d_{Hyd} (nm)	K_D (10^{-6} M)	N_{max}	n (cooperativity)
AUC (MUA-AuNPs)	9.4	5.4 ± 0.9	18 ± 2	0.8 ± 0.1
FCS (FePt NPs)	11.2	5.1 ± 1.3	22 ± 4	0.7 ± 0.1
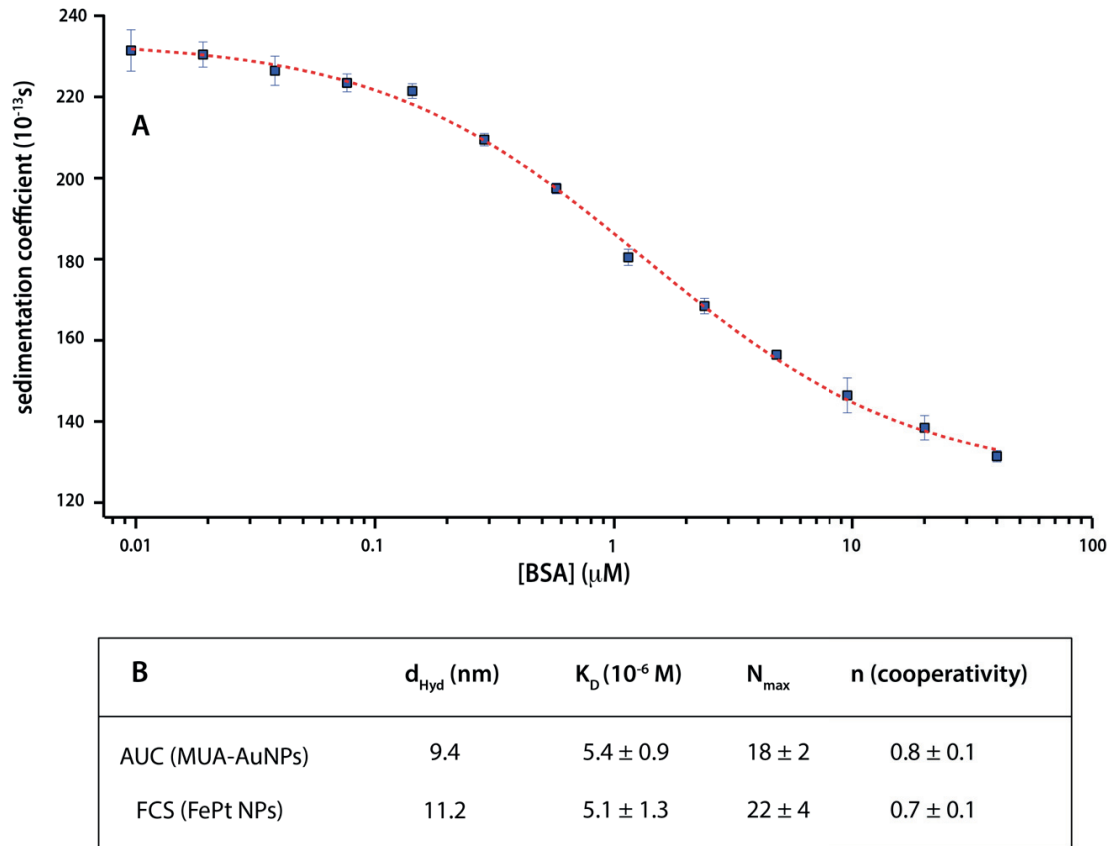
Figure 5.3: a) the average s-values of MUA NPs with respect to BSA concentration. The blue boxes are experimental data points with three independent measurements. Red dashed line is the fit line according to the Equation 5.6. b) Table of interaction parameters of obtained in this fit for MUA NPs and BSA compared with the parameters for FePt NPs-HSA interaction characterized with fluorescence correlation spectroscopy. Note that the similar size of nanoparticles results similar interaction parameters which confirms the reliability of method.

results obtained are matched well with previously reported values for Human Serum Albumin (HSA)–FePt NPs interactions with similar hydrodynamic diameter and functional groups of NPs [134]. Nanoparticles with similar hydrodynamic diameter

(9.4 nm for MUA-AuNPs and 11.2 nm for FePt NPs) with similar ligand type (carboxylic acid terminated) lead to comparable protein adsorption behavior in terms of K_D and n. The subtle difference in N_{max} values might be due to the variation in size as lower N_{max} value corresponds to smaller AuNPs. However, the possibility of different ligand packing density of NPs for different metals should also be taken into account to reach the final conclusion.

The second type of NPs we used was the 14nm citrate coated AuNPs (Figure 5.4a). The dissociation constant, K_D calculated with AUC method for citrate-AuNPs and BSA interaction is found to be 13.6±3.5 10^{-6} M. This value is close to the previously reported value (association constant, K_A = 0.01±1.5) obtained using quartz crystal microbalance (QCM) [79].

In order to work with NPs with different surface functional groups, we investigated MUS(m)-AuNPs [slightly smaller than MUA-AuNPs] (d_H = 7.6 nm). Residuals plot show that excellent fitting quality with feasible interaction parameters are achieved regardless of the surface functionality (Figure 5.4b). Although this work is centralized around BSA as a model protein of choice, other proteins could also be investigated once their density and hydrodynamic volume are known. In this respect, various human serum albumin solutions are moreover incubated with this particular NP type and results are reported in Table 5.2).

AUC also allows to investigate very small colloidal particles. To prove this point, we synthesized and fractionated MUS(s)-AuNPs with 2.2 nm core diameter. The $c(s)$ analysis of MUS(s)-AuNPs and BSA mixtures is modeled through the fit function with excellent fit quality and interaction parameters were obtained (Table 5.2). To the best
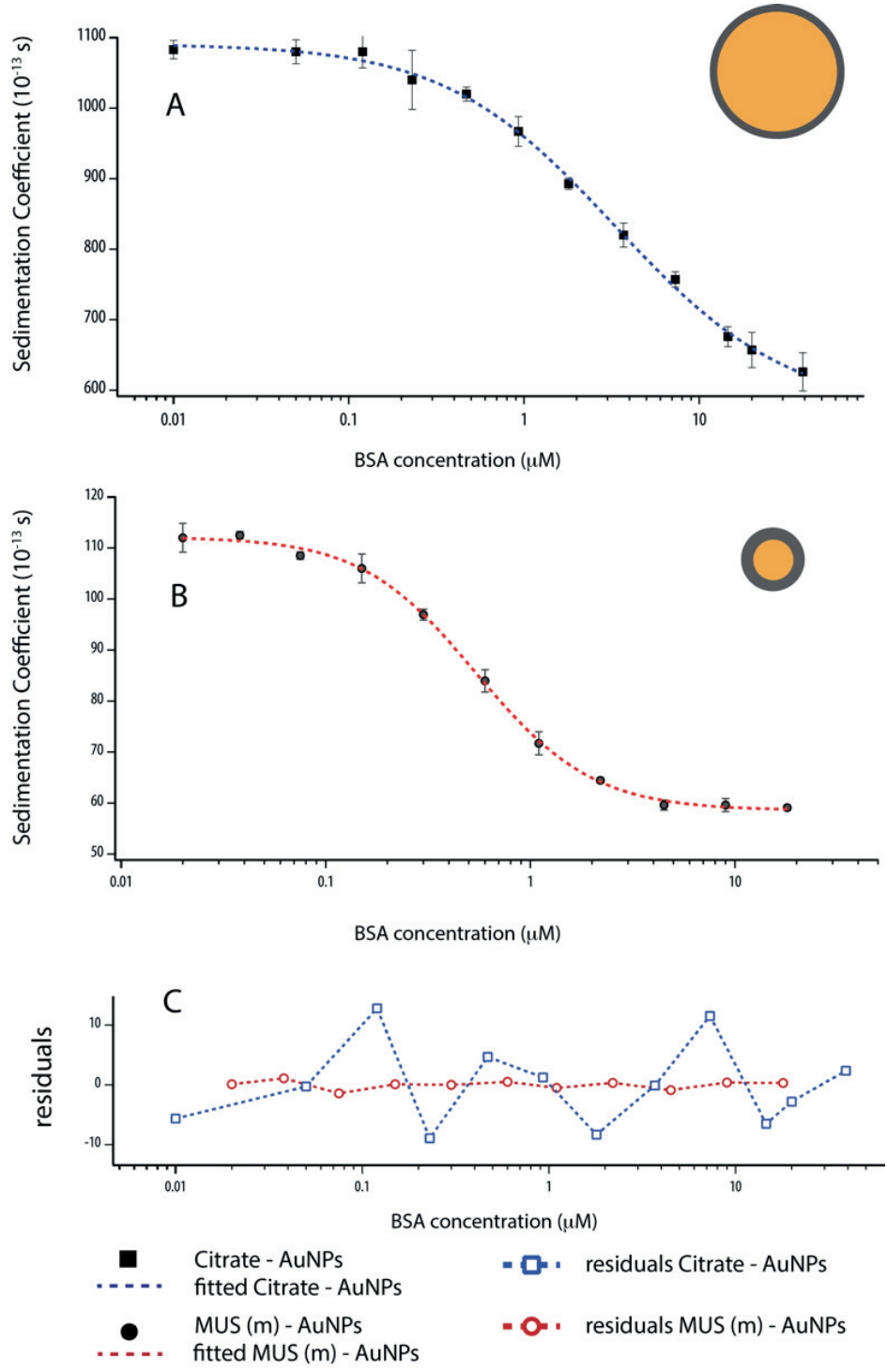
Figure 5.4: SV-AUC binding isotherms for Citrate-AuNPs and MUS(m)-AuNPs with BSA. Plots of average s versus BSA concentration for a) citrate– AuNPs (d_H = 13.6 nm) and b) MUS(m)–AuNPs (d_H = 7.6 nm). Dashed lines are fits obtained using equation (6). c) Residuals of the fit functions are plotted against BSA concentration. Dashed magenta line indicates the nanoparticle concentration kept constant during experiments. Error bars represent the standard deviation of three independent measurements from the same batch of NPs.

of our knowledge, investigation of the thermodynamic parameters of interaction with proteins for such small particles is presented here for the first time.

The limitation on investigating small sized NPs with AUC depends on the sedimentation coefficient. Proteins under investigation should have sufficiently distinct *s* from the *s* of NPs, otherwise the changes in sedimentation coefficient as a function of protein concentration would be too small. For most cases, this does not pose any problem because most proteins have low *s* compared to metal NPs due to their low densities (1.2-1.3 g/cm^3).

Table 5.2: Interaction parameters obtained from AUC for various types of AuNPs and proteins.

	s_{avg} (Sved.)	D (x10^{-11}m^2/s)	K_D (10^{-6} M)	N_{max}	n (Hill Coeff.)
Citrate-AuNPs - BSA	1080	3.38	13.6±3.5	36±5	0.9±0.1
MUA-AuNPs - BSA	234	4.13	5.4±0.9	18±2	0.8±0.1
MUS(m)-AuNPs - BSA	119	5.78	1.1±0.1	10±1	1.3±0.1
MUS(m)-AuNPs - HSA	119	5.78	0.57±0.1	5±1	1.6±0.3
MUS(s)-AuNPs - BSA	22	6.16	9.2±0.9	2±0	1.6±0.2

5.2.3. Shape Evolution of NP-Protein Complexes

Once obtained, the interaction parameters can be placed in the equation 5.5 and used to determine the average number of protein (N_{avg}) per nanoparticles as a function of concentration of protein ([BSA]). The back calculation of the equation 5.3 allows to calculate the parameter N_{avg} for each defined experimental [BSA] points.

As stated before, SV-AUC not only measures sedimentation coefficient of a species but also diffusion coefficients. According to the hydrodynamic scaling law,[81] D is a function of s and frictional ratio (f/f_0). Frictional ratio is a dimensionless ratio of translational frictional coefficient of a species to that of an equivalent spherical substance of the same volume. In this regard, the higher the f/f_0, the more the substance is non-spherical. Using scaling law, f/f_0 can be written as a function of D and s with a given density of a species (Equation 5.7):

$$\frac{f}{f_0}(s, D) = \left(\frac{\sqrt{2}}{18\pi}\right)^{2/3} \left(\frac{k_b T}{D}\right)^{2/3} \frac{s^{-1/3}}{\eta_s}(\rho_{cx} - \rho_s)^{1/3} \qquad (5.7)$$

Recent studies determined the hydrodynamic shape of BSA as a triangular prism of equilateral triangle of 8.4 nm edges together with a thickness of 3.2 nm[66,87]. Considering the side-on attachment of BSA on AuNPs consisted with the maximum interaction geometry,[148] for big particles such as citrate-AuNPs (d_{core} = 13 nm), the shape would mostly preserve spherical geometry upon binding of BSA because of the small change in overall diameter. Accordingly, by estimating f/f_0 for each protein addition on citrate-AuNPs, it is possible to see slight fluctuations over the spherical value of 1.2 but no systematic trend (Figure 5.6a). On the other hand, when f/f_0 values
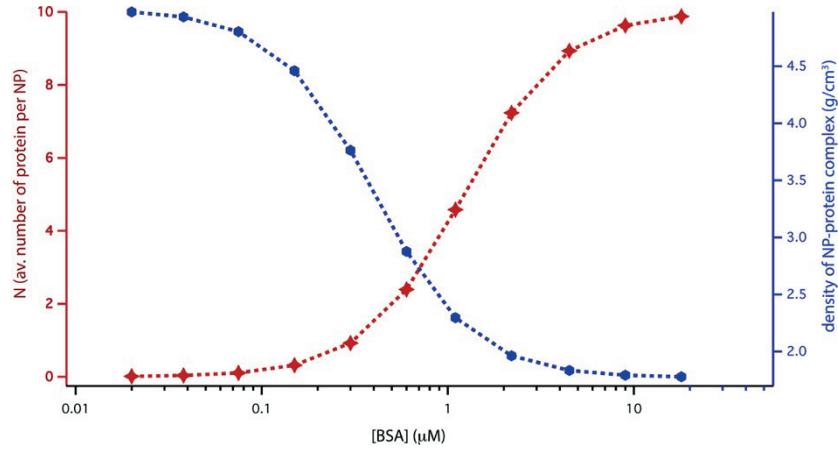
Figure 5.5: Average number of protein per nanoparticle calculated from Equation 5.5 after fitting and obtaining interaction parameters (Red dots are protein titration points; dashed line is the function itself. The density of nanoparticle-protein complex at each titration points then can be calculated with Equation 5.3 by using density of protein, nanoparticle and approximate volume of protein (blue markers are the same titration points; the blue dashed line is the function of equation 5.3).

are estimated for medium sized-NPs/BSA complexes (namely MUA-AuNPs), there is a gradual increase upon the first additions of BSA up to a value of f/f_0 of ~1.6, followed by a stepwise decrease reaching a plateau value around 1.2. It is interesting to note that the peak value arises when the N_{avg} is around 2 proteins (Figure 5.6b). This suggests that after the first BSA molecule attached to the NP, the second one approaches possibly from the other side of the complex due to the steric reasons and create an elongated structure. When further BSA molecules are introduced, regardless of the binding position, they are gradually constructing the globular shape back again until NPs are fully covered in which case f/f_0 is again 1.2.

In case of very small MUS(s)-AuNPs, the interaction parameters indicate N_{max} to be around 2 BSA molecules per particle at saturation (Figure 5.6c). The analysis of f/f_0 revealed that there is an increasing f/f_0 starting right after the first additions of BSA and continuously elevate until the end of the saturation. Again, the mechanism can be speculated in the same way MUA-AuNPs' case with stronger effects on the frictional ratio as the size of the particles is more comparable to the size of the proteins (and the saturation is already at ~2 proteins per particles). Overall, frictional ratio analysis of particularly small particles – protein conjugates suggests that the complex's shape can considerably deviate from original sphere. This analysis cannot be considered analytically rigorous as some of the thermodynamic association parameters are first derived based on the assumption of f/f_0 to be ~1 and then used to find deviation of f/f_0 from 1. Yet we believe that the overall indication is correct (and strongly backed up by sound geometrical arguments. A more rigorous approach could be developed with multiwavelength AUC. In this case, future studies with multiwavelength AUC can improve the understanding of the NP-protein system by adding wavelength dimension to the analysis. Monitoring protein and NP concentration separately should allow to obtain more information on the NP-protein interactions[84]. For example, the density of NP-protein complex is solely theoretical approximation based on individual NP and protein densities which decreases the accuracy of f/f_0 analysis. Instead, recent advancements on multi-wavelength AUC could provide much more reliable information on the axial ratio of NP-Protein complexes through multidimensional analysis. This could also allow us to analyze protein interaction with other types of nanomaterials such as gold nanorods and carbon nanotubes. Finally, the applicability of the method could be widened through the employment of other optical sources in AUC, such as an interferometer. Characterizing the species inside the solution by fringes stem from refractive index
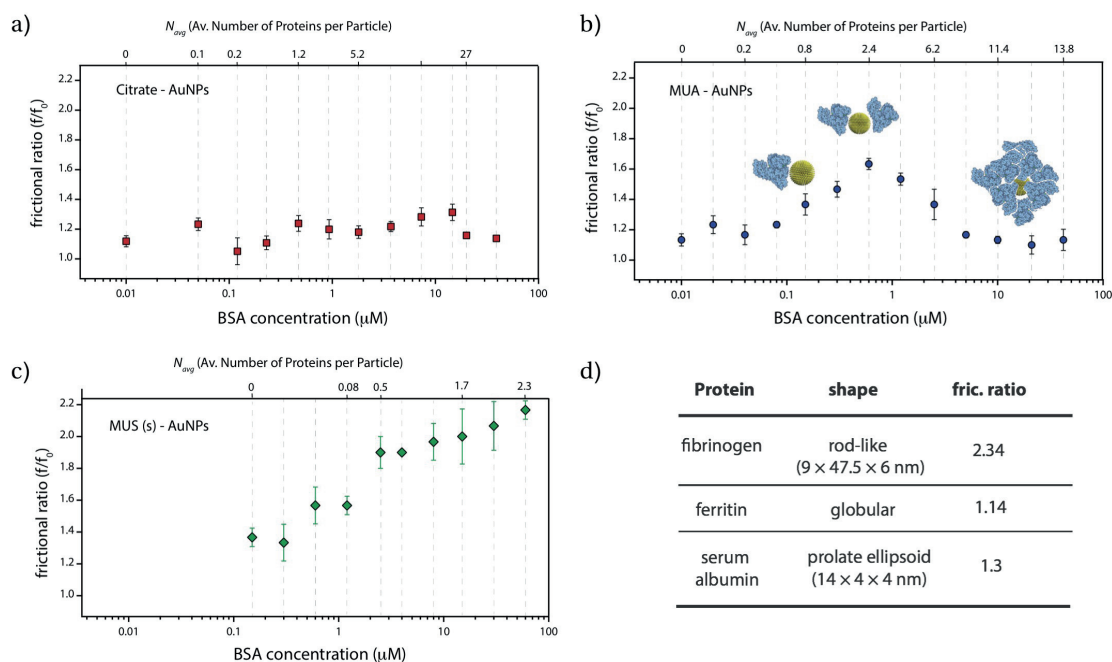
Figure 5.6: Anisotropic shape evolution of NP-protein complexes. Plots of frictional ratio versus BSA concentration (bottom x-axis) and Navg (top x- axis) for a) Citrate–AuNPs, b) MUA–AuNPs and c) MUS(s)–AuNPs. Possible arrangements of proteins on a nanoparticle are depicted in the plots to clarify the anistropic change on protein binding. It should be noted that these are only cartoon images and not based on scientific simulation. Error bars represent the standard deviation of three independent measurements from the same batch of NPs. d) frictional ratio values of some common proteins to show the relation between the anisotropy and frictional ratio.

change offers a convenient workaround for non-absorbing soft materials like polymers and dendrimers.
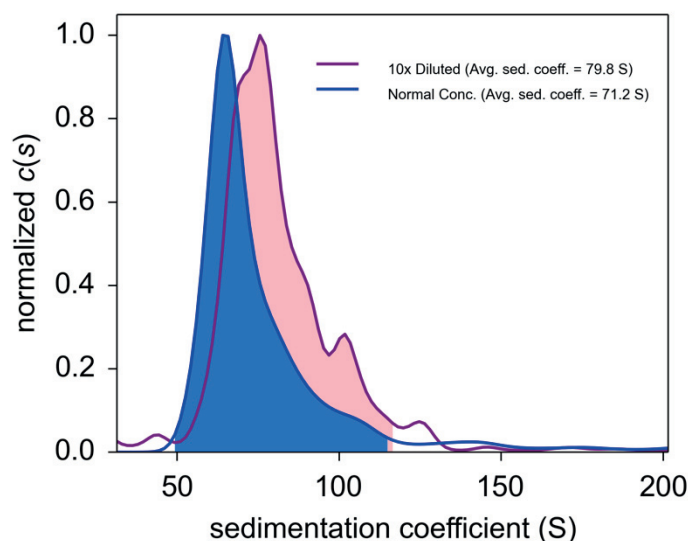
Figure 5.7: Reversibility of protein interactions shown in AUC: mixing ~1 nM of MUS(m)-AuNPs with 1 µM BSA and incubation for 16 hours at 20 °C before running in AUC. For that particular molar ratio, NP – protein complex formed a solute with average sedimentation coefficient of 71 S. Then, diluted the mixture 10 times by volume and incubated with an additional 16 hours. AUC experiment afterwards revealed a shift towards higher s values that indicates some degree of desorption of BSA from MUS(m)-AuNPs' surface.

5.2.4. Reversibility of NP – BSA Interaction

Protein adsorption to NPs can manifest in different ways which comprises a distinction between a hard corona and soft corona. The interaction strength can become extremely high so that practically the adsorption is called irreversible rather than being in equilibrium. This is particularly valid for some hydrophobic NPs that foster a conformational change and denaturation of a protein after adsorption to NPs' surface. Even though the initial protein adsorption is merely driven by small amount of Van der Waals interactions and London dispersion forces, denaturation of

the protein exposes originally buried hydrophobic amino acids and multiply the interactions with NPs resulting in an irreversibly strong binding. In this approach, the validity of Hill formulation and Langmuir type adsorption strictly depends upon the reversibility of any protein – NP interaction and therefore should be confirmed with additional experiments. To this end, sedimentation analysis of a protein-NP mixture before and after dilution was compared (Figure 5.7). The apparent shift towards larger *s*-values upon diluton confirmed the reversible nature of protein binding, thus verified the validity of AUC approach for investigation of protein-NP interactions through Hill formulation.

5.3. Conclusion

In conclusion, AUC can be used as a tool to determine accurately and reliably thermodynamic interaction parameters of proteins with monodisperse NPs. With the method developed here, it is possible to determine dissociation constants (K_D), maximum protein number per nanoparticle (N_{max}), and Hill coefficient, *n* for the association of monodisperse NP-protein complexes regardless of their size. The strength of the methods is in its label-free absorption nature that allows for the study of large or small particles with no increase in complexity and with close to no-influence from possible protein aggregates in the medium.

CHAPTER 6

6. COMPARATIVE NANOPARTICLE - PROTEIN BINDING STUDIES WITH
^{1}H-^{15}N HSQC NMR SPECTROSCOPY AND ANALYTICAL ULTRACENTRIFUGATION

The complexity of protein binding to NPs entails investigation of different aspects to describe a single binding event in full course. We have already shown that AUC can be employed to calculate thermodynamic binding parameters with high resolution. This chapter outlines NMR based methodology to complement protein binding studies with mechanism information. Molecular level binding scheme was presented for NPs with different size, surface chemistry and hydrophobicity. The resulting discrepancies based on these parameters were correlated to hydrodynamic properties of NPs characterized by complementary AUC analysis. Combination of AUC and NMR analysis revealed that protein binding to NPs could be highly sophisticated phenomenon that depends on multiple features of NPs.

6.1. Protein-Nanoparticle Interactions with Solution NMR Spectroscopy

Solution NMR spectroscopy is well-studied as robust and versatile method for characterization of biomolecules. A plethora of information on biomolecules' local and global structure as well as their solution dynamics can be obtained with combination of various types of solution NMR techniques. Molecular level resolution obtained in most NMR experiments do not only allow for a simple characterization of biomolecules but also shed light on details of intermolecular interactions. Ligand
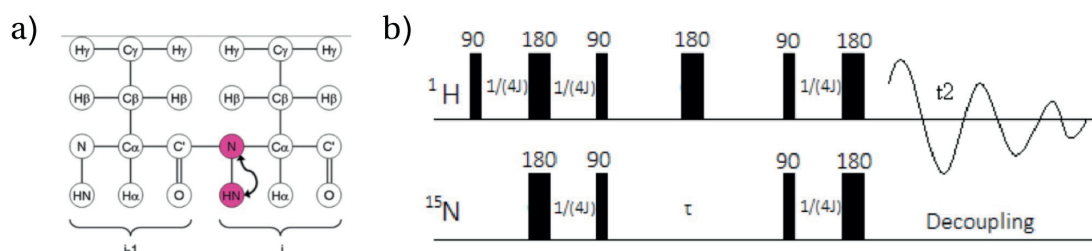
Figure 6.1: a) representation of atoms used in heteronuclear single quantum coherence spectroscopy (HSQC) NMR. Only nitrogen atoms that are directly attached to protons are excited and the relaxation excites back the same proton in a different mode which can be decoupled with the pulse sequence presented in b).

perturbations that form interaction epitopes on a protein can be mapped to 3D crystal structure of the protein with extremely high precision and accuracy.

Conformational stability, steady-state kinetics, translational and diffusion coefficients can also be obtained from a variety of NMR techniques. Although practical limitations such as the necessity of isotopically labelled proteins hamper the wide range use of protein NMR in nanoparticle field, there are few studies of NP-protein interactions using specific methods in solution NMR spectroscopy. Heteronuclear single/multiple quantum coherence spectroscopy (HSQC/HMQC) reportedly constitutes the majority of these works and will also be used in our studies.

6.2. Basics of Heteronuclear Single Quantum Coherence (HSQC) NMR

HSQC NMR was first described by Bodenhausen and Ruben at 1980 as an experiment where magnetization on the proton is transferred to a secondary nucleus (generally

^{15}N or ^{13}C) *via* insensitive nuclei enhanced by polarization transfer (INEPT) protocol. The relaxation signal is then formed after the secondary magnetization reverses to the primary proton after a time delay (t_1). Therefore, the direct dimension is always ^{1}H signal while the chemical shift for secondary nuclei constitutes the indirect dimension. The cross peaks of direct and indirect dimensions form pseudo-3-dimensional with the third dimension being the signal intensity for each peaks (I). Among solution NMR spectroscopy methods for proteins, HSQC NMR stands out as an important biomolecular fingerprinting technique as it is extremely useful to identify the cross peaks of multiple nuclei in a protein system and therefore filter out the noisy homonuclear signals. Even though historically the size limitation was a huge problem in HSQC NMR (only 50-70 kDa), advances on isotopic labelling and methyl-specific labelling as well as the combination with transverse-relaxation optimized spectroscopy (TROSY) allowed to investigate as large as 1 MDa proteins with HSQC NMR methods [136].

6.3. Protein – Nanoparticle Interactions with HSQC NMR

Three main characteristics that can be obtained with a good degree of precision for a conventional HSQC NMR spectrum are chemical shift, intensity and linewidth of a signal. The chemical shift (or resonance frequency) simply depends upon the local chemical environment that a given nucleus is surrounded by, while intensity is directly related to the number of nuclei that have the same frequency. Rotational correlation times of a protein is proportional to the transverse spin relaxation rate in NMR which affects the linewidth of a signal. One of the most prominent effect of NPs attachment for a protein NMR is the broadening of linewidths due to increased rotational correlation times (or reduced tumbling rates). Usually, most NP-protein
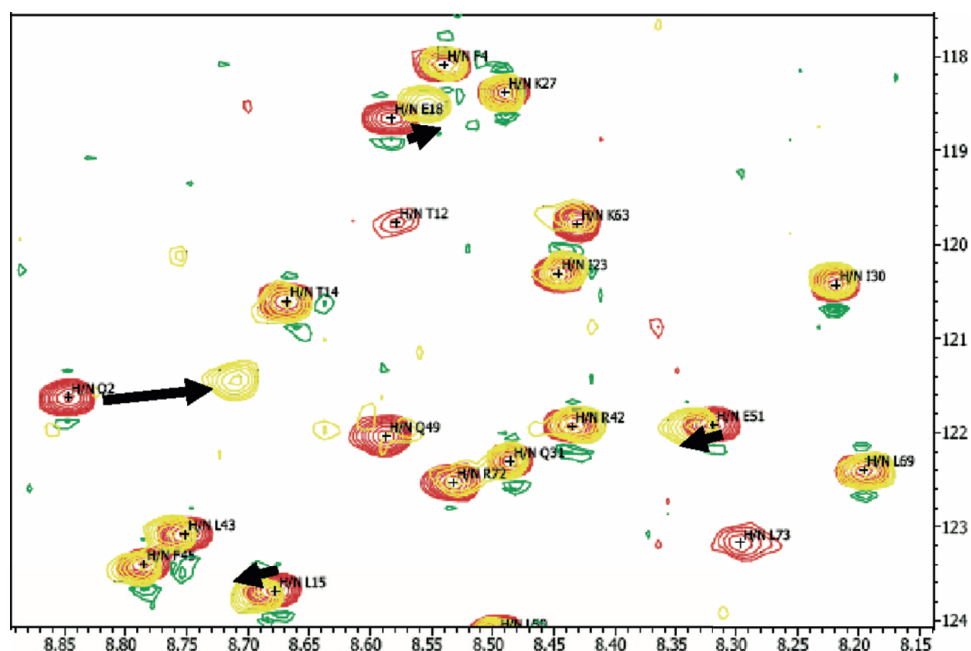
Figure 6.2: ^{1}H-^{15}N HSQC NMR study of ubiquitin with 13nm citrate gold nanoparticles. Note the particular amino acid cross peaks dramatically shifted, identifying the binding sites. Ref. [137] with the permission of The American Chemical Society.

complexes have significantly higher molecular weight and density than the protein alone and results in low tumbling rates, therefore, most of the times the signals become extremely broad and invisible.

In general, the difference in protein NMR spectrum upon NP interaction can manifest in number of ways, for instance, chemical shift perturbation (CSP), broadening of linewidth and/or decrease in signal intensities. Calzolai *et.al.* for instance monitored CSP of ^{15}N-labelled human ubiquitin upon adsorption to 12 nm citrate gold NPs in ^{1}H-^{15}N HSQC NMR spectroscopy [138]. They observed a

considerable shift in peaks corresponding to Q2, L15 and E18 amino acid residues which were attributed to primary contact points for ubiquitin – citrate AuNPs interactions. It was reported that the protein attachment was initially driven by electrostatic interactions although in later stages citrate ligands might have been displaced by the whole protein.

Another study by Srinivasan *et.al.* displays chemical shift perturbation for ^{15}N-labelled wild-type ubiquitin when mixed with AuNPs with self-assembled monolayers of mimicry of multimodal chromatographic "Capto" and "Nuvia" resin materials [139]. Their common interaction residues are found to be K48, H68, L69, V70 and L71 being completely different from Calzolai's study possibly due to drastic difference in NPs' ligands used in both studies. A more recent study discusses ubiquitin interaction with citrate capped silver NPs through CSP. However, in this study, they also report broadening in individual peaks where transient interactions might occur particularly for positively charged AA residues. Additionally, selective radio frequency pulse sequence allowed specific relaxation experiments which revealed local conformational fluctuations on binding sites upon interaction with silver NPs[140]. The more emphasis on the broadening effect on linewidths for signals upon NP insertion was observed in heteronuclear multiple quantum coherence (HMQC) – SOFAST spectroscopy when ubiquitin is mixed with graphene oxide (GO) sheets. In fact, Mondal *et. al.* calculated the T_2 relaxation rate for each AA residues after introducing GO sheets to the ubiquitin solution. The largest decrease in the T_2 relaxation rate, that is, the highest attenuation in signal intensity due to broadening effect was attributed to the contact points for ubiquitin on GO sheets. According to this protocol, the highest reduction was observed in I3, V5, L8, T12, L43, F45, A46, E51, D58, Q62, L69, V70 and G75 residues. The paper later discusses how
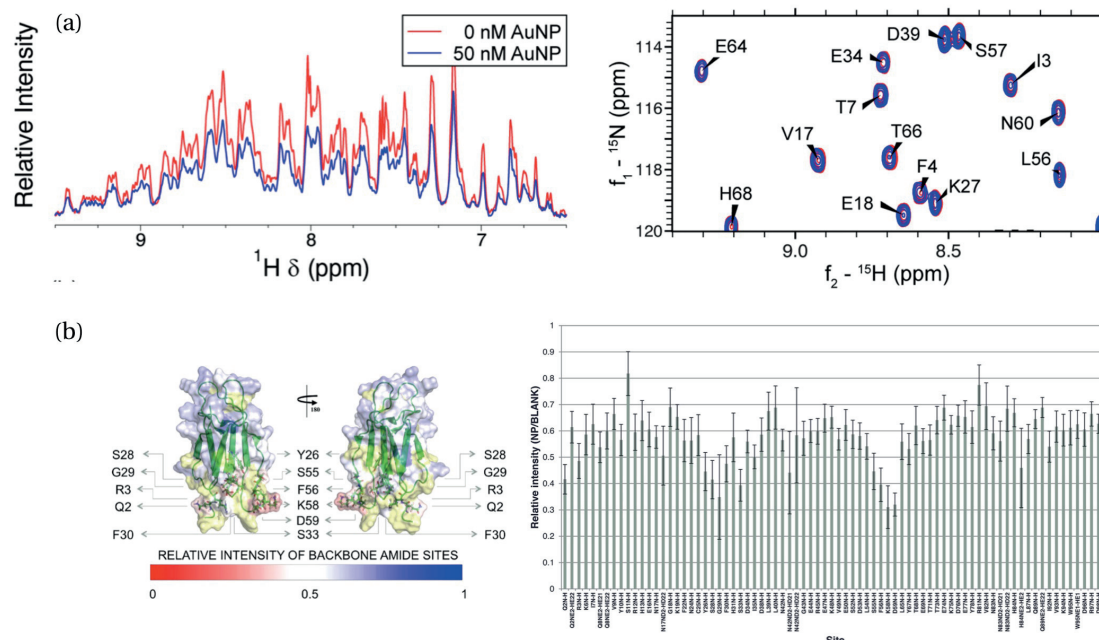
Figure 6.3: (a) Intensity decrease upon addition of 50 nM citrate capped gold NPs into ubiquitin solution. 2D spectrum on the right shows perfect overlap indicating no chemical shift is detected. Ref [141] with the permission of The American Chemical Society. (b) Investigation of b2-microglobulin – 5 nm gold NP interactions with intensity mapping in HSQC NMR experiments. Note the clear decrease in specific parts of protein is observable. Ref. [142] with the permission of The American Chemical Society.

different pH values in the buffer solution might deviate the interaction scheme for this protein – nanomaterial pair [143].

Depending on the kinetics of interaction between protein and NPs, intensity variations can also be evident instead of CSP in the HSQC spectra of protein-NP mixtures. For instance, Wang et. al. investigates interaction between 15 nm citrate capped gold NPs with ubiquitin that demonstrates only intensity decrease of amino

Figure 6.4: A summary of nanoparticles used in this work. 3D cartoon drawings are only for comparison (courtesy of Dr. Kellen Harkness).

acid cross peaks (Figure 6.3a). Interestingly, even though the NP - protein system is quite similar to the work of Calzolai, Wang and coworkers concluded that the disparity for the manifestation for the NP-protein interaction on both HSQC spectra
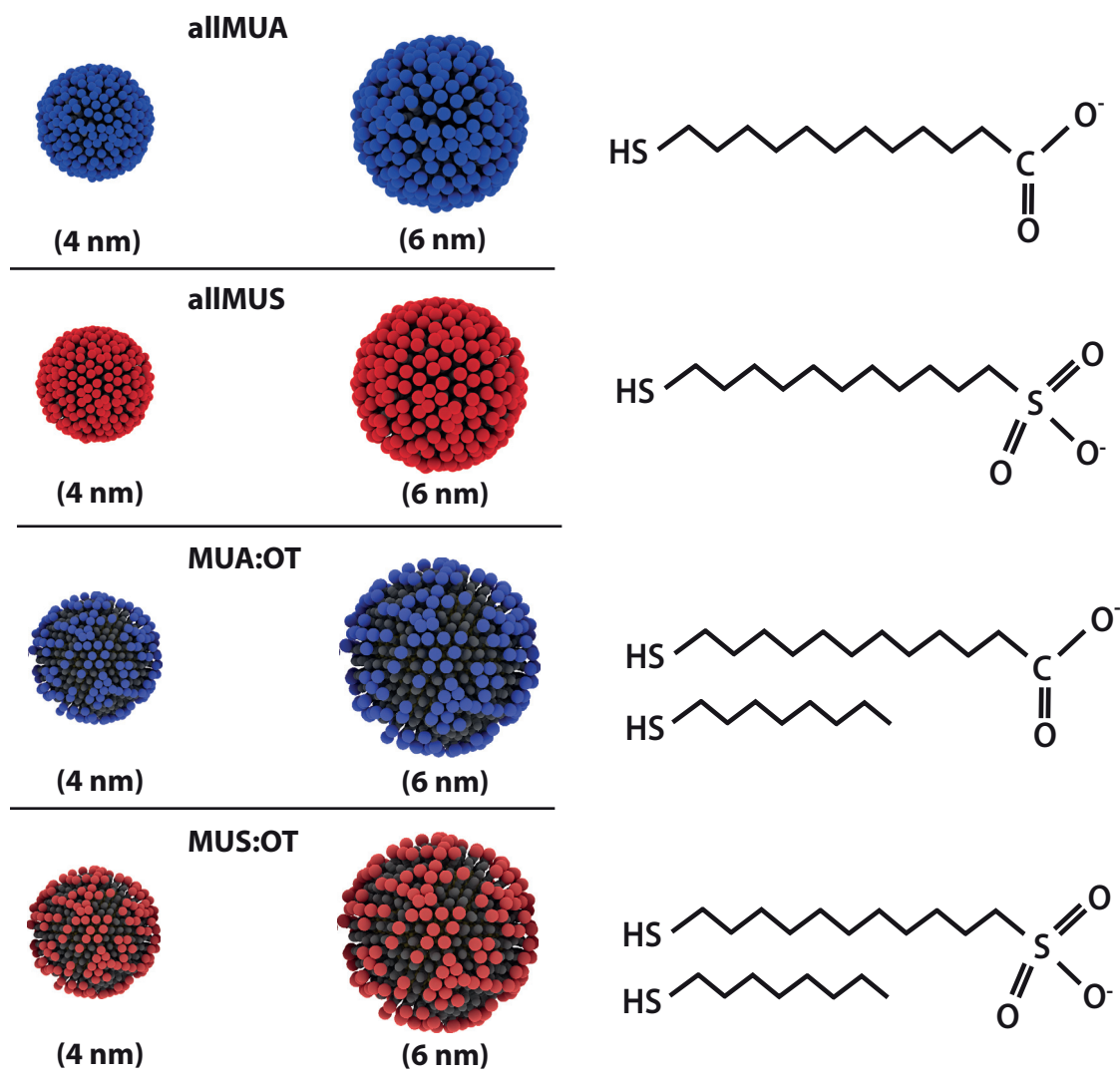
could be due to difference in the sample purity on protein solutions. They reported that Calzolai used commercially available ubiquitin samples which may have DNA contaminants and eventually affect the overall binding kinetics [141]. Additional example on intensity decrease upon NP binding is reported from Brancolini et. al. where fibrillogenic microglobulin and 5 nm gold NP adsorption was investigated [142]. Due to less ordered secondary structure of the protein, a clear characteristic decrease on certain amino acid cross peaks were observed which was attributed to primary binding site of proteins to these gold NPs (Figure 6.3b).

6.4. Design and Characterization of Nanoparticles

To carry out a reliable comparative study for protein binding behavior, it is crucial to set up high quality and well-characterized NP samples. To this end, we modified previously reported gold NP synthesis method by Stucky et. al. to produce highly monodisperse gold NPs with core diameters of 4 nm and 6 nm (see Chapter 4 for details of synthesis). In the first set, both 4 nm and 6 nm NPs were fully coated with one of the hydrophilic ligands, 11-mercaptoundecane sulfonate (MUS) or 11-mercaptoundecanoic acid (MUA) which provided substantial solubility in aqueous buffer conditions used in all experiments in this work (Figure 6.4). Zeta potential measurements in 10 mM phosphate buffer (pH 7.4) indicates substantially higher electrical potential for MUS NPs as compared to MUA NPs which was attributed to sulfonate terminal groups with higher degree of hydration. As per the surface coating of second set of gold NPs, a mixture of hydrophilic MUA (or MUS) and hydrophobic 1-octanethiol (OT) ligands was used in approximately 2:1 hydrophilic to hydrophobic molar ratio in order to increase the overall hydrophobicity of gold NPs (Table 1). The incorporation of secondary OT ligands with a given molar ratio did not considerably

Table 1. This table shows the OT percentage on the surface of each NPs calculated with NMR analysis described in chapter 4. Core diameters obtained by TEM show similar size distributions in each 4nm and 6nm set. Zeta-potential measurements indicate the negatively charged surface of NPs in the same buffer with NMR experiments (10mM phosphate buffer pH 7.4). Note the difference in electrical potential of NPs between sulfonate and carboxylate NPs.

	allMUA(4)	allMUA(6)	allMUS(4)	allMUS(6)	MUAOT(4)	MUAOT(6)	MUSOT(4)	MUSOT(6)
OT (%) NMR	0	0	0	0	32±3	32±3	31±3	33±3
Core Diam. TEM	4.2±0.7	6.5±0.9	4.0±0.6	6.2±0.8	4.0±0.7	6.2±1.5	4.1±0.7	6.3±1.0
ζ-potential 10 mM PB (pH 7.4)	-10±1	-12±2	-35±4	-34±5	-8±1	-11±2	-28±6	-30±3

affect the colloidal stability of gold NPs compared to their homoligand counterparts as demonstrated in zeta-potential measurements (Table 1). Overall, for the given conditions, all particles were found to be net negatively charged which is crucial to prevent charge driven aggregation with negatively charged ubiquitin.

6.5. ^{1}H-^{15}N HSQC NMR Analysis for Ubiquitin and Sub-10 nm Gold NPs

Ubiquitin is a robust molecule with high conformational stability at neutral pH even after long storage times. However, upon contact with a highly energetic surface like sub-10 nm NPs, it is crucial to confirm the absence of any variation in the secondary structure of ubiquitin in order to avoid any misinterpretation for the studies of NP-binding thermodynamics and mechanism herein. For this purpose, circular dichroism (CD) experiments were carried out to all NP – ubiquitin mixtures with similar molar ratios of NP to protein used in subsequent NMR experiments (Figure
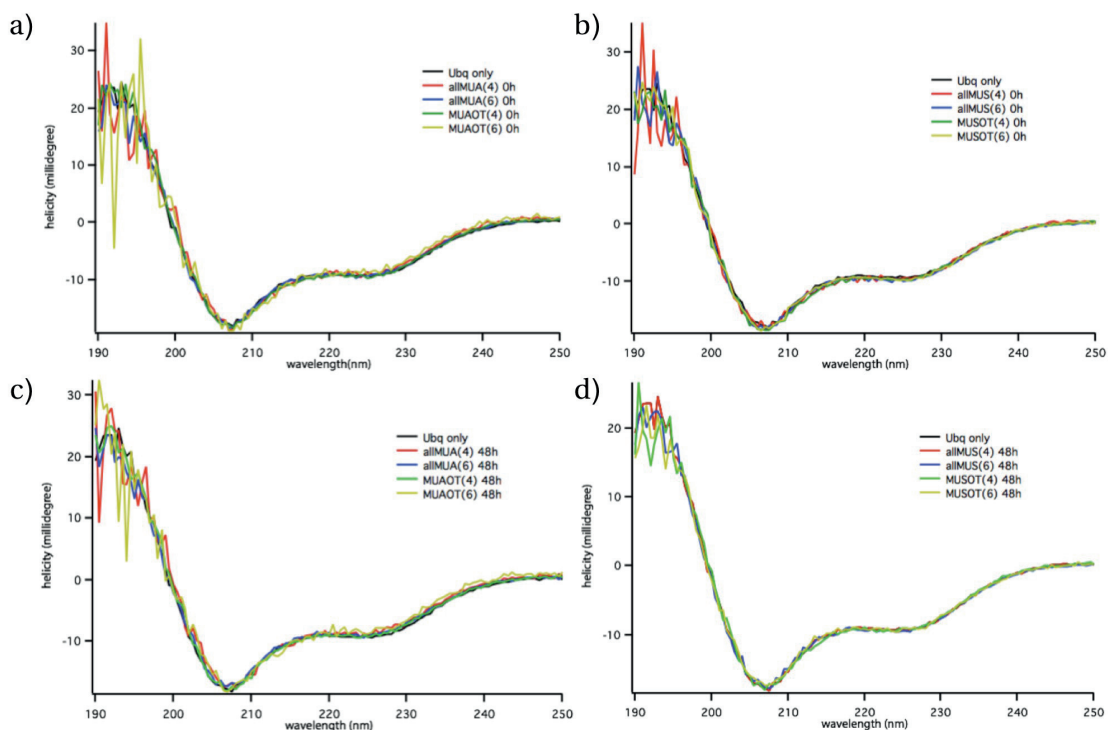
Figure 6.5: Circular dichroism (CD) spectra of a mixture of ubiquitin with a) carboxylate and b) sulfonate NPs right after mixing. c) and d) represent the same experiment after 48 hours of incubation. In any of the cases, difference in the protein conformation was not observed, i.e. the structural integrity of protein was protected upon nanoparticle's adhesion.

6.6). All of the CD spectra showed no change in ubiquitin's α-helices and β-sheets bands upon mixing with NP as characterized by a perfect overlapped with the ubiquitin's CD spectrum alone. This confirmed that conformation is retained upon contact with NPs even 48 hours after mixing.
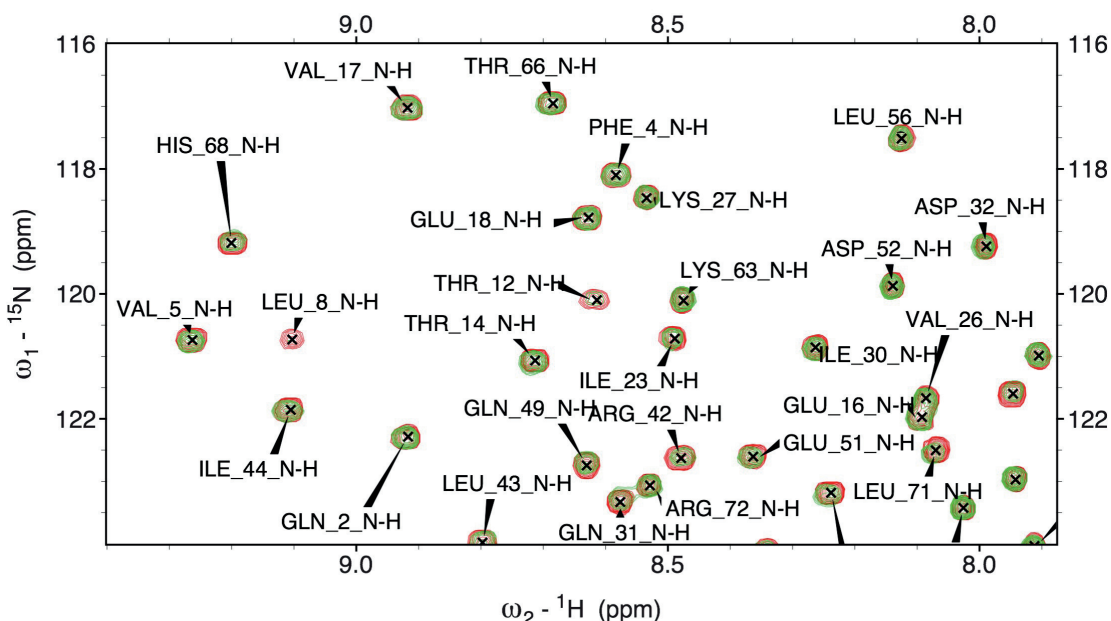
Figure 6.6: A portion of HSQC NMR spectrum of ubiquitin alone (red contours) overlaid with ubiquitin and allMUS(4) NPs mixture (green contours) in 10 mM phosphate buffer at pH 7.4. Unlike Calzolai *et.al.*, only intensity decrease in crosspeaks was observed. The disparity could be attributed to different NPs used in these work as well as the interaction kinetics.

6.6. Nanoparticles – Ubiquitin Binding with NMR Results

Later in this study, ^{1}H-^{15}N HSQC was carried out to characterize NP – binding at a molecular level. HSQC spectrum of ubiquitin was measured before and after addition of each NPs, followed by overlaid spectrum to compare differences in both cases. Possibly due to slow kinetics, we exclusively observed signal intensity decrease upon NP addition instead of chemical shift perturbation (Figure 6.7a). The intensity ratio of NP-protein mixture to protein alone gives characteristic peaks pertaining to strong
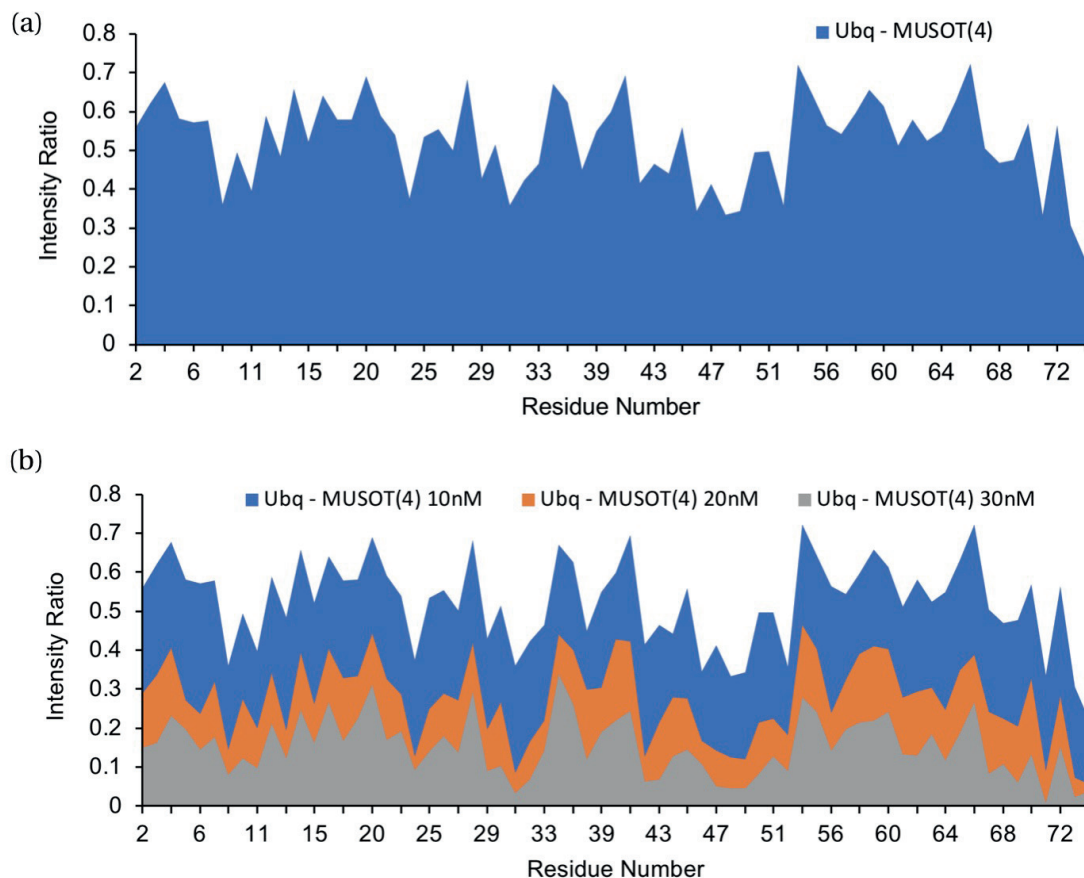
Figure 6.7: a) intensity ratios of amino acid crosspeaks with and without nanoparticle addition. Different nanoparticles may exhibit different degree of decrease in the overall spectrum even though molar stoichiometry between nanoparticles and protein is the same. This is why using a constant threshold value for all nanoparticles would not be analytically rigorous. b) In order to solve this problem, we calculated a threshold value for each nanoparticle-protein mixture separately by estimating average intensity ratio and standard deviation. The amino acid residues that lie above the standard deviation were attributed to signific
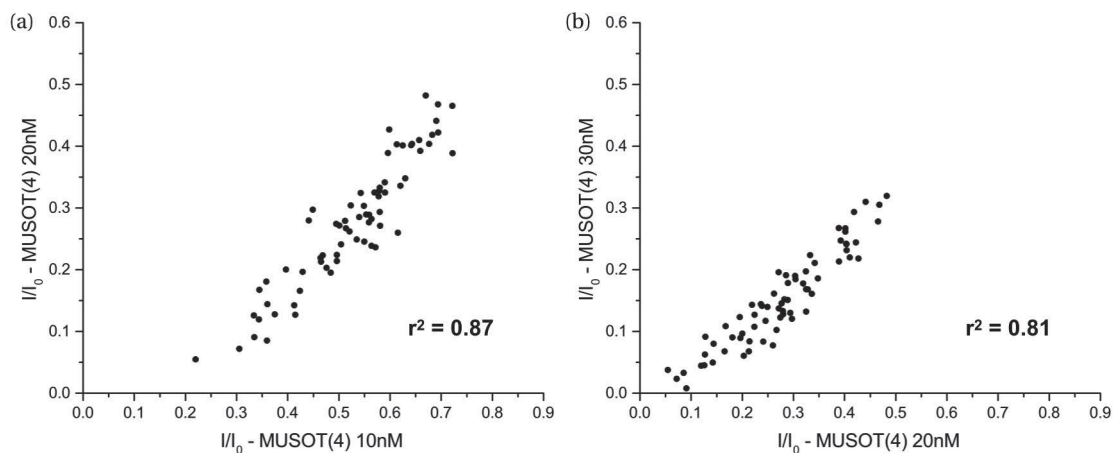
Figure 6.8: a) intensity ratio spectrum of allMUS(4) NPs. b) theoretical representation of the evolution of intensity ratio of binding residues with respect to NP concentration. c) The titration of ubiquitin with allMUS(4) resulted overall decrease in the whole sequence. Note that as NP concentration increase, significant decrease in some residues start to disappear again, probably due to crowding of proteins on NPs surface indistinguishably affect most of the amino acids. d) We did not obtain the full saturation of nanoparticles with protein titration for all nanoparticles used in this work and therefore do not exactly know where each nanoparticle corresponds in the ubiquitin adsorption isotherm.

binding that manifests as deeper wells in the AA residue spectrum (Figure 6.7a). The stronger the deviation of a particular AA residue in the spectrum with respect to the rest of the residues, the higher it is affected by NP adhesion and thus attributed to closer to contact point on protein. Increasing the temperature up to 40 °C with the intention of increasing the kinetics did not render any peak shift but rather exhibited deterioration of some of the peaks and hence was abandoned for the sake of reliability. Unlike protein – ligand interactions where the contact points are highly localized and well-defined, NP – protein binding could be somewhat more scattered.
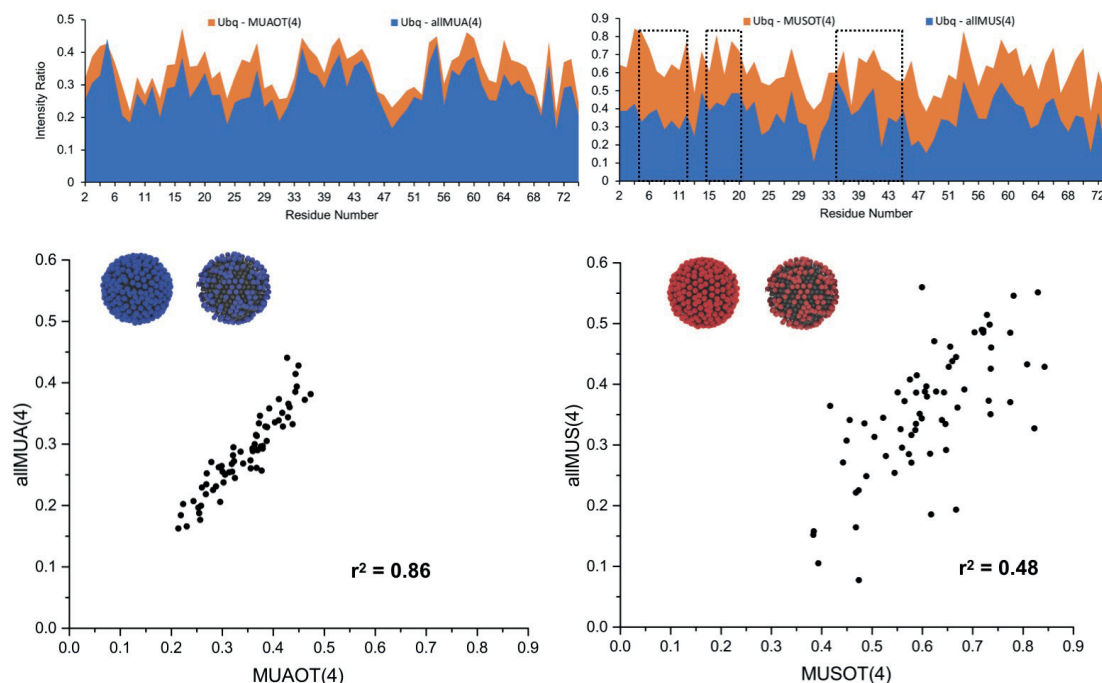
Figure 6.9: Intensity ratio maps and corresponding correlation plots for comparison of allMUA(4) vs MUAOT(4) and allMUS(4) vs MUSOT(4) NPs. Note the high correlation coefficient of carboxylate NPs indicating a substantial similarity in protein binding in contrast to sulfonate NPs where correlation is considerably low.

Due to large surface of NPs that is available to binding, protein can conform in different binding regimes. It is therefore imperative to demonstrate whether ubiquitin binding to our NPs is stochastic or specific to certain positions on protein. To this end, we carried out concentration study with some NPs and ubiquitin mixtures in HSQC spectra. For example, varying concentrations of MUSOT(4) NPs and fixed amount of ubiquitin was measured in HSQC NMR and the resulting intensity ratio map was compared (Figure 6.7b). Intensity ratio plots for different NP concentration pairs and resulting high correlation coefficients revealed that the

Table 6.2: All calculated correlation coefficients for each NP pair. Color coding for values is done with the following thresholds: 1.0 – 0.8 (green), 0.79-0.5 (orange) and 0.49-0.01 (red).

r²	allMUA(4)	MUAOT(4)	allMUS(4)	MUSOT(4)	allMUA(6)	MUAOT(6)	allMUS(6)	MUSOT(6)
allMUA(4)		0.865	0.429	0.395	0.836	0.690	0.541	0.669
MUAOT(4)			0.479	0.363	0.887	0.779	0.556	0.566
allMUS(4)				0.483	0.478	0.363	0.458	0.428
MUSOT(4)					0.291	0.170	0.482	0.472
allMUA(6)						0.813	0.544	0.542
MUAOT(6)							0.423	0.371
allMUS(6)								0.747
MUSOT(6)								

binding behavior of ubiquitin is specific and do not change with varying concentrations of NPs (Figure 6.8). The fact that the binding is not stochastic allowed us to reliably compare different types of NPs in terms of protein binding.

The second step was to compare different NPs types in terms of ubiquitin binding in molecular level. Intensity ratio plots and subsequent calculation of correlation coefficients showed an interesting disparity. While for some NPs such as MUAOT(4) and allMUA(4) the protein binding is highly similar with very high correlation coefficients, some other NPs such as MUSOT(4) and allMUS(4) can deviate quite substantially (Figure 6.9). With all the other parameters being constant, this information suggests that protein binding characteristics may or may not depend on NP surface characteristics (mixed ligand or homoligand) based on the surface chemistry of NPs (sulfonate vs. carboxylate). Calculation of correlation coefficients for each single NP pairs highlighted a broader picture on ubiquitin binding: surface chemistry is seemingly the most dominant effect exhibiting high disparity on protein binding (Table 6.2). In addition, size and surface hydrophobicity are also important
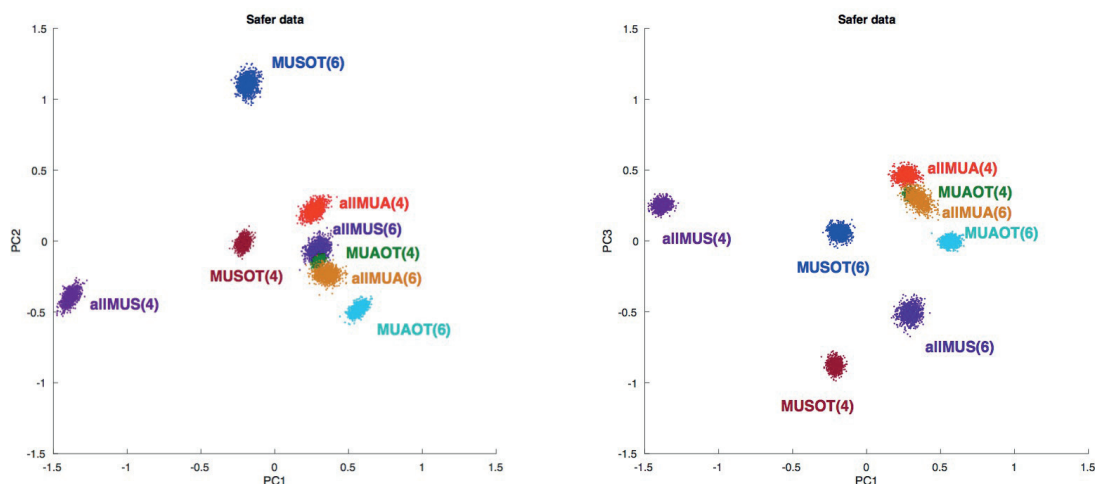
Figure 6.10: Principal component analysis of all NP sets combined. The spatial separation of NPs indicates the difference in terms of protein binding. As such, carboxylate NPs are found to be clustering around each other while sulfonate NPs are somewhat more scattered.

factors but their effect is not universal and bound to certain surface chemistry. This detail was clearer on principal component analysis (PCA) of the whole 8 NP set. The combination of first 3 principal components (PC) and plotting against each other demonstrated a separation of sulfonate and carboxylate NPs in general. More detailed investigation revealed that all carboxylate NPs are somewhat clustered around each other regardless of their sizes and surface hydrophobicity. In contrast, sulfonate NPs are more scattered around PC plots, indicating different protein binding behavior. In particular, within the same size family, allMUS and MUSOT NPs show quite distinct binding characteristics while allMUA and MUAOT NPs are virtually same in that respect (Figure 6.10).

6.7. Hydrodynamic Analysis of Nanoparticles with AUC
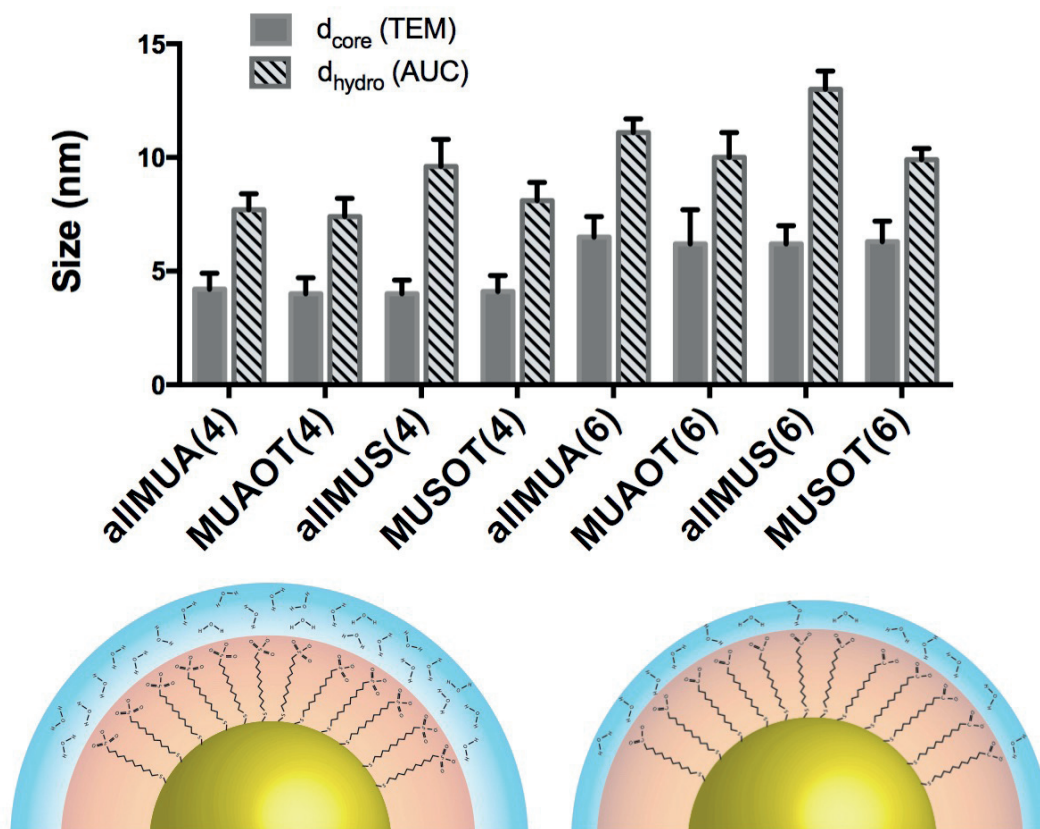
Figure 6.11: Hydrodynamic and core diameters of NPs obtained from AUC and TEM experiments respectively. Assuming the ligand length is similar in sulfonate and carboxylate NPs, the difference between these two values gives a hint on the hydration layer thickness. It is evident that there is a discrepancy between allMUS and MUSOT NPs in terms of the hydration layer while allMUA and MUAOT NPs are somewhat similar. This behavior perfectly correlates with the HSQC NMR results on ubiquitin binding, indicating the role of hydration layer on protein binding.

As discussed previously, AUC is a robust method to characterize hydrodynamic parameters of NPs requiring no standard experiments and little *a priori* information
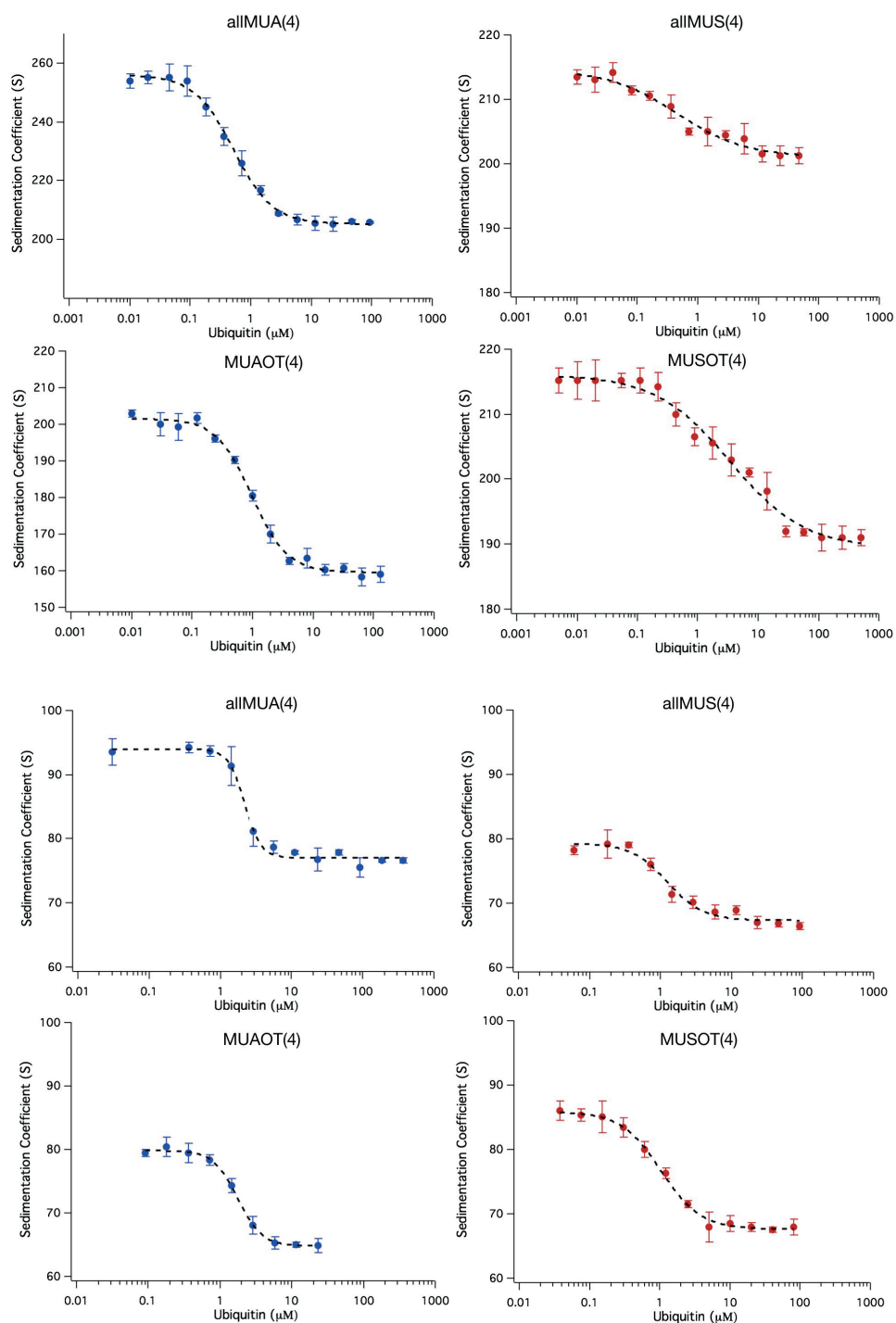
Figure 6.12: Sedimentation coefficient plots upon ubiquitin titration to NPs in AUC experiments. Note the fit lines calculated from equation 5.6 represent the experimental data with high quality.

on the sample [122]. Based on this method, hydrodynamic diameters (d_{hyd}) of all of our NPs were calculated from sedimentation and diffusion coefficients individually. Combining the results with core diameter of NPs that were obtained from TEM images revealed an interesting correlation: within the same size family, the difference between hydrodynamic diameter and core diameter indicates the organic surface layer of NPs and their hydration shells (Figure 6.11). Based on the highly similar values for allMUA and MUAOT NPs for both 4 nm and 6 nm core diameters, the hydration shell thickness do not change upon addition of hydrophobic OT ligands. However, between allMUS and MUSOT NPs, there is a clear decrease of

hydrodynamic diameter when OT ligands are put on NP surfaces. This suggests that the hydration layer of sulfonate NPs are dramatically affected by the presence of secondary ligands with less thick water layer around them. Interestingly, the overall behavior perfectly overlaps with the HSQC NMR results where carboxylate NPs are similar in protein binding while sulfonate NPs show great disparity. We hypothesize that the effect of hydrophobicity on protein binding can be correlated with its effect on hydration layer around NPs. This could be somewhat intuitive as protein needs to replace water layer to bind to the surface ligands of NPs and therefore could spatially conform itself to pay the least entropic penalty for removing ordered water layer around NPs. Of course, further experiments remain to be done to prove the direct correlation of hydration layer and its effect on protein binding.

6.8. Binding Affinity and Stoichiometry of NP-Ubiquitin Interactions

Thermodynamic parameters of ubiquitin binding such as binding affinity (K_D) and maximum number of protein bound per NP (N_{max}) for all NPs were calculated using the AUC methodology described in chapter 5. While NPs concentrations were kept constant during the titration (between 10-30 nM), ubiquitin concentration was varied 4-6 orders of magnitude. The resulting average sedimentation coefficient corresponding to each titration points were plotted and fitted to the equation 5.6 using ubiquitin parameters instead of BSA. All of the fit lines reliably represented the experimental data points as can be seen in figure 6.12.

All of the extracted KD and Nmax information was summarized in the Figure 6.13. Apparently, except for the 6 nm sulfonate NPs, binding affinity values are invariant among different types of NPs. As per protein stoichiometry per NP, there are some variations between NPs but it is not as systematic as in NMR experiments. All of this information highlights the lack of correlation between the molecular level binding differences among the NPs we found with HSQC NMR experiments and their thermodynamic binding parameters. Because HSQC NMR experiment gives local and highly specific information whereas AUC provides a global interaction parameter, such lack of correlation could be expected. This demonstrates that even though the local binding information is quite specific, there are other factors such as flexibility of certain side chains that were not taken into account in our HSQC experiments which could contribute to the global binding scheme.

Combination of all NPs features effect in various binding studies allow us to reach the following conclusion: size, surface chemistry and hydrophobicity are crucial
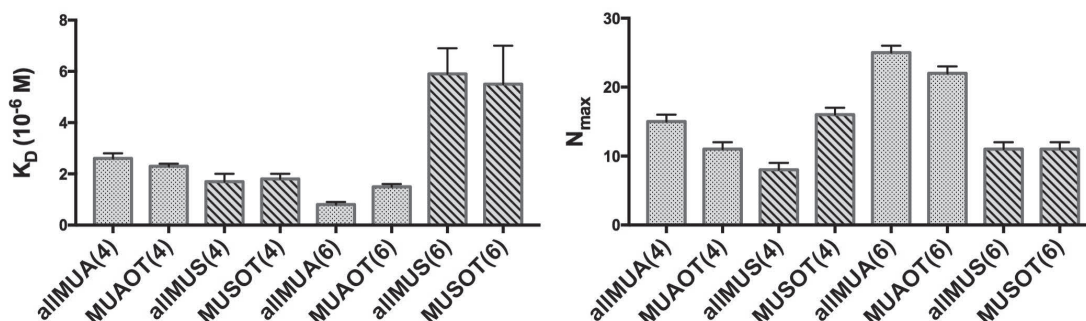
Figure 6.13: Binding parameters, K_D and N_{max} obtained from AUC experiments. Apart from 6 nm sulfonate NPs, binding affinity is similar among NPs. Nmax is somewhat more diverse but we could not find any monotonic behavior among different types of NPs.

parameters that influence thermodynamics and mechanism of ubiquitin binding to NPs, but they may not have universal and consistent effect among all NPs. Although for some cases we observed correlation of binding thermodynamics and mechanism, it was difficult to find a general rule that fits to all. This, in fact, demonstrates the intricate effects of NP parameters that may not be deconvoluted with simple terms.

6.9. Molecular Information on Ubiquitin Binding to NPs

To begin with, G75 and G76 residues were removed from analysis due to their extremely varied intensities with large deviations which might result in overestimation or underestimation of the degree of signal decrease for other AA residues. Among binding residues, L71 and L74 were found to be exclusively existent in all NP types possibly due to its flexibility which also renders this part of the protein responsible for most of the binding and dimerization in biological processes. The absence of R72 in all NP types, however, suggests the binding is not merely due to

102

allMUS(4)   MUSOT(4)

Figure 6.14: Binding residues represented in 3D crystal structure of ubiquitin (PDB code: 1UBQ) for allMUS(4) and MUSOT(4).

flexibility, but also spatial arrangement of AA residues plays a role. That is, even though R72 is positively charged, it faces towards the other side of L71 and L74 residues and not affected from binding which indicates spatially selective binding.

One of the most distinct pattern in terms of binding regions on ubiquitin was observed in allMUS(4) NPs. First, they are bound to the least amount of AA residues with less distinct binding regions compared to other NPs. Except for Q31, all of the other interacting residues (R42, A46, G47, Q49, L71, L73 and R74) are spatially aligned in a continuous way on the lateral side of ubiquitin which creates almost one complete binding region. In contrast, ubiquitin binds preferentially from two distinct regions to MUSOT(4) NPs, namely (i) I13, I30, Q31, D32, I36, L71, L73 and R74 and (ii) G47, K48, Q49 and L50. First binding region is somewhat similar to allMUS(4) NPs but contains additional hydrophobic residues possibly due to more hydrophobic nature of mixed-ligand shell of MUSOT(4). Additional hydrophobic L67 residue is also affected in binding although it is spatially far from the main binding site and facing
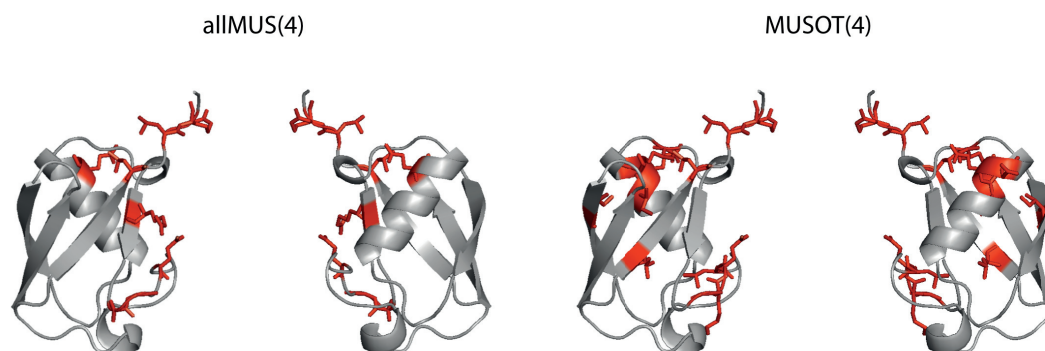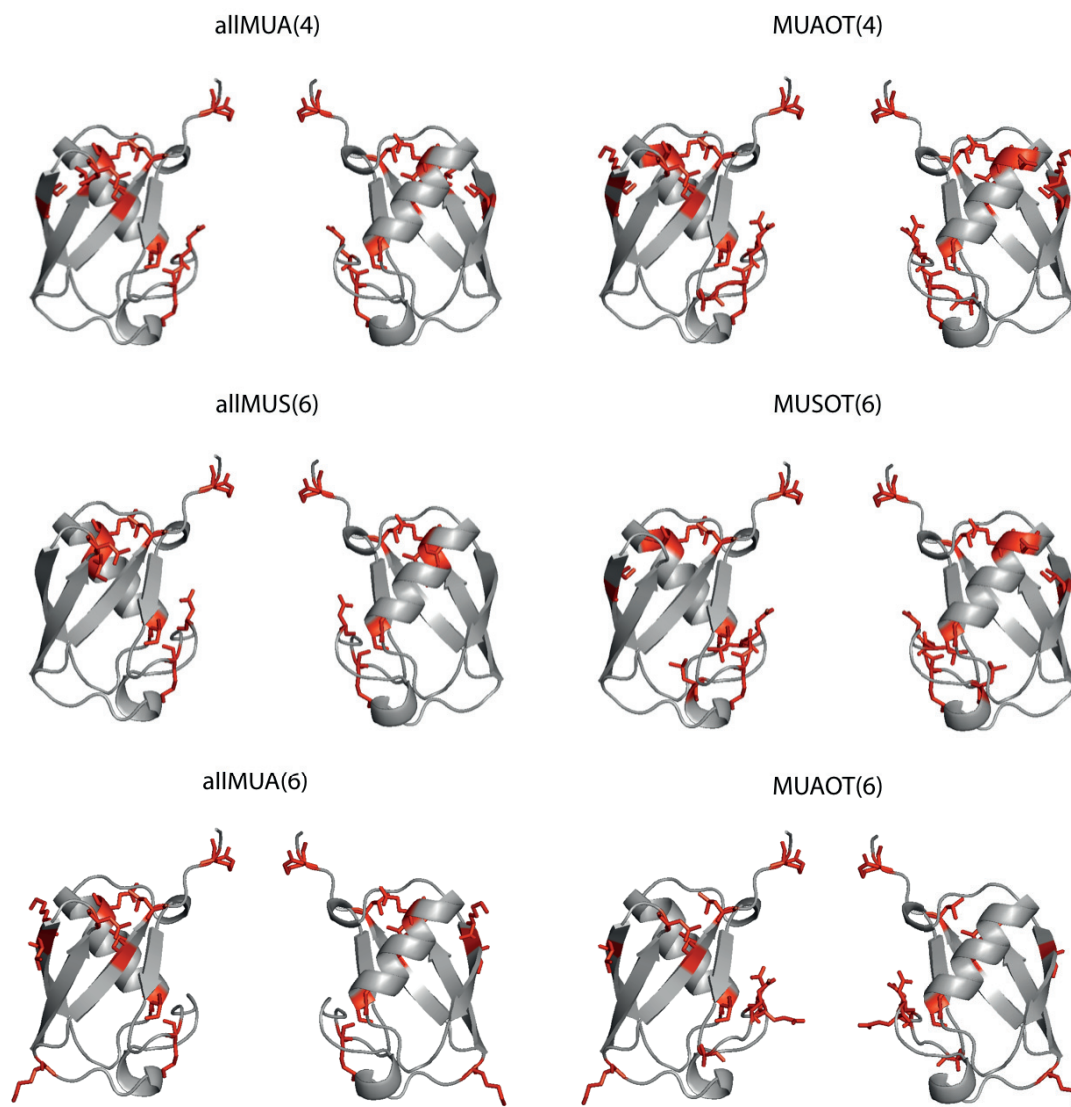
Figure 6.15: Binding residues represented in 3D crystal structure of ubiquitin (PDB code: 1UBQ) for allMUS(6), MUSOT(6), allMUA(4), MUAOT(4), allMUA(6) and MUAOT(6).

inwards of protein backbone. This might be due to penetration of hydrophobic ligands within the protein backbone from the main binding site which also explains

the binding to I13 residue in the same context. However, being close proximity with binding region 2 suggests that this residue could belong to that particular binding region although similar hydrophobic penetration is still necessary due to the AA being not exposed from this side as well. This interpretation might make more sense when considering allMUA(4) and MUAOT(4) NPs in which I23 residue which is closer to secondary binding site was affected. Similar to allMUS(4) vs MUSOT(4), MUAOT(4) involves more AA residues in binding with additional hydrophobic and polar groups compared to homoligand allMUA(4) NPs. In 6 nm NPs, carboxylate NPs are almost identical in terms of binding region while they deviate from sulfonate NPs. In general, the main difference between both 4 nm and 6 nm sized carboxylate NPs and sulfonate NPs are additional residues involved in first binding site such as T7, L8, K11, T12 which extends the binding region towards the residues that form beta sheets in the protein.

Overall, color-mapped 3D cartoon representation of ubiquitin binding residues shows considerable differences among sulfonate and carboxylate NPs for both 4 nm and 6 nm sizes. In this scheme, ubiquitin was generally found to bind to NPs from two different orientations which create two separate binding regions. The degree of extension of each binding regions is demonstrated to be specific to some NPs types with different AA residues contributing in addition to main binding site. 4 nm sulfonate NPs are most distinct in terms of binding regions while spatially different binding regions were identified between sulfonate and carboxylate NPs which potentially affect the positioning of protein on NPs surface and thus the total number of protein per NPs due to geometrical considerations.

6.10. Conclusion

With the help of ^{1}H-^{15}N HSQC NMR technique, molecular level information on ubiquitin binding to 4 nm and 6 nm gold NPs with different chemistry and hydrophobicity were obtained. NPs' characteristics evidently play an important role in dictating protein binding to the surface. AUC analysis of ubiquitin binding complemented this information with thermodynamic interaction parameters. These distinct behaviors were explained in terms of NPs hydration shell differences demonstrated by AUC characterization of NPs alone. In conclusion, it has been shown that a full description of NP-protein binding is necessary to construct reliable structure-property relationships which potentially influence the design of novel nanomaterials for nanomedicine applications.

CHAPTER 7

7. OUTLOOK AND CONCLUSIONS

The methods developed in this thesis paved the way for new avenues to study regarding structure-property relations of NP-protein interactions as well as competitive binding of different proteins on the same NPs. The work in this context carried out so far will be outlined in this chapter with the final conclusions thereafter.

7.1. Ongoing and Future Work

7.1.1. Competitive NP-Protein Binding Study with AUC

About 50 years ago, with ellipsometric measurements, Vroman and Adams demonstrated rapid exchange of fibrinogen by other proteins in serum at liquid/solid interfaces [157]. Afterwards, competitive displacement of proteins already adsorbed to a surface by other proteins with stronger affinities was termed 'Vroman effect'. As NPs also present energetic surface where proteins adsorb and hence create protein corona, Vroman effect is naturally thought to be valid. However, there are very few examples of the presence of this effect for NPs. One study employed quartz crystal microbalance (QCM) to investigate competitive binding of BSA and cytochrome C (CytC) onto MUA coated NPs but NPs were stabilized on gold surfaces which do not accurately reflect the colloidal dynamics of NPs in blood. I think, the most critical factor that restricts the existence of such investigation is methodological. That is, one needs to have a method that exhibits at least two
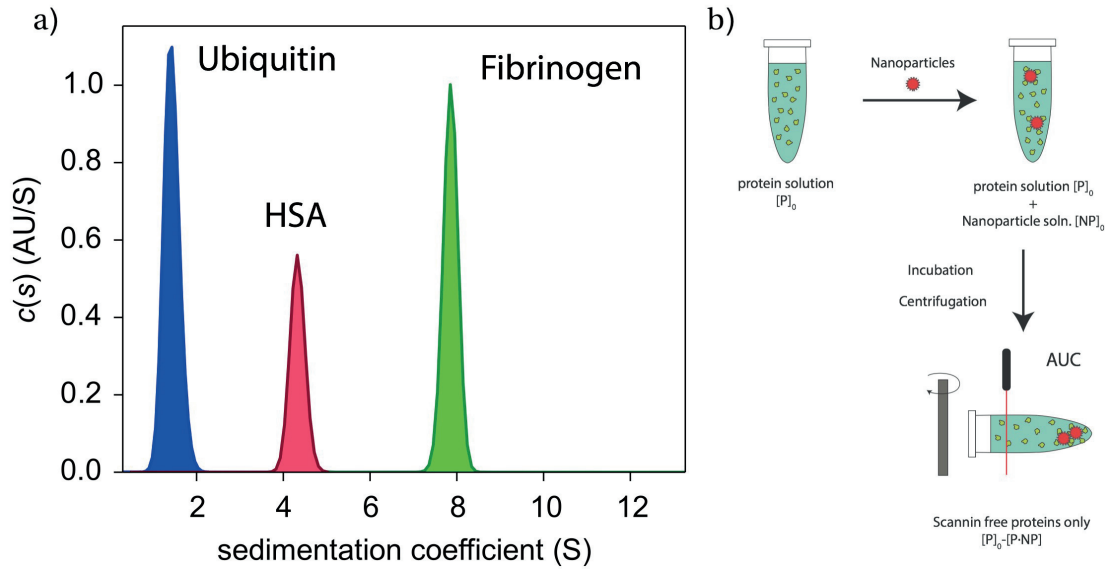
Figure 7.1: a) Sedimentation coefficient distribution of mixtures of ubiquitin, HSA and fibrinogen. The area under the curves gives quantitative information on the molar ratio of each protein in the mixture. b) schematic description of proposed protocol for competitive protein adhesion analysis in AUC.

separate signals from two different proteins upon binding to the same NPs. Free proteins should also be accounted for in the signal spectrum so as to distinguish adsorption and desorption processes of proteins. Such specificity unfortunately cannot be achieved with most of the colloidal characterization systems, especially without selectively labelling proteins, for instance, with separate dyes.

My hypothesis is that, AUC, as being a quantitative protein characterization method, can overcome this limitation. In order to assess whether AUC is selective and quantitative enough with proteins alone, a test AUC study with multiple proteins was carried out. A mixture of ubiquitin, human serum albumin and fibrinogen with

known concentrations was run with AUC and *c(s)* analysis have been done. According to *c(s)* distribution, each protein was separately observable, residing on their average sedimentation coefficients. Since their molecular weight is different, their sedimentation coefficients are different and therefore can be separated in the distribution. The integration of the area provided the relative signal concentrations of each protein which was found to be matching with the calculated values based on their extinction coefficients.

Next, sedimentation velocity experiment of protein-NP mixture has been carried out. The idea is that when protein-NP complexes are in equilibrium, very fast centrifugation could separate them from the solution, leaving only free proteins in AUC. Subsequent *c(s)* distribution can reveal the concentration of free proteins from which it is possible to calculate the NP-bound protein concentration.

Recently, Sahneh *et. al.* has developed a mathematical model for describing the dynamics of multiple protein binding to NPs surface from population balance equations [144]. According to their model, as time approaches infinity, slow dynamics accompanying dissociation of proteins and subsequent replacement by other proteins is in equilibrium where stable composition of multiple proteins on NP surface is achieved. In this case, the following relation can be approximated:

$$[P_i . NP] = n_i \frac{K_i^A [P_i]_0}{1 + \sum_{j=1}^m K_j^A [P_j]_0} [NP]_0 \qquad (7.1)$$

where K_i^A is the equilibrium constant of type *i* proteins. To put it more simply, in case of two different proteins in solution, Equation (7.1) suggests that once binding
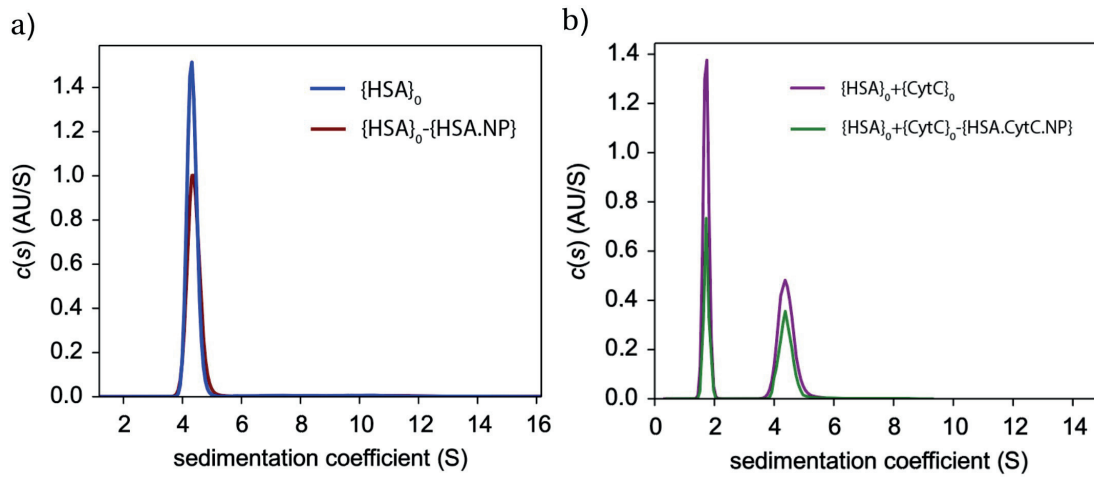
Figure 7.2: a) Sedimentation analysis of HSA in the absence and presence of 14nm MUA coated gold NPs. A clear decrease in the amount of protein is observed due to attachment of some of the HSA to NPs. b) When a mixture of HSA and cytochrome C were used, decrease in both protein's concentration were observed.

affinities of each protein and stoichiometry are known, the amount of bound proteins can be calculated or *vice versa*. AUC has already been presented as a method to calculate binding affinities and stoichiometry of individual protein-NP pairs. Thus, if we can calculate the amount of bound proteins $[P_i.NP]$ independent from this equation, we will be able to estimate binding affinities of each protein.

Although the quantification of free protein can also be done by simple centrifugation and absorption spectrometry, AUC's real power will be revealed when multiple proteins are used. In this regard, preliminary qualitative AUC experiments with CytC and HSA in the presence of 14 nm MUA coated gold NPs demonstrated remarkable difference in terms of signal concentration when compared to proteins analyzed

alone with the same concentration. Further calculations remain to be done to quantify the stoichiometry of each protein per NP. These findings can then be confirmed by using Equation 7.1 and binding affinity and stoichiometry of each protein calculated separately.

There are multiple advantages of the proposed experimental approach for competitive binding:

- First of all, AUC allows to distinguish each protein separately, therefore there is no need to impart any modifications to proteins or NPs in order to obtain separate signals.
- NP-protein complexes can be fractionated from free proteins *in situ* and directly measured in AUC. This removes the necessity of pipetting free proteins from the mixture after centrifugation which is an important source of experimental errors in NP-protein interactions.
- Since NPs are separated from the solution at the beginning of the experiment and bound proteins are investigated indirectly, the method is simply applicable to any size, shape and heterogeneity of NPs.

On the other hand, in order for the method to be valid, a measurable decrease in concentration must be present. This requires an optimization of protein and NP concentration used in the experiment. Too little NPs may not seize enough protein from solution based on its binding isotherm, while too little protein amount could simply not be detected in AUC as long as absorption detection system is used. The latter problem can be addressed with high sensitive fluorescence optics in future.

7.1.2. Size Scaling of Protein Binding Affinity and Stoichiometry for Sub-10 nm Gold NPs

The optimization of ligand exchange synthetic protocol for monodisperse gold NPs with various ligands allow to create multiple sets of high quality NPs with different ligands and size. These NPs can then be investigated in terms of protein binding affinity and stoichiometry through AUC analysis. The result of the study will demonstrate how binding affinities and stoichiometry scale with size of NPs less than 10 nm in diameter. In addition, the scaling can be compared among different types of NPs, for instance MUS, MUSOT, MUA, MUAOT, PEG coated NPs to study the effect of surface chemistry, charge and hydrophobicity. We think size dependency on protein binding to NPs might be different given the discrepancies we found in NMR studies in Chapter 6 where sulfonate and carboxylate NPs with changing hydrophobicity were investigated. Also, the study can be replicated for various types of proteins as different binding nature of each protein may reveal distinct size relation. Eventually the aim is to construct structure-property relationship pertaining to protein binding to NPs in order to have thorough understanding of size, surface chemistry and hydrophobicity effect on protein binding event.

7.1.3. Potential NMR Studies for Nanoparticle-Protein Interactions

In this thesis, ^{1}H-^{15}N HSQC NMR was demonstrated to be powerful tool for determination of protein binding residues to NP surface at molecular level detail. Although for the sake of consistency, studies herein were centered around one protein, namely ubiquitin, many small and medium size proteins as well as various types of NPs can potentially be investigated with the same approach using HSQC
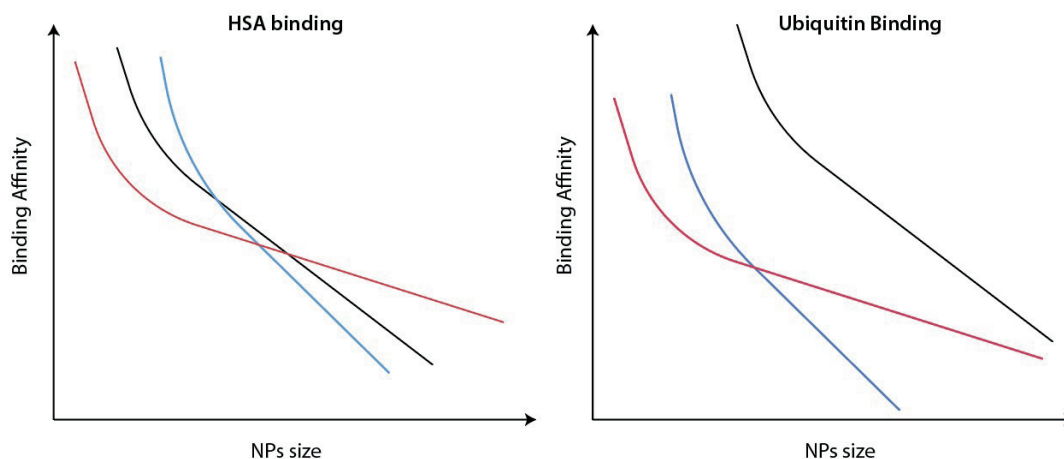
Figure 7.3: The schematic relation between size of nanoparticles and protein binding affinity. Lines with different colors represents NPs with theoretically different surface ligands.

NMR. In addition to generic studies of NP-protein interactions, HSQC NMR experiments can be applied to answer specific questions pertaining NP's interactions with biological entities. For instance, recent work published by our group demonstrated a unique ability of MUS coated NPs that mimic heparan sulfate proteoglycans and irreversibly deform the virus structure. Molecular dynamic simulations described the potential binding mechanism of NPs to capsid protein pentamers which initiates the destructive events of virus membrane. In order to elucidate this mechanism and other selective interactions between NPs and capsid proteins, HSQC NMR could be highly valuable asset. Another study in our group recently discovered discriminative adsorption of particular type of NPs on amyloid fibers. While cryo-TEM images exhibit highly ordered alignment of NPs onto surface features of Aβ1-40 and α-synuclein fibers, the exact mechanism remains to be solved. Again, NMR methodologies could shed light on identifying interacting residues and

thus contribute to the understanding of NP-amyloid interactions. Of course, one is not limited only to solution phase NMR spectroscopy for these applications. Combined with magic angle spinning technique, solid-state NMR spectroscopy also offers plenty of opportunities, particularly to capture aggregation states of proteins with NPs which could be ideal for amyloid-like proteins-NP interactions.

7.2. Conclusions

The ramifications of protein-NP interactions that were outlined in the beginning of this thesis motivated us to explore novel ways to characterize the binding in various aspects. First, we presented a powerful nanomaterial characterization tool, AUC, as a basis for the methodology we developed in order to estimate thermodynamic parameters for protein binding. This method was shown to be robust, mostly unaffected by contaminations/aggregates and do not become more complicated even with extremely small NPs.

Secondly, we utilized ^{1}H-^{15}N HSQC NMR for obtaining molecular level information on protein binding to sub-10 nm gold NPs. We optimized data analysis method in order to compare different size and types of gold NPs reliably. According to this protocol, we observed that protein binding can be highly dependent on surface chemistry which can also be a distinguishing factor for size dependency. That is, for instance, unlike carboxylate NPs, sulfonate NPs exhibit disparate binding modes to ubiquitin based on their size and surface hydrophobicity. We also combined AUC binding studies to obtain thermodynamic information on ubiquitin binding and reasoned that such dependency on surface chemistry can be linked to different hydration layer of NPs which was in turn reflected to overall hydrodynamic diameter.

Overall, in this thesis, I have developed methods to investigate protein-NP binding event with different aspects, such as thermodynamics and mechanism. I tried to answer how surface chemistry, size and surface hydrophobicity are correlated to protein binding modes for small NPs. Throughout my PhD work, I extensively worked on 'perfecting' gold NPs in terms of synthesis, separation and characterization which helped me to control different characteristics of NPs carefully. These well-characterized and highly homogeneous NPs allowed me to reliably interpret the data I obtained from other experiments. In this sense, I strongly believe that the high quality I achieved in these NPs also built the foundation of the other studies presented in this thesis. Ongoing projects was also shown to offer answering more advanced questions regarding protein-NP interactions. Therefore, the future of these projects seems quite open with multiple avenues for further discoveries.

8. BIBLIOGRAPHY

[1]   D. Bobo, K.J. Robinson, J. Islam, K.J. Thurecht, S.R. Corrie, Nanoparticle-Based Medicines: A Review of FDA-Approved Materials and Clinical Trials to Date, Pharm Res. 33 (2016) 2373–2387. doi:10.1007/s11095-016-1958-5.

[2]   M.L. Etheridge, S.A. Campbell, A.G. Erdman, C.L. Haynes, S.M. Wolf, J. McCullough, The big picture on nanomedicine: the state of investigational and approved nanomedicine products, Nanomedicine: Nanotechnology, Biology and Medicine. 9 (2013) 1–14. doi:10.1016/j.nano.2012.05.013.

[3]   B. Thiesen, A. Jordan, Clinical applications of magnetic nanoparticles for hyperthermia, International Journal of Hyperthermia. 24 (2009) 467–474. doi:10.1080/02656730802104757.

[4]   S.K. Libutti, G.F. Paciotti, A.A. Byrnes, H.R. Alexander, W.E. Gannon, M. Walker, et al., Phase I and pharmacokinetic studies of CYT-6091, a novel PEGylated colloidal gold-rhTNF nanomedicine, Clin Cancer Res. 16 (2010) 6139–6149. doi:10.1158/1078-0432.CCR-10-0978.

[5]   A.N. Kharlamov, A.E. Tyurnina, V.S. Veselova, O.P. Kovtun, V.Y. Shur, J.L. Gabinsky, Silica–gold nanoparticles for atheroprotective management of plaques: results of the NANOM-FIM trial, Nanoscale. 7 (2015) 8003–8015. doi:10.1039/C5NR01050K.

[6]   C. Loo, A. Lowery, N. Halas, J. West, R. Drezek, Immunotargeted nanoshells for integrated cancer imaging and therapy, Nano Lett. 5 (2005) 709–711. doi:10.1021/nl050127s.

[7]   C.H.J. Choi, L. Hao, S.P. Narayan, E. Auyeung, C.A. Mirkin, Mechanism for the endocytosis of spherical nucleic acid nanoparticle conjugates, Proc. Natl. Acad. Sci. U.S.a. 110 (2013) 7625–7630. doi:10.1073/pnas.1305804110.

[8]   S.A. Jensen, E.S. Day, C.H. Ko, L.A. Hurley, J.P. Luciano, F.M. Kouri, et al., Spherical nucleic acid nanoparticle conjugates as an RNAi-based therapy

for glioblastoma, Sci Transl Med. 5 (2013) 209ra152. doi:10.1126/scitranslmed.3006839.

[9]   V. Cagno, P. Andreozzi, M. D'Alicarnasso, P.J. Silva, M. Mueller, M. Galloux, et al., Broad-spectrum non-toxic antiviral nanoparticles with a virucidal inhibition mechanism, Nat Mater. 17 (2018) 195–203. doi:10.1038/nmat5053.

[10]   S. Wilhelm, A.J. Tavares, Q. Dai, S. Ohta, J. Audet, H.F. Dvorak, et al., Analysis of nanoparticle delivery to tumours, Nat. Rev. Mater. 1 (2016) 16014. doi:10.1038/natrevmats.2016.14.

[11]   W.C.W. Chan, Nanomedicine 2.0, Acc. Chem. Res. 50 (2017) 627–632. doi:10.1021/acs.accounts.6b00629.

[12]   D.M. Shin, M.E. Davis, Z.G. Chen, Nanoparticle therapeutics: an emerging treatment modality for cancer, Nat Rev Drug Discov. 7 (2008) 771–782. doi:10.1038/nrd2614.

[13]   L. Xu, C.-C. Huang, W. Huang, W.-H. Tang, A. Rait, Y.Z. Yin, et al., Systemic tumor-targeted gene delivery by anti-transferrin receptor scFv-immunoliposomes, Mol. Cancer Ther. 1 (2002) 337–346.

[14]   S.A. Wissing, O. Kayser, R.H. Müller, Solid lipid nanoparticles for parenteral drug delivery, Advanced Drug Delivery Reviews. 56 (2004) 1257–1272. doi:10.1016/j.addr.2003.12.002.

[15]   A.E. Nel, L. Mädler, D. Velegol, T. Xia, E.M.V. Hoek, P. Somasundaran, et al., Understanding biophysicochemical interactions at the nano–bio interface, Nat Mater. 8 (2009) 543–557. doi:10.1038/nmat2442.

[16]   J.M. Chan, P.M. Valencia, L. Zhang, R. Langer, O.C. Farokhzad, Polymeric Nanoparticles for Drug Delivery, in: Cancer Nanotechnology, Humana Press, Totowa, NJ, 2010: pp. 163–175. doi:10.1007/978-1-60761-609-2_11.

[17]   F. Masood, Polymeric nanoparticles for targeted drug delivery system for cancer therapy, Materials Science and Engineering: C. 60 (2016) 569–578. doi:10.1016/j.msec.2015.11.067.

[18]   K.M. El-Say, H.S. El-Sawy, Polymeric nanoparticles: Promising platform for drug delivery, Int J Pharm. 528 (2017) 675–691. doi:10.1016/j.ijpharm.2017.06.052.

[19]   Z. Liu, J.T. Robinson, S.M. Tabakman, K. Yang, H. Dai, Carbon materials for drug delivery & cancer therapy, Materials Today. 14 (2011) 316–323. doi:10.1016/S1369-7021(11)70161-4.

[20]   S.Y. Madani, A. Mandel, A.M. Seifalian, A concise review of carbon nanotube's toxicology, Nano Reviews. 4 (2013) 21521. doi:10.3402/nano.v4i0.21521.

[21]   Y. Song, Y. Li, Q. Xu, Z. Liu, Mesoporous silica nanoparticles for stimuli-responsive controlled drug delivery: advances, challenges, and outlook, Ijn. 12 (2017) 87–110. doi:10.2147/IJN.S117495.

[22]   Y. Tian, R. Guo, Y. Jiao, Y. Sun, S. Shen, Y. Wang, et al., Redox stimuli-responsive hollow mesoporous silica nanocarriers for targeted drug delivery in cancer therapy, Nanoscale Horiz. 1 (2016) 480–487. doi:10.1039/C6NH00139D.

[23]   J. Zhu, Y. Niu, Y. Li, Y. Gong, H. Shi, Q. Huo, et al., Stimuli-responsive delivery vehicles based on mesoporous silica nanoparticles: recent advances and challenges, J. Mater. Chem. B. 5 (2017) 1339–1352. doi:10.1039/C6TB03066A.

[24]   L.Y.T. Chou, K. Ming, W.C.W. Chan, Strategies for the intracellular delivery of nanoparticles, Chem Soc Rev. 40 (2011) 233–245. doi:10.1039/C0CS00003E.

[25]   Y.-L. Zhao, Z. Li, S. Kabehie, Y.Y. Botros, J.F. Stoddart, J.I. Zink, pH-Operated Nanopistons on the Surfaces of Mesoporous Silica Nanoparticles, J. Am. Chem. Soc. 132 (2010) 13016–13025. doi:10.1021/ja105371u.

[26]   M.W. Ambrogio, C.R. Thomas, Y.-L. Zhao, J.I. Zink, J.F. Stoddart, Mechanized silica nanoparticles: a new frontier in theranostic nanomedicine, Acc. Chem. Res. 44 (2011) 903–913. doi:10.1021/ar200018x.

[27]   F.A.S. Oluyomi S Adeyemi, Evaluation of metal nanoparticles for drug delivery systems, Journal of Biomedical Research. 29 (2015) 145–149. doi:10.7555/JBR.28.20130096.

[28]   T.B. Huff, L. Tong, Y. Zhao, M.N. Hansen, J.-X. Cheng, A. Wei, Hyperthermic effects of gold nanorods on tumor cells, Nanomedicine (Lond). 2 (2007) 125–132. doi:10.2217/17435889.2.1.125.

[29]   L. Yang, H. Kuang, W. Zhang, Z.P. Aguilar, H. Wei, H. Xu, Comparisons of the biodistribution and toxicological examinations after repeated intravenous administration of silver and gold nanoparticles in mice, Sci. Rep. 7 (2017) 3303–583. doi:10.1038/s41598-017-03015-1.

[30]   U. Prabhakar, H. Maeda, R.K. Jain, E.M. Sevick-Muraca, W. Zamboni, O.C. Farokhzad, et al., Challenges and Key Considerations of the Enhanced Permeability and Retention Effect for Nanomedicine Drug Delivery in Oncology, Cancer Res. 73 (2013) 2412–2417. doi:10.1158/0008-5472.CAN-12-4561.

[31]   A.H. Faraji, P. Wipf, Nanoparticles in cellular drug delivery, Bioorganic & Medicinal Chemistry. 17 (2009) 2950–2962. doi:10.1016/j.bmc.2009.02.043.

[32]   J. Rauch, S. Laurent, M. Mahmoudi, W. Kolch, Big Signals from Small Particles: Regulation of Cell Signaling Pathways by Nanoparticles, 113 (2013) 3391–3406. papers2://publication/uuid/67930E77-800B-4AFB-B1F5-C286261EFB3A.

[33]   E. Fröhlich, The role of surface charge in cellular uptake and cytotoxicity of medical nanoparticles, Ijn. 7 (2012) 5577–5591. doi:10.2147/IJN.S36111.

[34]   S. Hirn, M. Semmler-Behnke, C. Schleh, A. Wenk, J. Lipka, M. Schäffler, et al., Particle size-dependent and surface charge-dependent biodistribution of gold nanoparticles after intravenous administration, Eur J Pharm Biopharm. 77 (2011) 407–416. doi:10.1016/j.ejpb.2010.12.029.

[35]   Y.-H. Park, H.C. Bae, Y. Jang, S.H. Jeong, H.N. Lee, W.-I. Ryu, et al., Effect of the size and surface charge of silica nanoparticles on cutaneous toxicity,

Mol. Cell. Toxicol. 9 (2013) 67–74. doi:10.1007/s13273-013-0010-7.

[36]   A.E. Gregory, R. Titball, D. Williamson, Vaccine delivery using nanoparticles, Front Cell Infect Microbiol. 3 (2013) 13. doi:10.3389/fcimb.2013.00013.

[37]   R. Toy, P.M. Peiris, K.B. Ghaghada, E. Karathanasis, Shaping cancer nanomedicine: the effect of particle shape on the in vivojourney of nanoparticles, Nanomedicine. 9 (2014) 121–134. doi:10.2217/nnm.13.191.

[38]   B.D. Chithrani, A.A. Ghazani, W.C.W. Chan, Determining the Size and Shape Dependence of Gold Nanoparticle Uptake into Mammalian Cells, Nano Lett. 6 (2006) 662–668. doi:10.1021/nl052396o.

[39]   Y. Geng, P. Dalhaimer, S. Cai, R. Tsai, M. Tewari, T. Minko, et al., Shape effects of filaments versus spherical particles in flow and drug delivery, Nature Nanotech. 2 (2007) 249–255. doi:10.1038/nnano.2007.70.

[40]   P.M. Peiris, L. Bauer, R. Toy, E. Tran, J. Pansky, E. Doolittle, et al., Enhanced Delivery of Chemotherapy to Tumors Using a Multicomponent Nanochain with Radio-Frequency-Tunable Drug Release, ACS Nano. 6 (2012) 4157–4168. doi:10.1021/nn300652p.

[41]   S.E.A. Gratton, P.A. Ropp, P.D. Pohlhaus, J.C. Luft, V.J. Madden, M.E. Napier, et al., The effect of particle design on cellular internalization pathways, Proc. Natl Acad. Sci. 105 (2008) 11613–11618. doi:10.1073/pnas.0801763105.

[42]   P. Decuzzi, M. Ferrari, The adhesive strength of non-spherical particles mediated by specific interactions, Biomaterials. 27 (2006) 5307–5314. doi:10.1016/j.biomaterials.2006.05.024.

[43]   L. Pan, Q. He, J. Liu, Y. Chen, M. Ma, L. Zhang, et al., Nuclear-Targeted Drug Delivery of TAT Peptide-Conjugated Monodisperse Mesoporous Silica Nanoparticles, J. Am. Chem. Soc. 134 (2012) 5722–5725. doi:10.1021/ja211035w.

[44]   A. Accardo, L. Aloj, M. Aurilio, G. Morelli, D. Tesauro, Receptor binding

peptides for target-selective delivery of nanoparticles encapsulated drugs, Ijn. 9 (2014) 1537–1557. doi:10.2147/IJN.S53593.

[45]   C. Saraiva, C. Praça, R. Ferreira, T. Santos, L. Ferreira, L. Bernardino, Nanoparticle-mediated brain drug delivery: Overcoming blood-brain barrier to treat neurodegenerative diseases, J Control Release. 235 (2016) 34–47. doi:10.1016/j.jconrel.2016.05.044.

[46]   A. Verma, O. Uzun, Y. Hu, Y. Hu, H.-S. Han, N. Watson, et al., Surface-structure-regulated cell-membrane penetration by monolayer-protected nanoparticles, 7 (2008) 588–595. doi:10.1038/nmat2202.

[47]   R.P. Carney, Y. Astier, T.M. Carney, K. Voïtchovsky, P.H. Jacob Silva, F. Stellacci, Electrical method to quantify nanoparticle interaction with lipid bilayers, ACS Nano. 7 (2013) 932–942. doi:10.1021/nn3036304.

[48]   P. Andreozzi, R.C. Van Lehn, K. Voïtchovsky, M. Ricci, P.H.J. Silva, J. Reguera, et al., Lipid tail protrusions mediate the insertion of nanoparticles into model cell membranes, Nat Comms. 5 (2014) 4482. doi:10.1038/ncomms5482.

[49]   R.C. Van Lehn, P.U. Atukorale, A. Alexander-Katz, D.J. Irvine, Y.-S. Yang, R.P. Carney, et al., Effect of particle diameter and surface composition on the spontaneous fusion of monolayer-protected gold nanoparticles with lipid bilayers, Nano Lett. 13 (2013) 4060–4067. doi:10.1021/nl401365n.

[50]   R. Duncan, The dawning era of polymer therapeutics, Nat Rev Drug Discov. 2 (2003) 347–360. doi:10.1038/nrd1088.

[51]   S.T. Kim, K. Saha, C. Kim, V.M. Rotello, The Role of Surface Functionality in Determining Nanoparticle Cytotoxicity, Acc. Chem. Res. 46 (2012) 681–691. doi:10.1021/ar3000647.

[52]   S. Mondini, M. Leonzino, C. Drago, A.M. Ferretti, S. Usseglio, D. Maggioni, et al., Zwitterion-Coated Iron Oxide Nanoparticles: Surface Chemistry and Intracellular Uptake by Hepatocarcinoma (HepG2) Cells, Langmuir. 31 (2015) 7381–7390. doi:10.1021/acs.langmuir.5b01496.

[53]   W.D. Bancroft, New Books: Studien zur Lehre von den kolloiden Losungen, J. Phys. Chem. 13 (1908) 729–730. doi:10.1021/j150108a005.

[54]   T. Svedberg, Studien zur Lehre von den kolloiden Lösungen, von The Svedberg, Buchdruckerei E. Berling, 1907.

[55]   V. Mirshafiee, M. Mahmoudi, K. Lou, J. Cheng, M.L. Kraft, Protein corona significantly reduces active targeting yield, Chemical Communications. 49 (2013) 2557–2559. doi:10.1039/C3CC37307J.

[56]   A. Balbo, P.H. Brown, E.H. Braswell, P. Schuck, Measuring protein-protein interactions by equilibrium sedimentation, Curr Protoc Immunol. Chapter 18 (2007) Unit 18.8. doi:10.1002/0471142735.im1808s79.

[57]   G. Rivas, W. Stafford, A.P. Minton, Characterization of Heterologous Protein–Protein Interactions Using Analytical Ultracentrifugation, Methods. 19 (1999) 194–212. doi:10.1006/meth.1999.0851.

[58]   O. Lamm, Die Differentialgleichung der Ultrazentrifugierung, Ark. Mat. Astr. Fys. 21B (1929) 1–4.

[59]   C.A. Brautigam, Using Lamm-Equation modeling of sedimentation velocity data to determine the kinetic and thermodynamic properties of macromolecular interactions, Methods. 54 (2011) 4–15. doi:10.1016/j.ymeth.2010.12.029.

[60]   M.P. Monopoli, C. Åberg, A. Salvati, K.A. Dawson, Biomolecular coronas provide the biological identity of nanosized materials, Nature Nanotech. 7 (2012) 779–786. doi:10.1038/nnano.2012.207.

[61]   W. Hu, C. Peng, M. Lv, X. Li, Y. Zhang, N. Chen, et al., Protein Corona-Mediated Mitigation of Cytotoxicity of Graphene Oxide, ACS Nano. 5 (2011) 3693–3700. doi:10.1021/nn200021j.

[62]   A. Kumar, E.M. Bicer, A.B. Morgan, P.E. Pfeffer, M. Monopoli, K.A. Dawson, et al., Enrichment of immunoregulatory proteins in the biomolecular corona of nanoparticles within human respiratory tract lining fluid, Nanomedicine: Nanotechnology, Biology and Medicine. 12 (2016) 1033–

1043. doi:10.1016/j.nano.2015.12.369.

[63]   S. Wan, P.M. Kelly, E. Mahon, H. Stockmann, P.M. Rudd, F. Caruso, et al., The "Sweet" Side of the Protein Corona: Effects of Glycosylation on Nanoparticle-Cell Interactions, ACS Nano. 9 (2015) 2157–2166. doi:10.1021/nn506060q.

[64]   D. OWENSIII, N. PEPPAS, Opsonization, biodistribution, and pharmacokinetics of polymeric nanoparticles, Int J Pharm. 307 (2006) 93–102. doi:10.1016/j.ijpharm.2005.10.010.

[65]   A. Gessner, A. Lieske, B.R. Paulke, R.H. Müller, Influence of surface charge density on protein adsorption on polymeric nanoparticles: analysis by two-dimensional electrophoresis, European Journal of Pharmaceutics and Biopharmaceutics. 54 (2002) 165–170. doi:10.1016/S0939-6411(02)00081-4.

[66]   A. Gessner, A. Lieske, B.R. Paulke, R.H. Müller, Functional groups on polystyrene model nanoparticles: influence on protein adsorption, Journal of Biomedical Materials Research Part A. 65 (2003) 319–326. doi:10.1002/jbm.a.10371.

[67]   D.F. Moyano, K. Saha, G. Prakash, B. Yan, H. Kong, M. Yazdani, et al., Fabrication of Corona-Free Nanoparticles with Tunable Hydrophobicity, ACS Nano. 8 (2014) 6748–6755. doi:10.1021/nn5006478.

[68]   R. Safavi-Sohi, S. Maghari, M. Raoufi, S.A. Jalali, M.J. Hajipour, A. Ghassempour, et al., Bypassing Protein Corona Issue on Active Targeting: Zwitterionic Coatings Dictate Specific Interactions of Targeting Moieties and Cell Receptors, ACS Appl Mater Interfaces. 8 (2016) 22808–22818. doi:10.1021/acsami.6b05099.

[69]   R. Mout, D.F. Moyano, S. Rana, V.M. Rotello, Surface functionalization of nanoparticles for nanomedicine, Chem Soc Rev. 41 (2012) 2539–2544. doi:10.1039/C2CS15294K.

[70]   T. Mizuhara, D.F. Moyano, V.M. Rotello, Using the Power of Organic Synthesis for Engineering the Interactions of Nanoparticles with Biological

Systems, Nano Today. 11 (2016) 31–40. doi:10.1016/j.nantod.2015.11.002.

[71] C.-F. Wang, E.M. Mäkilä, C. Bonduelle, J. Rytkönen, J. Raula, S. Almeida, et al., Functionalization of alkyne-terminated thermally hydrocarbonized porous silicon nanoparticles with targeting peptides and antifouling polymers: effect on the human plasma protein adsorption, ACS Appl Mater Interfaces. 7 (2015) 2006–2015. doi:10.1021/am507827n.

[72] M.E. Norman, P. Williams, L. Illum, Human serum albumin as a probe for surface conditioning (opsonization) of block copolymer-coated microspheres, Biomaterials. 13 (1992) 841–849. doi:10.1016/0142-9612(92)90177-P.

[73] T. Cedervall, I. Lynch, M. Foy, T. Berggård, S.C. Donnelly, G. Cagney, et al., Detailed Identification of Plasma Proteins Adsorbed on Copolymer Nanoparticles, Angew. Chem. Int. Ed. Engl. 46 (2007) 5754–5756. doi:10.1002/anie.200700465.

[74] H. Bayraktar, P.S. Ghosh, V.M. Rotello, M.J. Knapp, Disruption of protein-protein interactions using nanoparticles: inhibition of cytochrome c peroxidase, Chem. Commun. 3 (2006) 1390–1392. doi:10.1039/b516096k.

[75] A.A. Vertegel, R.W. Siegel, J.S. Dordick, Silica Nanoparticle Size Influences the Structure and Enzymatic Activity of Adsorbed Lysozyme, Langmuir. 20 (2004) 6800–6807. doi:10.1021/la0497200.

[76] Martin Lundqvist, A. Ingmar Sethson, Bengt-Harald Jonsson, Protein Adsorption onto Silica Nanoparticles: Conformational Changes Depend on the Particles' Curvature and the Protein Stability, American Chemical Society, 2004. doi:10.1021/la0484725.

[77] P. Roach, D. Farrar, C.C. Perry, Surface tailoring for controlled protein adsorption: effect of topography at the nanometer scale and chemistry, J. Am. Chem. Soc. 128 (2006) 3939–3945. doi:10.1021/ja056278e.

[78] L. Shang, Y. Wang, J. Jiang, S. Dong, pH-Dependent Protein Conformational Changes in Albumin:Gold Nanoparticle Bioconjugates: A Spectroscopic

Study, Langmuir. 23 (2007) 2714–2721. doi:10.1021/la062064e.

[79]   F. Pederzoli, G. Tosi, M.A. Vandelli, D. Belletti, F. Forni, B. Ruozi, Protein corona and nanoparticles: how can we investigate on? Wiley Interdiscip Rev Nanomed Nanobiotechnol. 9 (2017). doi:10.1002/wnan.1467.

[80]   M. Mahmoudi, I. Lynch, M.R. Ejtehadi, M.P. Monopoli, F.B. Bombelli, S. Laurent, Protein–Nanoparticle Interactions: Opportunities and Challenges, Chem. Rev. 111 (2011) 5610–5637. doi:10.1021/cr100440g.

[81]   M. Lundqvist, I. Sethson, B.-H. Jonsson, High-Resolution 2D 1H– 15N NMR Characterization of Persistent Structural Alterations of Proteins Induced by Interactions with Silica Nanoparticles, Langmuir. 21 (2005) 5974–5979. doi:10.1021/la050569j.

[82]   K. Fischer, M. Schmidt, Pitfalls and novel applications of particle sizing by dynamic light scattering, Biomaterials. 98 (2016) 79–91. doi:10.1016/j.biomaterials.2016.05.003.

[83]   G. Maiorano, S. Sabella, B. Sorce, V. Brunetti, M.A. Malvindi, R. Cingolani, et al., Effects of Cell Culture Media on the Dynamic Formation of Protein–Nanoparticle Complexes and Influence on the Cellular Response, ACS Nano. 4 (2010) 7481–7491. doi:10.1021/nn101557e.

[84]   M.P. Monopoli, D. Walczyk, A. Campbell, G. Elia, I. Lynch, F.B. Bombelli, et al., Physical–Chemical Aspects of Protein Corona: Relevance to in Vitro and in Vivo Biological Impacts of Nanoparticles, J. Am. Chem. Soc. 133 (2011) 2525–2534. doi:10.1021/ja107583h.

[85]   D. Walczyk, F.B. Bombelli, M.P. Monopoli, I. Lynch, K.A. Dawson, What the Cell "Sees" in Bionanoscience, J. Am. Chem. Soc. 132 (2010) 5761–5768. doi:10.1021/ja910675v.

[86]   D. Docter, U. Distler, W. Storck, J. Kuharev, D. Wünsch, A. Hahlbrock, et al., Quantitative profiling of the protein coronas that form around nanoparticles, Nature Protocols. 9 (2014) 2030–2044. doi:10.1038/nprot.2014.139.

[87]   D.A. Mbeh, T. Javanbakht, L. Tabet, Y. Merhi, K. Maghni, E. Sacher, et al., Protein Corona Formation on Magnetite Nanoparticles: Effects of Culture Medium Composition, and Its Consequences on Superparamagnetic Nanoparticle Cytotoxicity, J Biomed Nanotechnol. 11 (2015) 828–840. doi:10.1166/jbn.2015.2000.

[88]   T. Cedervall, I. Lynch, S. Lindman, T. Berggård, E. Thulin, H. Nilsson, et al., Understanding the nanoparticle–protein corona using methods to quantify exchange rates and affinities of proteins for nanoparticles, Proc. Natl Acad. Sci. 104 (2007) 2050–2055. doi:10.1073/pnas.0608582104.

[89]   S. Tenzer, D. Docter, J. Kuharev, A. Musyanovych, V. Fetz, R. Hecht, et al., Rapid formation of plasma protein corona critically affects nanoparticle pathophysiology, Nature Nanotech. 8 (2013) 772–781. doi:10.1038/nnano.2013.196.

[90]   P.H. Brown, P. Schuck, Macromolecular size-and-shape distributions by sedimentation velocity analytical ultracentrifugation, Biophys. J. 90 (2006) 4651–4661. doi:10.1529/biophysj.106.081372.

[91]   J. Dam, P. Schuck, Calculating sedimentation coefficient distributions by direct modeling of sedimentation velocity concentration profiles, Methods in Enzymology. (2004).

[92]   P. Schuck, Sedimentation Analysis of Noninteracting and Self-Associating Solutes Using Numerical Solutions to the Lamm Equation, Biophys. J. 75 (1998) 1503–1512. doi:10.1016/S0006-3495(98)74069-X.

[93]   P.H. Brown, A. Balbo, P. Schuck, Characterizing protein-protein interactions by sedimentation velocity analytical ultracentrifugation, Curr Protoc Immunol. Chapter 18 (2008) Unit 18.15. doi:10.1002/0471142735.im1815s81.

[94]   K.E. van Holde, W.O. Weischet, Boundary analysis of sedimentation-velocity experiments with monodisperse and paucidisperse solutes, Biopolymers. 17 (1978) 1387–1403. doi:10.1002/bip.1978.360170602.

[95]   V. Mittal, A. Völkel, H. Cölfen, Analytical Ultracentrifugation of Model Nanoparticles: Comparison of Different Analysis Methods, Macromol Biosci. 10 (2010) 754–762. doi:10.1002/mabi.200900446.

[96]   B. Demeler, K.E. van Holde, Sedimentation velocity analysis of highly heterogeneous systems, Anal. Biochem. 335 (2004) 279–288. doi:10.1016/j.ab.2004.08.039.

[97]   P. Schuck, M.A. Perugini, N.R. Gonzales, G.J. Howlett, D. Schubert, Size-Distribution Analysis of Proteins by Analytical Ultracentrifugation: Strategies and Application to Model Systems, Biophys. J. 82 (2002) 1096–1111. doi:10.1016/S0006-3495(02)75469-6.

[98]   K. Planken, B. Kuipers, A. Philipse, Model Independent Determination of Colloidal Silica Size Distributions via Analytical Ultracentrifugation, Anal. Chem. (2008) –. doi:10.1021/ac801556t.

[99]   I.K. MacGregor, A.L. Anderson, T.M. Laue, Fluorescence detection for the XLI analytical ultracentrifuge, Biophysical Chemistry. 108 (2004) 165–185. doi:10.1016/j.bpc.2003.10.018.

[100]   E. Karabudak, E. Brookes, V. Lesnyak, N. Gaponik, A. Eychmüller, J. Walter, et al., Simultaneous Identification of Spectral Properties and Sizes of Multiple Particles in Solution with Subnanometer Resolution, Angew. Chem. Int. Ed. Engl. 55 (2016) 11770–11774. doi:10.1002/anie.201603844.

[101]   J. Walter, K. Löhr, E. Karabudak, W. Reis, J. Mikhael, W. Peukert, et al., Multidimensional Analysis of Nanoparticles with Highly Disperse Properties Using Multiwavelength Analytical Ultracentrifugation, ACS Nano. 8 (2014) 8871–8886. doi:10.1021/nn503205k.

[102]   W. Mächtle, High-Resolution, Submicron Particle Size Distribution Analysis Using Gravitational-Sweep Sedimentation, Biophys. J. 76 (1999) 1080–1091. doi:10.1016/S0006-3495(99)77273-5.

[103]   G.E. Gorbet, J.Z. Pearson, A.K. Demeler, H. Cölfen, B. Demeler, Next-Generation AUC: Analysis of Multiwavelength Analytical

Ultracentrifugation Data, Methods Enzymol. 562 (2015) 27–47. doi:10.1016/bs.mie.2015.04.013.

[104]   K.S. Mayya, B. Schoeler, F. Caruso, Preparation and Organization of Nanoscale Polyelectrolyte-Coated Gold Nanoparticles, Adv. Funct. Mater. 13 (2003) 183–188. doi:10.1002/adfm.200390028.

[105]   E.B. Svedberg, J. Ahner, N. Shukla, S.H. Ehrman, K. Schilling, FePt nanoparticle hydrodynamic size and densities from the polyol process as determined by analytical ultracentrifugation, Nanotechnology. 16 (2005) 953–956. doi:10.1088/0957-4484/16/6/056.

[106]   F. Toni, H. Xing, J. Walter, V. Strauß, T.J. Nacken, C. Damm, et al., Production of well dispersible single walled carbon nanotubes via a "floating catalyst-"method, Chemical Engineering Science. 138 (2015) 385–395. doi:10.1016/j.ces.2015.08.002.

[107]   J.A. Jamison, K.M. Krueger, J.T. Mayo, C.T. Yavuz, J.J. Redden, V.L. Colvin, Applying analytical ultracentrifugation to nanocrystal suspensions, Nanotechnology. 20 (2009) 355702. doi:10.1088/0957-4484/20/35/355702.

[108]   B. Sandmann, B. Happ, I. Perevyazko, T. Rudolph, F.H. Schacher, S. Hoeppener, et al., Incorporation of core–shell particles into methacrylate based composites for improvement of the mechanical properties, Polym. Chem. 6 (2015) 5273–5280. doi:10.1039/C4PY01544D.

[109]   I.Y. Perevyazko, J.T. Delaney, A. Vollrath, G.M. Pavlov, S. Schubert, U.S. Schubert, Examination and optimization of the self-assembly of biocompatible, polymeric nanoparticles by high-throughput nanoprecipitation, Soft Matter. 7 (2011) 5030–5035. doi:10.1039/C1SM05079F.

[110]   L. Diaz, C. Peyrot, K.J. Wilkinson, Characterization of Polymeric Nanomaterials Using Analytical Ultracentrifugation, Environ. Sci. Technol. 49 (2015) 7302–7309. doi:10.1021/acs.est.5b00243.

[111]   M. Holzer, V. Vogel, W. Mäntele, D. Schwartz, W. Haase, K. Langer, Physico-

chemical characterisation of PLGA nanoparticles after freeze-drying and storage, European Journal of Pharmaceutics and Biopharmaceutics. 72 (2009) 428–437. doi:10.1016/j.ejpb.2009.02.002.

[112]   A. Bootz, V. Vogel, D. Schubert, J. Kreuter, Comparison of scanning electron microscopy, dynamic light scattering and analytical ultracentrifugation for the sizing of poly(butyl cyanoacrylate) nanoparticles, European Journal of Pharmaceutics and Biopharmaceutics. 57 (2004) 369–375. doi:10.1016/S0939-6411(03)00193-0.

[113]   W. Wang, C. Damm, J. Walter, T.J. Nacken, W. Peukert, Photobleaching and stabilization of carbon nanodots produced by solvothermal synthesis, Phys. Chem. Chem. Phys. 18 (2016) 466–475. doi:10.1039/c5cp04942c.

[114]   A.A. Sousa, J.T. Morgan, P.H. Brown, A. Adams, M.P.S. Jayasekara, G. Zhang, et al., Synthesis, Characterization, and Direct Intracellular Imaging of Ultrasmall and Uniform Glutathione-Coated Gold Nanoparticles, Small. 8 (2012) 2277–2286. doi:10.1002/smll.201200071.

[115]   K. Nontapot, V. Rastogi, J.A. Fagan, V. Reipa, Size and density measurement of core–shell Si nanoparticles by analytical ultracentrifugation, Nanotechnology. 24 (2013) 155701. doi:10.1088/0957-4484/24/15/155701.

[116]   L.A. Fielding, O.O. Mykhaylyk, S.P. Armes, P.W. Fowler, V. Mittal, S. Fitzpatrick, Correcting for a Density Distribution: Particle Size Analysis of Core–Shell Nanocomposite Particles Using Disk Centrifuge Photosedimentometry, Langmuir. 28 (2012) 2536–2544. doi:10.1021/la204841n.

[117]   J.K. Streit, S. Lam, Y. Piao, A.R. Hight Walker, J.A. Fagan, M. Zheng, Separation of double-wall carbon nanotubes by electronic type and diameter, Nanoscale. 9 (2017) 2531–2540. doi:10.1039/c6nr09257h.

[118]   A. Koeth, B. Tiersch, D. Appelhans, M. Gradzielski, H. Coelfen, J. Koetz, Synthesis of Core-Shell Gold Nanoparticles with Maltose-Modified Poly(Ethyleneimine), Journal of Dispersion Science and Technology. 33

(2012) 52–60. doi:10.1080/01932691.2010.530084.

[119]   J.A. Jamison, K.M. Krueger, C.T. Yavuz, J.T. Mayo, D. LeCrone, J.J. Redden, et al., Size-Dependent Sedimentation Properties of Nanocrystals, ACS Nano. 2 (2008) 311–319. doi:10.1021/nn700144m.

[120]   J.B. Falabella, T.J. Cho, D.C. Ripple, V.A. Hackley, M.J. Tarlov, Characterization of Gold Nanoparticles Modified with Single-Stranded DNA Using Analytical Ultracentrifugation and Dynamic Light Scattering, Langmuir. 26 (2010) 12740–12747. doi:10.1021/la100761f.

[121]   D.N. Benoit, H. Zhu, M.H. Lilierose, R.A. Verm, N. Ali, A.N. Morrison, et al., Measuring the Grafting Density of Nanoparticles in Solution by Analytical Ultracentrifugation and Total Organic Carbon Analysis, Anal. Chem. 84 (2012) 121009152814008–9245. doi:10.1021/ac301980a.

[122]   R.P. Carney, J.Y. Kim, H. Qian, R. Jin, H. Mehenni, F. Stellacci, et al., Determination of nanoparticle size distribution together with density or molecular weight by 2D analytical ultracentrifugation, Nat Comms. 2 (2011) 335. doi:10.1038/ncomms1338.

[123]   V. Mittal, M.D. Lechner, Size and density dependent sedimentation analysis of advanced nanoparticle systems, J Colloid Interface Sci. 346 (2010) 378–383. doi:10.1016/j.jcis.2010.03.025.

[124]   M.S. Arnold, J. Suntivich, S.I. Stupp, M.C. Hersam, Hydrodynamic Characterization of Surfactant Encapsulated Carbon Nanotubes Using an Analytical Ultracentrifuge, ACS Nano. 2 (2008) 2291–2300. doi:10.1021/nn800512t.

[125]   J.A. Fagan, M. Zheng, V. Rastogi, J.R. Simpson, C.Y. Khripin, C.A.S. Batista, et al., Analyzing Surfactant Structures on Length and Chirality Resolved (6,5) Single-Wall Carbon Nanotubes by Analytical Ultracentrifugation, ACS Nano. 7 (2013) 3373–3387. doi:10.1021/nn4002165.

[126]   S. Lam, M. Zheng, J.A. Fagan, Characterizing the Effect of Salt and Surfactant Concentration on the Counterion Atmosphere around

Surfactant Stabilized SWCNTs Using Analytical Ultracentrifugation, Langmuir. 32 (2016) 3926–3936. doi:10.1021/acs.langmuir.6b00605.

[127] L.G. AbdulHalim, S. Ashraf, K. Katsiev, A.R. Kirmani, N. Kothalawala, D.H. Anjum, et al., A scalable synthesis of highly stable and water dispersible Ag 44 (SR) 30 nanoclusters, Journal of Materials Chemistry A. 1 (2013) 10148–10154. doi:10.1039/C3TA11785E.

[128] K.M. Harkness, Y. Tang, A. Dass, J. Pan, N. Kothalawala, V.J. Reddy, et al., Ag44(SR)304–: a silver–thiolate superatom complex, Nanoscale. 4 (2012) 4269–4274. doi:10.1039/C2NR30773A.

[129] L.G. AbdulHalim, M.S. Bootharaju, Q. Tang, S. Del Gobbo, R.G. AbdulHalim, M. Eddaoudi, et al., Ag29(BDT)12(TPP)4: A Tetravalent Nanocluster, J. Am. Chem. Soc. 137 (2015) 11970–11975. doi:10.1021/jacs.5b04547.

[130] S. Bestgen, O. Fuhr, B. Breitung, V.S. Kiran Chakravadhanula, G. Guthausen, F. Hennrich, et al., [Ag115S34(SCH2C6H4tBu)47(dpph)6]: synthesis, crystal structure and NMR investigations of a soluble silver chalcogenide nanocluster, Chem. Sci. 8 (2017) 2235–2240. doi:10.1039/c6sc04578b.

[131] J. Walter, G. Gorbet, T. Akdas, D. Segets, B. Demeler, W. Peukert, 2D analysis of polydisperse core-shell nanoparticles using analytical ultracentrifugation, Analyst. 142 (2016) 206–217. doi:10.1039/c6an02236g.

[132] A. Ditsch, S. Lindenmann, P.E. Laibinis, D.I.C. Wang, T.A. Hatton, A. Ditsch, et al., High-Gradient Magnetic Separation of Magnetic Nanoclusters, Ind. Eng. Chem. Res. 44 (2005) 6824–6836. doi:10.1021/ie048841s.

[133] A.H. Latham, R.S. Freitas, P. Schiffer, M.E. Williams, Capillary magnetic field flow fractionation and analysis of magnetic nanoparticles, Anal. Chem. 77 (2005) 5055–5062. doi:10.1021/ac050611f.

[134] C. Röcker, M. Pötzl, F. Zhang, W.J. Parak, G.U. Nienhaus, A quantitative fluorescence study of protein monolayer formation on colloidal

nanoparticles, Nature Nanotech. 4 (2009) 577–580. doi:10.1038/nnano.2009.195.

[135] W. Mächtle, L. Börger, Analytical ultracentrifugation of polymers and nanoparticles, 2006.

[136] M. Assfalg, L. Ragona, K. Pagano, M. D'Onofrio, S. Zanzoni, S. Tomaselli, et al., The study of transient protein–nanoparticle interactions by solution NMR spectroscopy, Biochimica Et Biophysica Acta (BBA) - Proteins and Proteomics. 1864 (2016) 102–114. doi:10.1016/j.bbapap.2015.04.024.

[137] L. Calzolai, F. Franchini, D. Gilliland, F. Rossi, Protein-Nanoparticle Interaction: Identification of the Ubiquitin-Gold Nanoparticle Interaction Site, Nano Lett. 10 (2010) 3101–3105. doi:10.1021/nl101746v.

[138] L. Calzolai, F. Franchini, D. Gilliland, F. Rossi, Protein–Nanoparticle Interaction: Identification of the Ubiquitin–Gold Nanoparticle Interaction Site, Nano Lett. 10 (2010) 3101–3105. doi:10.1021/nl101746v.

[139] K. Srinivasan, S. Parimal, M.M. Lopez, S.A. McCallum, S.M. Cramer, Investigation into the Molecular and Thermodynamic Basis of Protein Interactions in Multimodal Chromatography Using Functionalized Nanoparticles, Langmuir. 30 (2014) 13205–13216. doi:10.1021/la502141q.

[140] V.P. Brahmkhatri, K. Chandra, A. Dubey, H.S. Atreya, An ultrastable conjugate of silver nanoparticles and protein formed through weak interactions, Nanoscale. 7 (2015) 12921–12931. doi:10.1039/C5NR03047A.

[141] A. Wang, K. Vangala, T. Vo, D. Zhang, A three-step model for protein–gold nanoparticle adsorption, The Journal of Physical …. 118 (2014) 8134–8142. doi:10.1021/jp411543y.

[142] G. Brancolini, A. Corazza, M. Vuano, F. Fogolari, M.C. Mimmi, V. Bellotti, et al., Probing the Influence of Citrate-Capped Gold Nanoparticles on an Amyloidogenic Protein, ACS Nano. 9 (2015) 2600–2613. doi:10.1021/nn506161j.

[143] S. Mondal, R. Thirupathi, L.P. Rao, H.S. Atreya, Unraveling the dynamic

nature of protein–graphene oxide interactions, RSC Adv. 6 (2016) 52539–52548. doi:10.1039/C6RA03759C.

[144]   Dynamics of Nanoparticle-Protein Corona Complex Formation: Analytical Results from Population Balance Equations, Journals.Plos.org. 8 (2013) e64690. doi:10.1371/journal.pone.0064690.

Ahmet Bekdemir

Doctoral Assistant
STI IMX MXG032, Station 12, EPFL
CH-1015, Switzerland
Phone: +41 78 9291480
ahmet.bekdemir@epfl.ch

Summary

Extensive laboratory experience on synthesis of fluorescent dyes for applications on Photodynamic Therapy. PhD studies on Gold Nanoparticle synthesis and their interactions with proteins. Excelled on various protein analysis methods, drug delivery systems and published results in highly prestigious scientific journals. Very strong in working both individually and collaboratively. Undertook management of medium to large scale European Commission Projects with a team of scientific and industrial collaborators. A co-author of a biotechnology patent. Proven multidisciplinary researcher with a strong background on Mathematics, Chemistry and Materials Science.

Education

2013 - 2018 Ph.D. Supramolecular Nanomaterials and Interfaces Laboratory, Materials Science and Engineering, École Polytechnique Fédérale de Lausanne (EPFL), Switzerland
Thesis Title: Investigation of Nanoparticle - Protein Interactions with Novel Methods
Supervisor: Prof. Francesco Stellacci
Date: 02/16/2018

2011-2013 M.Sc., Magna Cum Laude. Chemistry, Graduate School of Engineering and Science, Bilkent University, Chemistry Department, Ankara, Turkey.
Thesis Title: Optimization of Orthogonal Reactions on Bodipy Dyes for One-pot Synthesis of Light Harvesting Dendrimers
Supervisor: Prof. Engin Umut Akkaya

2008-2011 B.Sc., Magna Cum Laude. Chemistry, Faculty of Science, Bilkent University, Ankara, Turkey.

2005-2008 B.Sc. Mathematics, Faculty of Science, Bilkent University, Ankara, Turkey. Program Terminated with Transfer to Chemistry Department.

Main Research Projects

- Development of novel methods for thermodynamic characterization of protein adsorption on small gold nanoparticles with Analytical Ultracentrifugation (AUC).

- Investigation of binding mechanism of proteins to sub-10 nm mixed ligand gold nanoparticles with 15N HSQC NMR and AUC.

- Synthesis and Fabrication of Light Responsive Nanoactuators Based on Gold Nanorods

– Developing synthetic methodology for polymeric nanoparticles with monodisperse gold nanorods and their assemblies with controlled crosslinking chemistry. Collaboration with MicroBioRobotic Systems Laboratory, Prof. Selman Sakar, EPFL, Switzerland.

- Amphiphilic Gold Nanoparticle-Based Cytosolic Drug Delivery Platforms for Cancer an Infections.

  – Responsible for synthesis and characterization of optimal mixed ligand gold nanoparticles and antibody conjugations for efficient drug delivery platforms. Collaboration with Prof. Darrell Irvine, MIT, USA.

Employment

Academic Collaborator to industrial partner, Midatech Pharma, UK. Preparation and Characterization of Functional Gold Nanoparticles for Drug Delivery Applications. (May 2015 - ongoing)

Research Assistant under 7th Framework Programme by European Commission, Self-Assembled Virus Like Vectors for Stem Cell Phenotyping (SAVVY), Total Budget of 4 Million . EPFL, Switzerland. (May 2013 - September 2016)

Teaching Assistant Thermodynamics in Materials Science. EPFL, Switzerland. (September 2016 - December 2016)

Guest Research Assistant Bionanoplasmonics Group, Prof. Luis Liz M. Marzan, CIC BiomaGUNE, Spain. (April 2014-May 2014)

Teaching Assistant Surface Science in Materials. EPFL, Switzerland. (February 2014 - April 2014)

Guest Research Assistant Advanced Polymer and Biomaterials Group, Prof. Joerg Lahann, Karlsruhe Institute of Technology (KIT), Germany. (November 2013-December 2013)

Summer Internship Process control of aircraft adhesives, paints and sealants, Chemical Process Lab, Turkish Aerospace Industries (TAI), Ankara, Turkey. (June 2011-August 2011)

Teaching Assistant Statistical Thermodynamics. Bilkent University, Turkey. (September 2010 - May 2011)

Undergraduate Research Assistant Mesoporous Silica Nanoparticles as Chemiluminescence Triggered Photosensitizer Carriers, Supervisor: Prof. Dr. Engin U. Akkaya, Bilkent University Chemistry Department, Supramolecular Laboratory, Ankara, TURKEY. (January 2010 - June 2011)

Laboratory Teaching Assistant Organic Chemistry Laboratory Practice. Bilkent University, Turkey. (September 2009 - December 2009)

Honors and Awards

Nominated for Prof. Rene Wasserman Award, EPFL, Lausanne, Switzerland, 2018.

Nominated for MRS Graduate Student Award, Material Research Society (MRS), Boston, USA, 2017.

Finalist on EDMX Graduate Student Award, Material Science Doctoral School, École Polytechnique Fédérale de Lausanne (EPFL), Switzerland, 2017.

Finalist on EPFL Dimitris N. Chorafas Foundation Award, École Polytechnique Fédérale de Lausanne (EPFL), Switzerland, 2017.

Awarded National Scholarship Programme for MSc. Students TUBITAK (Scientific and Technical Research Council of Turkey), 2011-2013.

Dean's High Honour List 2009-2010 Fall, 2009-2010 Spring, 2010-2011 Fall, 2010- 2011 Spring

Dean's Honour List 2008-2009 Fall

Awarded National Scholarship Programme for Undergradute Students TUBITAK (Scientific and Technical Research Council of Turkey)

Awarded Full Scholarship for Outstanding Undergraduate Students Chemistry Department, Bilkent University, (2005-2010)

Top 1000 Ranking in National University Entrance Exam (SS) among 1.5 million attendants.

Top 2% Ranking in National High School Entrance Exam (LGS) among 600 thousand students.

Scientific Publications

Atukorale P.U., Guven Z.P.*, Bekdemir A.*, Carney R.P.*, Van Lehn R.C., Soo Yun D., Jacob Silva P., Demurtas D., Yang Y.S., Alexander-Katz A., Stellacci, F., Irvine D.J., **Bioconjugate Chemistry**, 2018, Accepted. * These authors contributed equally to this work.

Cagno, V., Andreozzi, P., D'Alicarnasso, M., Silva, P.J., Mueller, M., Jones, S.T., Vallino, M., Hodek, J., Weber, J., Sen, S., Vukovic, L., Janecek, E.R., Bekdemir, A., Sanavio, B., Martinelli, C., Donalisio, M., Kaiser, L., Tapparel, C., Král, P., Krol, S., Lembo, D., Stellacci, F., **Nature Materials**, 2018, 17, 195-203.

Yang, Y-S., Atukorale, P.U., Moynihan, K., Bekdemir, A., Rakhra, K., Tang, L., Stellacci, F., Irvine, D.J., **Nature Communications**, 2017, 8, 14069.

Bekdemir, A., Stellacci, F. **Nature Communications**, 2016, 7, 13121.

Serrano-Montes, A. B., Langer, J., Henriksen-Lacey, M., De Aberasturi, D. J., Sols, D. M., Taboada, J. M., Obelleiro, F., Sentosun, K., Bals, S., Bekdemir, A., Stellacci, F., Liz-Marzán, L. M. **The Journal of Physical Chemistry C**, 2016, 120(37), pp 20860-20868.

Zhao, H., Ghirlando, R., Alfonso, C., Arisaka, F., Attali, I., Bain, D. L., Bakhtina, M. M., Becker, D. F., Bedwell, G. J., Bekdemir, A., ..., Schuck, P. **PloS One**, 2015, 10(5).

Atukorale, P. U., Yang, Y.-S., Bekdemir, A., Carney, R. P., Silva, P. J., Watson, N., Stellacci, F., Irvine, D. J. **Nanoscale**, 2015, 7(26), pp 11420-11432.

Ertem, E.*, Bekdemir, A.*, Atilgan, A, Akkaya E.U. **Pure and Applied Chemistry**, 2014, 86(9), pp 899-903. * These authors contributed equally to this work.

Conferences

Bekdemir, A., Stellacci, F. Investigation of Protein - Nanoparticle Interactions with Novel Methods, **Talk** MRS Fall 2017, Boston, USA.

Bekdemir, A., Stellacci, F. Analytical Ultracentrifugation as a tool for Nanoparticle - Protein interactions, **Poster Presentation** AUC 2015, Melbourne, Australia.

Bekdemir, A., Stellacci, F. Analytical Ultracentrifugation as a tool for Nanoparticle - Protein interactions, **Invited Talk** AUC 2015, Melbourne, Australia.

Bekdemir, A., Stellacci, F. Protein Binding Behaviors of Mixed-Ligand Gold Nanoparticles, **Poster Presentation** EDMX Research day, 2015, Lausanne, Switzerland.

Patents

Irvine, D.J., Yang, Y.S., Bekdemir A., Stellacci, F., Nanoparticles Comprising A Metal Core Surrounded By A Monolayer For Lymph Node Targeting, WO 2017/070676.

Languages

Turkish (Mother Tongue), English (Advanced), German (Beginner)